UC San Diego
UC San Diego Electronic Theses and Dissertations

Title
Non-diffusive cross field transport in scrape-off-layer in Tokamak

Permalink
https://escholarship.org/uc/item/9rp7b8vv

Author
Yu, Guanghui

Publication Date
2006

Peer reviewed|Thesis/dissertation

UNIVERSITY OF CALIFORNIA, SAN DIEGO

Non-diffusive Cross Field Transport in

Scrape-off-Layer in Tokamak

A dissertation submitted in partial satisfaction of the

requirements for the degree Doctor of Philosophy

in

Engineering Sciences (Mechanical Engineering)

by

Guanghui Yu

Committee in charge:

        Professor Sergei I. Krasheninnikov, Chair
        Professor Farhat Beg
        Professor Farrokh Najmabadi
        Professor Thomas M. O'Neil
        Professor Sutanu Sarkar

2006

The dissertation of Guanghui Yu is approved, and it is acceptable in quality and form for publication on microfilm:

_____

_____

_____

_____

_____ Chair

University of California, San Diego

2006

To my parents Meiying and Qimimg, who make this achievable.

To my wife Rubing, who makes this enjoyable.

To Evelyn, who is my angel.

TABLE OF CONTENTS

LIST OF FIGURES

LIST OF TABLES

ACKNOWLEDGMENTS

My graduate study for five years has involved assistance and support of many people. I appreciate to all of them and wish to use the limited space to thank a few in particular.

I would firstly thank my advisor, Prof. Sergei I. Krasheninnikov for giving me the great opportunity to achieve my PhD research. It is him who brings me into the world of plasma physics and arouses my interest in theory by his extraordinary enthusiasm and insightful perspective in research. I would also like to thank the other members of my committee (Prof. Farhat Beg, Prof. Farrokh Najmabadi, Prof. Sutanu Sarkar, and Prof. Thomas M. O'Neil) for taking the time to review my work.

I wish to thank all members in our group. I am honored to work with Dr. Sergei A. Galkin, who gives me unparalleled assistance in the beginning to understand our simulation model. It is my pleasure to be an officemate, and of course a friend, of Boris Frolov with plenty of constructive and interesting talk and fun. I am grateful for fruitful collaborations with Dr. Dan D'Ippolito and Dr. James R. Myra in Lodestar Research Corporation. The rotational blob, in which we work together, is definitely a highlight part in this work. I would also express my gratitude to departmental graduate coordinator, Beverley Walton, and the previous network manager in PISCES group, Maggie Qu, for many helps in smoothening the way.

I have been fortunate to have many good friends along the journey. I want to thank all of them for their aid in both study and life, and for their friendship to make the journey a pleasant and memorable one. In particular, grateful thanks are due to Laizhong Cai, for sharing his insightful opinions in study and research with me, and Haoxiang Luo, for his valuable suggestions in modelling work and Linux system.

Finally I owe my deepest gratitude to my family. Thanks to my wife for her love and support. Thanks to my parents for their encouragement along the way. Thanks also to my parents-in-law for taking care of their grand-daughter during my preparation for the dissertation.

In this dissertation the text of Chapter 5 is, in part, a reprint of the material as it appears in "Two dimensional modelling of blob dynamics in tokamak edge plasmas," G. Q. Yu, S. I. Krasheninnikov, and P. N. Guzdar published in Physics of Plasmas 13, 042508-1 (2006). The text of Chapter 6 is, in full, a reprint of the material as it appears in "Two dimensional modelling of blob dynamics in tokamak edge plasmas," G. Q. Yu, S. I. Krasheninnikov, and P. N. Guzdar published in Physics of Plasmas 13, 042508-1 (2006). The text of Chapter 7 contains material of the paper "Dynamics of blobs in scrape-off-layer/shadow regions of tokamaks and linear devices," G. Q. Yu and S. I. Krasheninnikov, published in Physics of Plasmas 10, 4413 (2003). The text of Chapter 8 contains material of the paper "Rotational stability of plasma blobs," D. A. D'Ippolito, J. R. Myra, D. A. Russell, and G. Q. Yu, published in Physics of Plasmas 11, 4603 (2004) and material of the paper "Convective transport in the scrape-off-layer by nonthermalized spinning blobs," J. R. Myra, D. A. D'Ippolito, S. I.

Krasheninnikov and G. Q. Yu, published in Physics of. Plasmas 11, 4267 (2004). The dissertation author was the primary author or co-author in each of these publications and the co-authors listed in these papers.

VITA

1998	B. S., Department of Thermal Engineering Tsinghua University, Beijing, China
2001	M. S., Department of Thermal Engineering Tsinghua University, Beijing, China
2001-2006	Research Assistant Department of Mechanical and Aerospace Engineering University of California, San Diego
2004-2006	Teaching Assistant Department of Mechanical and Aerospace Engineering University of California, San Diego
2006	Ph.D, University of California, San Diego

HONORS AND AWARDS

2005	Dissertation Fellowship. Department of Mechanical and Aerospace Engineering, University of California, San Diego
2001-2002	Irwin and Joan Jacobs Fellowship. Jacobs School of Engineering. University of California, San Diego

PUBLICATIONS

G. Q. Yu, S. I. Krasheninnikov, and P. N. Guzdar, "Two dimensional modelling of blob dynamics in tokamak edge plasmas," Phys. Plasma 13, 1-1(2006).

S. I. Krasheninnikov, D.D. Ryutov, and G. Q. Yu, "Large plasma pressure perturbations and radial convective transport in a tokamak," J. Plasma Fusion Res. SERIES 6, 139 (2005)

S. I. Krasheninnikov, A. I. Smolyakov, G. Yu, T. K. Soboleva, "Transport of meso-scale structures in tokamak edge plasmas," Czech. J. Phys. 55, 307 (2005)

D. A. D'Ippolito, J. R. Myra, D. A. Russell, and G. Q. Yu "Rotational stability of plasma blobs," Phys. Plasma 11, 4603 (2004)

J. R. Myra, D. A. D'Ippolito, S. I. Krasheninnikov and G. Q. Yu, "Convective transport in the scrape-off-layer by nonthermalized spinning blobs," Phys. Plasmas 11, 4267 (2004)

D. A. D'Ippolito, J. R. Myra, S. I. Krasheninnikov, G. Q. Yu, and A. Yu. Pigarov, "Blob transport in the tokamak scrape-off-layer," Contrib. Plasma Phys. 44, 205 (2004)

G. Q. Yu and S. I. Krasheninnikov, "Dynamics of blobs in scrape-off-layer/shadow regions of tokamaks and linear devices," Phys. Plasmas 10, 4413 (2003)

S. I. Krasheninnikov, A. Yu. Pigarov, S. A. Galkin, G. Q. Yu et al., "Blobby cross-field plasma transport in tokamak edge," 19th IAEA Fusion Energy Conference, Lyon, France, Oct 2002, Paper IAEA-CN-94/TH4-1.

FIELDS OF STUDY

Major Field: Mechanical Engineering

Studies in Fluid Mechanics.
Professors Paul Lindon and Stefan Llewellyn-Smith

Studies in Applied Mathimatics
Professors Glenn Ierley, William Young, Carl FitzGerald, and Jeffrey Rabin

Studies in Plasma Physics.
Professors Sergei Kransheninnikov and George Tynan

Studies in Computational Science.
Professors Tom Bewley and Constantine Pozrikidis

Studies in Electromagnetism.
Professor David MacFarlane

ABSTRACT OF THE DISSERTATION

Non-diffusive Cross Field Transport in

Scrape-off-Layer in Tokamak

by

Guanghui Yu

Doctor of Philosophy in Engineering Sciences (Mechanical Engineering)

University of California, San Diego, 2006

Professor Sergei I. Krasheninnikov, Chair

In recent years, coherent structures in edge plasmas are believed to be one of the major factors in cross-field transport. The present dissertation is dedicated to using theoretical and numerical methods to study the dynamics of individual coherent structure, or so-called blob, moving from bulk plasma to the chamber wall.

Blob is a filament structure extended along magnetic filed lines. We focus on two different types of blob. One is ending up at target plates, the other is not, i.e. the SOL and HB blobs. Two dimensional blob models are derived. Characteristic spatial scale δ_*, time scale t_*, and velocity v_* for blob are obtained and calculated for different tokamaks. They are in agreement with experimental measurements. Scaling

analysis shows blob dynamics sensitive to spatial scale length. Stability analysis shows that blobs with spatial scales less than δ_* may move as coherent structures to large distances.

In the SOL model simulation we have found the most structurally stable blob has scale length around δ_*. Blobs smaller than δ_* evolve into mushroom-like structures. Blobs larger than δ_* are subject to the fingering instability. Blobs with spatial scales close to δ_* can coherently move to long distances. Simulation results show that high density background effectively narrows down blob size and the inertia term in vorticity equation drives blob to mushroom shape and builds up vortex dipole within the structure. We also compare results with and without the Boussinesq approximation.

In the HB model simulation it is shown that blobs have wider stable range. Their steep nose and long relaxation tail can explain experimentally detected asymmetric profile. HB blob moves with a constant velocity.

In the biasing potential model a critical magnitude of the potential barrier is derived. A strong deformation of the blob as coherent structure will be observed while blob pass through a barrier higher than the critical value. Simulation results confirm the theoretical prediction.

In the rotational blob model simulation results show the suppression of radial velocity and the generation of poloidal velocity. Fingering and mushroom effects are inhibited, but blobs evolve into rotational instability at later stage.

Chapter 1

Introduction

1.1 Overview

Coming into 21st century, along with the population booming on the earth and the oil price soaring in 2006, we more and more clearly realize that exploring large dependable source of energy is one of the most important missions our human beings are facing up to. Among several types of feasible "new" energy in the future, such as nuclear energy, solar energy, wind energy, and tide energy etc., thermonuclear fusion energy is the most promising clean energy people can use in the future.

Possibly to be the first industrialized fusion technique, magnetic confinement fusion has been studied for many decades. However, many key problems of magnetic confinement fusion are still under research, and will surely carry on in the International Thermonuclear Experimental Reactor (ITER) project [1]. The edge plasma physics and cross-field transport are certainly in them because they determine the efficiency of magnetic confinement, plasma-wall interaction, and lifetime of chapber wall. Therefore, in some sense, it determines the feasibility of controlled fusion, or at least, makes a big impact on the cost of fusion reactor.

In recent years, coherent structures in edge plasmas are believed to be one of the major factors in cross-field transport. This dissertation work is dedicated to using theoretical and numerical methods to study the dynamics of individual coherent structure in SOL region in tokamak, expecting to understand these mesoscale (to be defined subsequently) structures' evolution on their way from bulk plasma to the chamber wall and provide some clues to control or reduce this transport process when it's undesirable. Understanding how blobs are born and what happens when they are reaching solid wall are beyond the scope of our research.

1.2 Cross-field Transport and Coherent Mesoscale Structure

The achievement of sufficiently long particle and energy confinement is perhaps the most difficult task on the route to a fusion reactor. Energy must be confined long enough for the plasma to reach the temperature, of order 10keV, for thermal reactions, while the ions must be confined long enough for a significant fraction to fuse. So the understanding of the transport phenomena is one of the central issue for realizing burning plasmas. We could say that an appropriate reduction in the undesirable transport means a dramatic decrease in the size and cost of a tokamak fusion reactor.

The particle and energy transport in toroidal plasmas is of two types. The first result from collisions is referred to as classical or neoclassical transport [2, 3, 4, 5]. It exact evaluation is mathematically quite difficult partially because of the complicated orbits of charged particles in a torus. However, much elegant analysis has been done

on this problem, see Ref. [5, 6, 7, 8] and references therein, and neoclassical loss can now be calculated accurately.

The second type of transport, know as anomalous transport [2, 9, 10, 11], results from the fluctuation of electric and magnetic fields, which are generally observed in magnetically confined plasma devices. Experimental results show that plasma loss rate is generally larger than neoclassical transport, which means that anomalous transport is much faster than the neoclassical transport. Therefore, understanding anomalous transport becomes crucial in controlling and reducing cross-field particle and energy losses.

Coherent mesoscale structures, often referred as blobs, have attracted much attention in the research of anomalous transport of edge plasma in recent years. The "mesoscale" means spatially much larger than gyro-radius, but on the other hand it's much smaller than the length scale of fusion devices. It is generally believed that mesoscale dynamics is driven by plasma instabilities due to density and temperature gradients. It becomes more and more clear that intermittent convective-like transport associated with such mesoscale structures is often dominant in the cross-field transport in the SOL of tokamaks, stellarators, and linear devices [12-28]. The term "intermittency" was originally coined to characterize signals measured in turbulent fluids, but has now come to refer more generally to systems undergoing apparently random, rapid switching from quiescent to bursting behaviors, as measured by the magnitude of some suitable system variable [29]. The intermittency features higher pressure and density than the surrounding plasma in edge plasma. Recent experimental

observations suggest that the dynamics of the Edge Localized Modes (ELMs) in high confinement regime in tokamaks are very similar to that of blobs [30,31,32,33,34], and result in a much larger plasma particle and energy fluxes into far SOL than it was thought of. Significant amount of theoretical and computational work on blob physics [35-44] have been done to date. It turns out that reduced two dimensional (2D) blob models are rather simple but still useful approach to understand main features of blob dynamics.

1.3 Experimental Observation of Coherent Structure in Edge Plasma

Recently the physics picture of plasma transport in the scrape-off layers of tokamaks and stellarators has changed because the former theory based on slow diffusive cross-field transport is not compatible with some of the experimental findings. Cross-field particle fluxes have an intermittent character. Large transport events can be responsible for large portion of the total flux.

Progress in those studies has been the result of improvements in several areas. One is the continuous improvement of edge plasma diagnostics. New diagnostics have allowed people to go from single point measurements to a visualization of structures at the plasma edge. The 2D radial vs. poloidal structures and motions of edge trubulence in the experimental magnetic confinement facilities have been trying to detect in wide time period. Because of the rather small scale length (normally several cms), high speed (around 10^5 cm/s), and harsh environment in edge plasma, measuring and

tracking mesoscale structures in SOL are technically very difficult. So far, measurements of edge-turbulence-developed structures have been made using Langmuir probes [45, 46, 47], beam emission spectroscopy (BES) [48], and gas puff imaging (GPI) [49,50]. We will introduce the recent diagnostic results as the following.

1.3.1 Langmuir Probes

It is well-known that fluctuations in the SOL are large and the fluctuation-induced particle flux is the dominant component in the total cross-field flux [51, 52, 53, 54, 55]. The most common fluctuation diagnostics techniques used in the SOL are based on electrostatic Langmuir probes, which are used in measuring ion saturation current (I_{sat}) fluctuations, floating potential fluctuations (from which one may derive the plasma potential [56]), electron temperature, etc. A local particle flux may be calculated from these measurements.

Figure 1.1 shows the results of the I_{sat} , E_θ and $I_{sat}E_\theta$ signals for three spatial locations in the SOL, namely, (a) close to separatrix, (b) 5 cm into the SOL, and (c) 10 cm into the SOL, which are measured by Langmuir probes. It is noticed that (1) the I_{sat} pulses are always positive, (2) the E_θ pulses are always positive and (3) the amplitudes of the I_{sat} and E_θ events are quickly reduced (by a factor of ~7) away from the separatrix. Intermittency, i.e., occasional bursts in a signal, is quite evident in many edge diagnostics in tokamaks. The intermittent character of the fluctuations is a very important result from the analysis of these measurements. More details of the study can be found in [19].
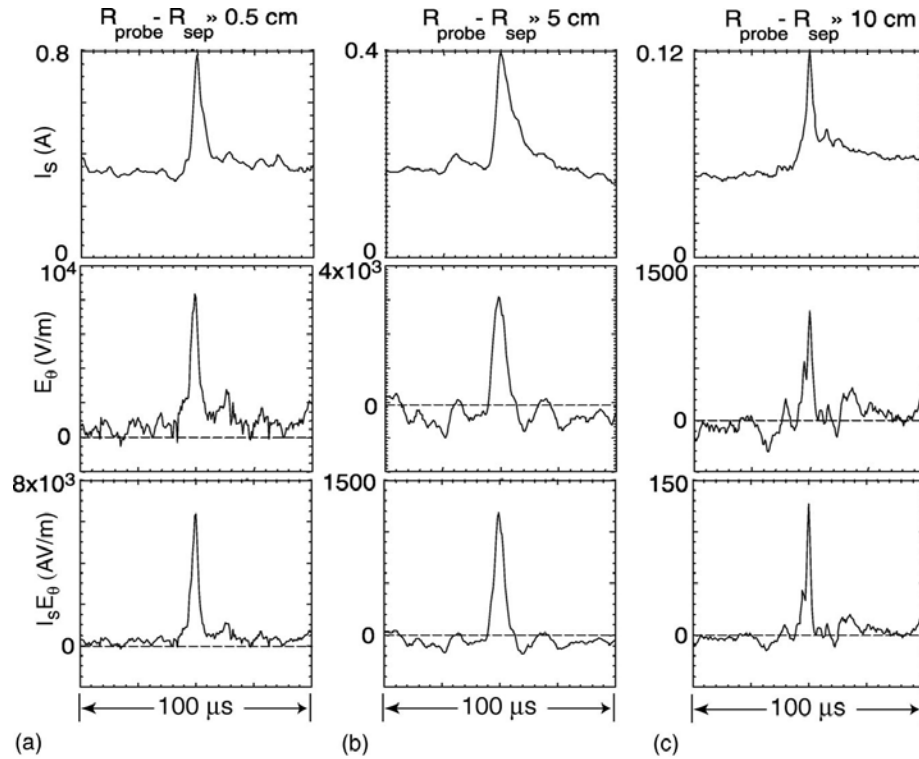
Figure 1.1 Results of the I_{sat} (top), E_θ (middle) and $I_{sat}E_\theta$ signals for radial locations within (a) 0.5 cm, (b) 5 cm and (c) 10 cm of the LCFS, showing the intermittent feature and its amplitude decaying with radius. [19].

1.3.2 Beam Emission Spectroscopy

The BES measures plasma density fluctuations at relatively high spatial resolution. It observes density fluctuations by measuring the emission from neutral beam deuterium atoms that undergo collisions with the plasma ions and electrons. The observed beam-plasma emission intensity fluctuations are related to density fluctuations through the atomic physics of particle collisions, excitation, ionization and emission. The intensity of the signal begins to saturate at higher plasma densities. for more details, see [57, 58, 59].

Bursting density and its velocity can be visualized by comparing two frames (2-D images) from BES [60], separated in time by 6 μs as shown in Figure 1.2, where the last closed flux surface (LCFS) is indicated by a solid vertical line. High density is indicated in red and low in blue. The radial motion of a positive density structure, marked by a dashed circle in both frames, is indicated by vertical dashed lines. Notice that the object has a radial and poloidal spatial extent of roughly 2 cm. From the two frames it is clear that the object is moving poloidally and radially with speeds that can be easily estimated at $v_\theta = 5 \times 10^5$ cm/s and $v_r = 1.5 \times 10^5$ cm/s. These compare well to Langmuir probe results.
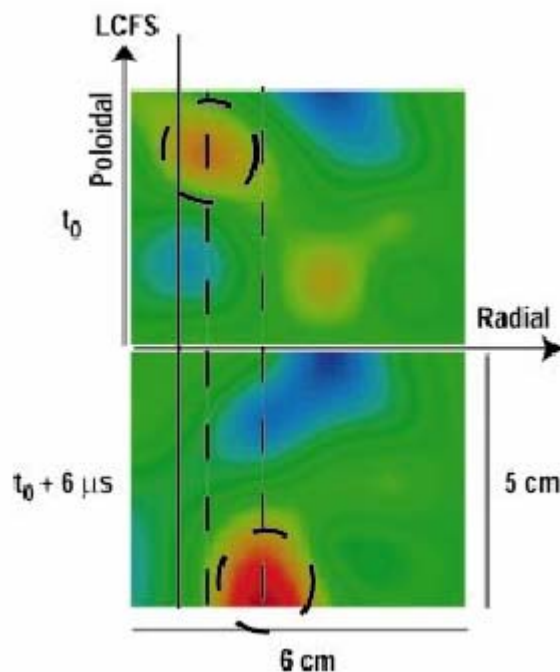
Figure 1.2 (Color) Two frames from BES showing 2D density plots. There is a time difference of 6 μs between frames. Red indicates high density and blue low density. A structure, marked with a dashed circle and shown in both frames, features poloidal and radial motion [60].

1.3.3 Gas Puff Imaging

The GPI diagnostic can be used to study the turbulence present at the edge of magnetically confined plasmas. In GPI diagnostic the instantaneous 2D radial vs. poloidal structure of the turbulence is detected by fast-gated cameras and discrete fast chords [20, 22].

(a)

(b)
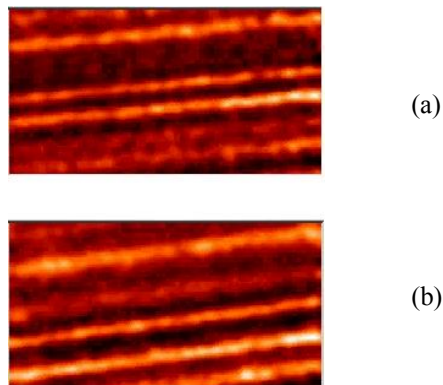
Figure 1.3 (Color) Side viewing images taken from movie of edge turbulence in C-Mod. The "filaments" of bright light emission in D-alpha are aligned nearly along the local magnetic field direction. This result and more pictures and movies can be found at http://www.pppl.gov/~szweben/.

Figure 1.3 presents the GPI results in the Alcator C-Mod tokamak. (a) and (b) are two snap shots taken from side view movie of edge turbulence in C-Mod around mid-plane region in the SOL. The "filaments" of bright light emission in D-alpha are aligned nearly along the local magnetic field direction. Figure 1.4 shows the GPI results in the National Spherical Torus Experiment (NSTX). (a) and (b) are two frames cut from edge turbulence movies in NSTX. This view of the plasma is located just above the outer mid-plane near the magnetic separatrix (dashed line). The vertical

direction is approximately poloidal, and the horizontal direction is approximately radial (with out toward the right). The solid vertical line is the RF limiter. Blob-like structures are clearly captured with both radial and poloidal velocity. The speed is about 10^5 cm/s. These results and more details about the measurements and plenty of interesting pictures and movies can be found at http://www.pppl.gov/~szweben/.

1.3.4 Edge Localized Modes

Edge localized modes (ELMs) are often seen in H-mode plasmas. It is a temporary relaxation of the very high edge gradients observed in H-modes and it may be a relaxation back to the L-mode.

(a)

(b)
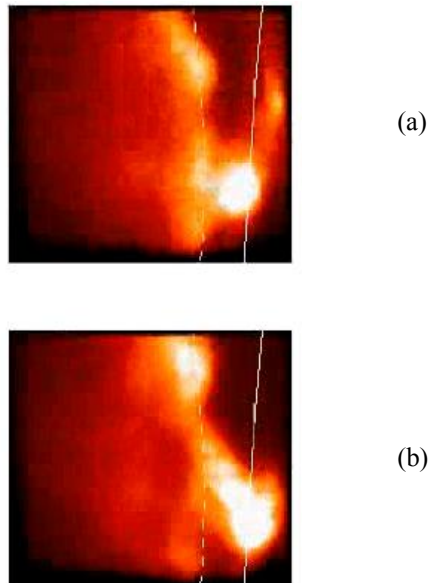
Figure 1.4 (Color) Two frames cut from edge turbulence movies in NSTX. This view of the plasma is located just above the outer midplane near the magnetic separatrix (dashed line). The vertical direction is approximately poloidal, and the horizontal direction is approximately radial (with out toward the right). The solid vertical line is the RF limiter. This result and more pictures and movies can be found at http://www.pppl.gov/~szweben/.

ELMs were first observed as short bursts detected by Mirnov coils and soft x-ray diodes, associated with periodic density and temperature reduction in the outer plasma zones of H-mode plasmas [61]. Large Type-I ELMs [62] are observed in good confinement regime, which can be destroyed by the ELMs themselves, triggering the return to the L-mode regime. The ELMs represent one of the main outstanding crucial issues for the design of large scale magnetic fusion reactor like ITER [63, 64], as the outflux of plasma energy and particles caused by these events could disturb steady-state operation [65] and cause serious damage of the first wall [66]. Hence a lot of effort has been devoted towards characterizing the ELMs as function of various plasma parameters across different machines.

Many recent experimental observations [29-33, 67] suggest that the dynamics of ELMs in the SOL plasma are very much similar to those of blobs. The temporal ELMs substructures being detected are related to spatial substructures on the scale of 1-2 cm [67], which is indeed in the most stable scale length range of blobs.

1.4 Two Dimensional Blob Model

So far, the name "blob" has been mentioned a couple of times and will be discussed even much more in the following Chapters. It is necessary to make it clear at this stage that what blob is and how 2D blob is related to three dimensional filament structures.

As we discuss in previous sections, in the last years the overall picture of fluctuations and transport in the SOL has changed because of much more quantitative

measurements obtained by latest techniques [68]. Its essential part is altering from a diffusive cross-field transport model to an intermittent transport model dominated by large transport events. Different authors [26, 35, 45, 69] have given different names to these transport events, which were first detected in the Caltech tokamak and were called "blobs" in Ref. [45].

A three dimensional (3D) density fluctuation in the SOL is a long filament along the toroidal direction. In 2D domain perpendicular to field lines it's a coherent "blob" or bubble. The spatial relative positions of magnetic field, target plates, and blob with the coordinates in the slab frame are shown in Figure 1.5. Note that all 2D simulation results in the thesis are shown in the frame of Figure 1.5 (b).

(a)   (b)
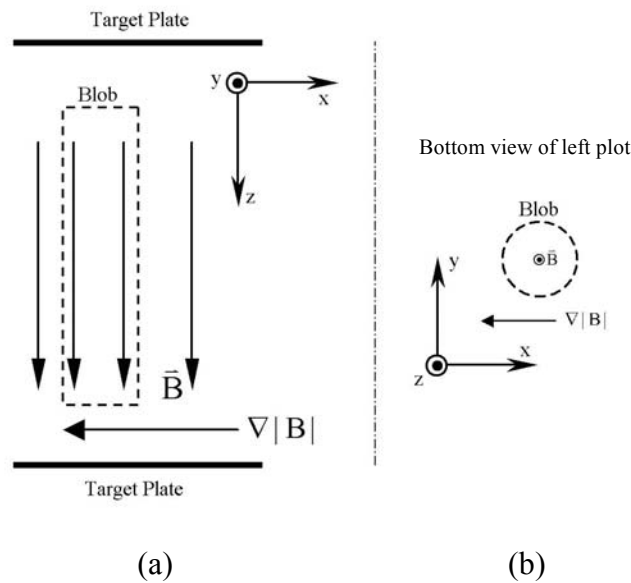
Figure 1.5 Sketch of blob in space. (a) is spatial relative positions of magnetic field, target plates, and blob. (b) is a bottom view of (a). Note that all 2D simulation results in the thesis are shown in the bottom view frame.

1.5 Dissertation Outline

The present dissertation consists in theoretical and numerical attempts to gain understanding of some experimental observed phenomena of intermittent coherent structure, blob, which is very active in tokamak edge plasma.

In present Chapter, we provide the goal of this dissertation work, introduce basic concepts and recent experimental results as very important bases of our research, and give a brief outline of its content.

Chapter 2 is dedicated to the review of the fundamental plasma theories behind our modelling work.

In Chapter 3, we review the derivation of our simple 2D blob model in SOL and normalization approach to make governing equations to be of unity-coefficient. We also use linear theory to study local stability of blob. Very important characteristic parameters in length and time are derived. Our numerical simulation is based on the normalized equations.

Chapter 4 describes the basis of our numerical model. The slab frame, spatial discretization, and time advance method are discussed. Models with/without Boussinesq approximation, relaxation technique, and effect of spatial resolution and data accuracy for our simulation are included in this Chapter.

The numerical results are covered in Chapter 5 through Chapter 8. Chapter 5 is devoted to the dynamics of individual blob along the open field lines, i.e. the SOL blob. Effects of spatial scale length, density background, and different terms in governing equation are discussed in this Chapter. Further more, a numerical model

without the Boussinesq approximation, i.e. the FI-SOL approach, and dip motions are also demonstrated in Chapter 5. Chapter 6 presents simulation results of blob in high β regime. We also talk about the impact of plasma diffusion in this Chapter. Chapter 7 contains how SOL blobs passing through the biasing potential region. A theoretical criteria of deformation of configuration is derived. In Chapter 8, we consider the non-thermalized blob dynamics with plasma rotation. Simple model for spinning blobs driven by the monopole temperature potential inside are given. The change of velocity due to rotation and rotational instability are discussed.

In Chapter 9 we summarize all results in this dissertation.

1.6 Units and Notations

In this work we use Gaussian units in equations and derivations unless explicitly noted to the contrary. After normalization of equations, all variables are non-dimensional. Real unit values can be converted by the characteristic normalizing constants addressed in Chapter 3. Vector variables are written in **bold** format. The symbol e refers to the absolute value of electron charge. In our simple 2D slab domain, we make use of the cartesian coordinates (x, y) to replace the directions (r, θ) in primitive toroidal coordinate systems.

Chapter 2

Fundamental Theories in Edge Plasma

In this Chapter, we are going to review some fundamental theories applied in edge plasma, which are related to our research work. They mainly are general reviews of fluid equations, MHD equations, Rayleigh-Taylor (RT) instability, Kelvin-Helmholtz (KH) instability, resistivity, sheath, and polarization in blob and the E×B drift with polarization induced electric field.

2.1 Fluid Equations

2.1.1 Continuity Equation

In fluid equations, we are looking at plasma as an ensemble of charged particles, whose behavior is a special kind of fluid. If only consider a single species of particle at one time, it is typical to derive the continuity equation as follows,

$$\frac{\partial n_\alpha}{\partial t} + \nabla \cdot (n_\alpha \mathbf{v}_\alpha) = S_\alpha \tag{2.1}$$

where n_α is the particle density for any single species α, $\mathbf{v}_\alpha$ is the average velocity, and S_α is a volume source rate of α particles. For the charged particles of a plasma, a

volume source term would arise from the ionisation of neutral atoms; recombination would give rise to a corresponding volume sink term. For the present work, we will generally neglect ionisation and recombination, but it should be aware that sources and sinks of particles do arise in plasmas and give additional terms in all of the fluid equations.

2.1.2 Momentum Balance Equation

We consider next the two-fluid momentum balance equations for species α and β. Considering the famous Navier-Stokes (NS) equation, taking the electric force and Lorentz force into account, and neglecting the gravitational force, the momentum equation for species α reads

$$m_\alpha n_\alpha (\frac{\partial \mathbf{v}_\alpha}{\partial t} + (\mathbf{v}_\alpha \cdot \nabla)\mathbf{v}_\alpha) = n_\alpha q_\alpha (\mathbf{E} + \frac{1}{c}\mathbf{v}_\alpha \times \mathbf{B}) - \nabla P_\alpha + \mathbf{R}_{\alpha\beta} \tag{2.2}$$

Where $\mathbf{E}$ is electric field, $\mathbf{B}$ is magnetic field, P_α is the pressure, q is the charge per particle, m_α is the mass of particle α, and c is the speed of light. $\mathbf{R}_{\alpha\beta}$ denotes the momentum volume rate gained by species α due to collisions with species β.

2.2 Hydrodynamic Instabilities

Hydrodynamic instabilities in fusion plasmas are very common. There are so many types of instabilities associated with fusion plasmas that it is very hard to fully list out. Of course, there are many instabilities associated with blob study such as the RT instability [70-77], the KH instability [78, 79], the Richtmyer-Meshkov (RM)

instability [80, 81], and the rotational instability [78] etc. These instabilities are key to the understanding of many essential phenomena in blob dynamics. We introduce two most famous typical instabilities, the RT and KH instability, as follows. We are trying to review the phenomenology of both instabilities basically at the beginning stage.

2.2.1 Rayleigh-Taylor Instability

The RT instability is a density gradient + effective gravitational force driven instability. If the density gradient and the effective gravitational force are in same direction, the system is stable; if in opposite direction, the system is unstable.
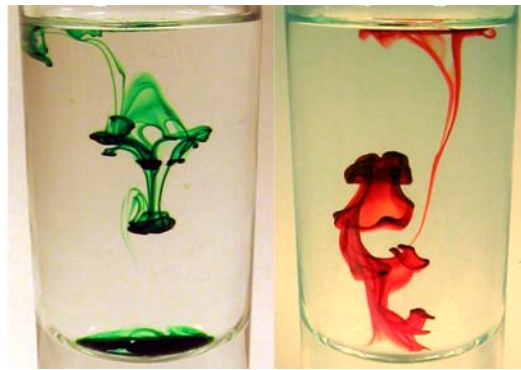
(a)
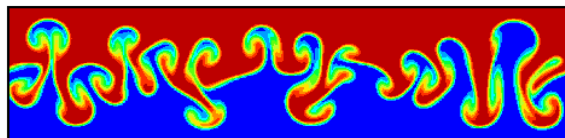
(b)

Figure 2.1 (Color) Rayleigh-Taylor instability. (a) RT instability in real fluid: falling green dye in vinegar and rising red dye in sugar syrup [82]; (b) Simulation result of RT instability [83].

There is a complex phenomenology associated with the evolution of the RT instability. This includes the formation of fingers and bubbles, the development of KH instability on the side of the fingers, and much more [72].

Figure 2.1 shows RT instability in both real fluid and numerical simulation. We see the featured fingering effect and KH-related mushroom phenomenon in both cases.

2.2.2 Kelvin-Helmholtz Instability

KH instability can occur when velocity shear is present within a continuous fluid or when there is sufficient velocity difference across the interface between two fluids. The theory can be used to predict the onset of instability and transition to turbulent flow in fluids of different densities moving at various speeds. When two parallel streams of different velocities are adjacent to each other, the flow can be unstable to perturbations, even infinitesimal ones, for all speeds.

(a)

(b)
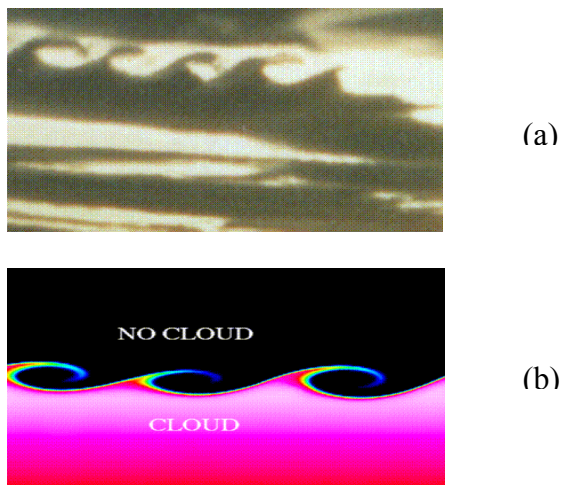
Figure 2.2 (Color) Kelvin-Helmholtz instability. (a) KH instability in real fluid: cloud in the sky; (b) Simulation result of KH instability. [84]

Observed plenty of times in real fluid, also predicted by theory, KH instability occurred on velocity difference interface is associated with the famous Kelvin's cat's eye pattern in streamline. Figure 2.2 shows KH instability in both real fluid and numerical simulation. We see the cat's eye pattern in both cases. It's interesting to note that the mushroom patter in RT instability actually consists of two symmetric cat's eyes.

2.3 Sheath

2.3.1 The Collisionless Sheath

In all magnetically confined plasma devices, the plasma is contained in a vacuum chamber of finite size. At the edge of the bounded plasma an electrostatic potential drop exists to contain the more mobile charged species. This allows the flow of positive and negative carriers to the wall to be balanced. The plasma will therefore charge positively with respect to a grounded wall (see Figure 2.3). The potential layer, which must exist on all cold walls with which the plasma is in contact, is called a sheath.

For simplicity, we just pay our attention on a one-dimensional model with no magnetic field as in Figure 2.3. Suppose there is no appreciable electric field inside the plasma, so the potential φ_p is a constant. Since electrons have much higher thermal velocities than ions, they are lost faster and leave the plasma with a net positive charge. The plasma must then have a potential positive with respect to the wall, i.e., the wall

potential φ_w is lower than φ_p. This potential cannot be distributed over the entire

plasma, since the Debye shielding [85] will confine the potential variation to a layer of

the order of several Debye lengths in thickness The thickness of the barrier adjusts

itself so that the flux of electrons that have enough energy to go over the barrier to the

wall is just equal to the flux of ions reaching the wall.
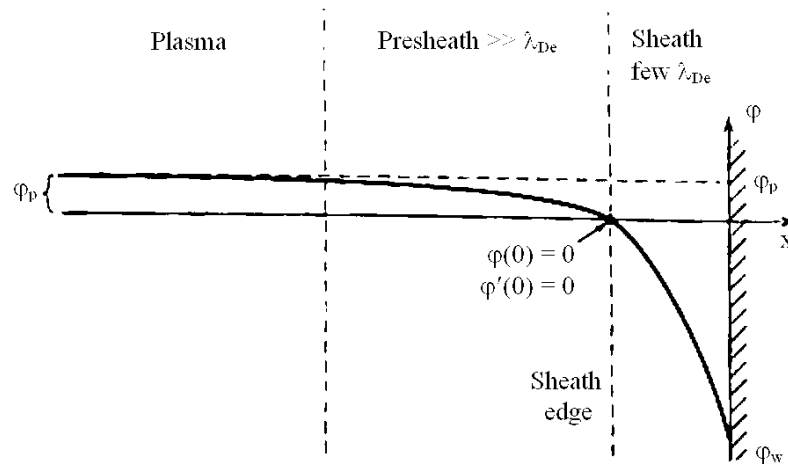
Figure 2.3 Qualitative behavior of sheath and presheath in contact
with a wall. [86]

To examine the exact behavior of $\varphi(x)$ in the sheath, one must treat the nonlinear

Poisson's equation. Figure 2.3 shows the situation near one of the wall. At the x point

far away from the wall, ions are imagined to enter the sheath region from the main

plasma with a drift velocity u_0. For simplicity, assume $T_i=0$, so all ions have the

velocity u_0 in the main plasma zone far away from the wall. The potential φ is

assumed to decrease monotonically with x.

If u(x) is the ion velocity, conservation of energy requires

$$\frac{1}{2}m_i u^2 = \frac{1}{2}m_i u_0^2 - e\varphi(x)$$

$$u = \left(u_0^2 - \frac{2e\varphi}{m_i}\right)^{1/2} \tag{2.3}$$

The ion equation of continuity then gives the ion density n_i in terms of the density n_0 in the main plasma:

$$n_0 u_0 = n_i(x) u(x) \tag{2.4}$$

$$n_i(x) = n_0 \left(1 - \frac{2e\varphi}{m_i u_0^2}\right)^{-1/2} \tag{2.5}$$

In steady state, the electrons will follow the Boltzmann relation closely:

$$n_e(x) = n_0 \exp\left(\frac{e\varphi}{T_e}\right) \tag{2.6}$$

Poisson's equation is then

$$\frac{d^2\varphi}{dx^2} = 4\pi e(n_e - n_i) = 4\pi e n_0\left[\exp\left(\frac{e\varphi}{T_e}\right) - \left(1 - \frac{2e\varphi}{m_i u_0^2}\right)^{-1/2}\right] \tag{2.7}$$

Equation (2.7) is the basic nonlinear equation governing the sheath potential and ion and electron densities.

2.3.2 The Bohm Sheath Criterion

A first integral of (2.7) can be obtained by multiplying it by $d\varphi/dx$ and integrating over x:

$$\int_0^\varphi \frac{d\varphi}{dx}\frac{d}{dx}\left(\frac{d\varphi}{dx}\right)dx = 4\pi e n_0 \int_0^\varphi \frac{d\varphi}{dx}\left[\exp\left(\frac{e\varphi}{T_e}\right) - \left(1 - \frac{2e\varphi}{m_i u_0^2}\right)^{-1/2}\right]dx \tag{2.8}$$

Cancelling the dx's and integrating with respect to φ, we obtain

$$\left(\frac{d\varphi}{dx}\right)^2 = 8\pi n_0 \left[T_e \exp\left(\frac{e\varphi}{T_e}\right) - T_e + m_i u_0^2 \left(1 - \frac{2e\varphi}{m_i u_0^2}\right)^{1/2} - m_i u_0^2 \right] \qquad (2.9)$$

where we have set φ = 0 and dφ/dx = 0 at infinity corresponding to a field free plasma.

Equation (2.9) can be integrated numerically to obtain φ (x). However, it is apparent

that the right hand side (RHS) of (2.9) should be positive for a solution to exist.

Physically this means that the electron density must always be less than the ion density

in the sheath region. In particular |φ| << 1, we expand the RHS of (2.9) to second order

in a Taylor series to obtain the inequality

$$\frac{1}{T_e} - \frac{1}{m_i u_0^2} \geq 0 \qquad (2.10)$$

One can also show that as -φ increases the RHS in equation (2.9) will monotonically

increase and, therefore, keep being positive, as long as the inequality in equation (2.10)

holds. The inequality gives us

$$u_0 \geq u_B = \left(\frac{T_e}{m_i}\right)^{1/2} \qquad (2.11)$$

The result is known as the Bohm sheath criterion. Same derivation can be found in Ref.

[86] or many other plasma text books. To give the ions this directed velocity u_0, there

must be a finite electric field in the plasma over some region, typically much wider

than the sheath, called presheath (see Figure 2.3). Hence the presheath region is not

strictly field free, although electric field is very small there. Since the field at the edge

between the sheath and the presheath is not precisely defined, only approximate

solutions are obtained by matching sheath to presheath solutions. Nevertheless, if we can make (2.11) sharper, by using the equality on the right, this relation is sufficient to obtain quantitative solutions for the plasma equilibrium. One can use the balance equation for ion flux and electron flux coupled with the equality in (2.11) to derive the potential drop within the sheath, therefore, to have the wall potential φ_w as

$$\varphi_w = -\frac{T_e}{e} \ln \sqrt{\frac{m_i}{m_e}} \qquad (2.12)$$

2.4 Guiding-Center Drift and Blob Motion

2.4.1 Guiding-Center Drift

Plasma motion can be broken down into a circular gyration with the motion for the instantaneous centre of this gyration. The center about which the particle gyrates is known as the guiding center. When some additional effect acts to make the radius of the particle orbit vary slowly, the guiding center drifts and particle moves. This is called drift motion. Several typical drift motions are as follows

A. E×B drift

The most basic type of fluid drift motion is the **E×B** drift. Think about a homogeneous magnetic field, both magnitude and direction constant in both time and space; an electric field superposed, perpendicular to the magnetic field; a single particle moving in the plane perpendicular to the magnetic field. Because the charged

particle is continuously accelerated and decelerated by electric field, it is going to have higher speed and larger gyro-radius on one side of the gyro-orbit and lower speed and smaller gyro-radius on the other side. This small velocity imbalance between the two sides amounts to a macroscopic drift of the guiding center. This is so-called $\mathbf{E}\times\mathbf{B}$ drift $\mathbf{v}_{E\times B}$ as follows

$$\mathbf{v}_{E\times B} = \frac{1}{c}\frac{\mathbf{E}\times\mathbf{B}}{B^2} \tag{2.13}$$

Note that the electric and magnetic forces are both perpendicular to $\mathbf{v}_{E\times B}$, and the $\mathbf{E}\times\mathbf{B}$ drift velocity is independent of particle's charge, q, and mass m.

B. ∇B+Curvature Drift

One can also calculate the ∇B drift, a guiding-center drift in a relatively simple inhomogeneous magnetic field, the lines of force are straight, but their density increases; and the curvature drift, in which the line or force is curved with a constant radius R and |B| is a constant.

In toroidal fusion device the curvature drift is always associated with the the ∇B drift with similar order of magnitude. Therefore, it is helpful to calculate ∇B drift and curvature drift together. Taking the configuration relations into account, the total drift in a toroidal vacuum field reads

$$\mathbf{v}_{\nabla B} + \mathbf{v}_R = \frac{m}{qc}\frac{\mathbf{R}\times\mathbf{B}}{R^2 B^2}\left(v_\parallel^2 + \frac{1}{2}v_\perp^2\right) \tag{2.14}$$

where **R** is the major radius of torus, **B** is the toroidal magnetic field, $v_\parallel$ is the velocity along **B**, and $v_\perp$ is the velocity perpendicular to **B**. Details of drift velocities' derivation and more types of guiding center drifts can be found in [85].

2.6.2 ∇B+Curvature Polarization and Blob Motion

Although originally born in a strong turbulence, blobs are seen to move as coherent objects in the SOL when we are going to study their dynamics. It's time to clarify at the moment that the ∇B+curvature polarization and the associated **E**×**B** drift are the main reasons pushing blob flowing outwards.
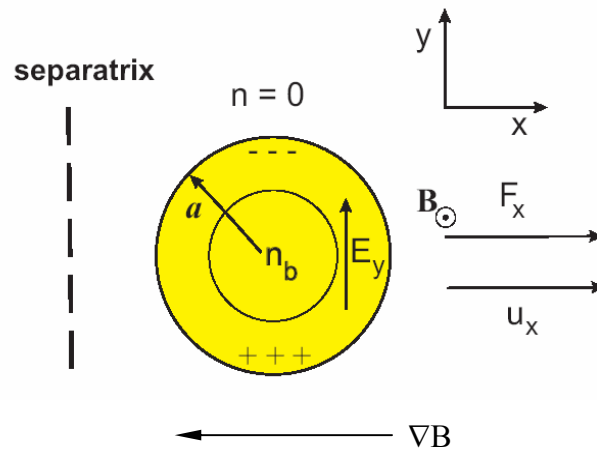
Figure 2.4 (Color) Sketch illustrating physics of blob charge polarization and transport in the SOL. [87]

In tokamak the ∇B+curvature drift of charged particle results in plasma polarization in blob as shown in Figure 2.4. In the blob (the yellow area) negative charged particles shift upwards a little bit and positive charged particles move downward due to the non-uniform magnetic field and toroidal curvature. Shifted

charged particles in opposite direction build up the local electric field within the blob. The corresponding $\mathbf{E} \times \mathbf{B}$ drift gives rise to plasma flow to the RHS. This flow can be very strong in the SOL because of the large effective "sheath resistivity" [88] when plasma contact with diverter targets at some distance from the separatrix where the effects of strong magnetic shear induced by X-point [89] can be neglected. Therefore, radial convective motion of blob requires two necessary conditions: (1) a mechanism to shift negative and positive particles in opposite directions, which can build up internal polarization inside blob; (2) a sufficiently slow parallel current (polarization charge loss) into sheaths, i.e. a strong enough sheath resistivity. In the case of Figure 2.4 it is the ∇B+curvature drift that creates the electric field within blob. In different fusion plasma devices the shifting power could be different. For instance, it could be centrifugal force or neutral wind effect in linear devices [90].

Chapter 3

Two Dimensional Models of Blob Dynamics

In this Chapter we will derive the reduced model equations, which describe blob motion across field lines under different conditions, referred to different closures in this Chapter. These governing equations are being used in the rest of our simulation work. However, before moving to the most important part of this thesis, the simulation research work, we apply a specific normalization rule on our equations to make them have very simple coefficients, which brings much convenience in programming and adjusting parameters in our models. Even more, very important characteristic values of scale length, scale time, and electric potential are dug out in this normalization process. At the end of this Chapter, we do a linear stability analysis on our equations.

3.1 Governing Equations

Basically we are using mass continuity equation and macroscopic two-fluid equations for electron and ion momentum conservation to build up our 2D model. We rewrite those equations as follows.

Mass continuity: $\dfrac{\partial n}{\partial t} + \nabla \cdot (n\mathbf{v}) = S$ (3.1)

Momentum conservation:

For electron: $m_e n_e \dfrac{d\mathbf{v}_e}{dt} = -\nabla P_e - e\mathbf{E}n_e - \dfrac{e}{c}(\mathbf{v}_e \times \mathbf{B})n_e$ (3.2)

For ion: $m_i n_i \dfrac{d\mathbf{v}_i}{dt} = -\nabla P_i + e\mathbf{E}n_i + \dfrac{e}{c}(\mathbf{v}_i \times \mathbf{B})n_i$ (3.3)

Next we use quasi-neutrality assumption with $n_e \cong n_i$ and electric potential φ as $\mathbf{E} = -\nabla\varphi$. Also we set two orthogonal unit vectors $\mathbf{e}_\perp$ and $\mathbf{e}_\parallel$ associated with magnetic field lines. $\mathbf{e}_\perp$ is perpendicular to $\mathbf{B}$ field and $\mathbf{e}_\parallel$ is parallel to $\mathbf{B}$. Decoupled to the new components, the total derivative and gradient operators read

$$\frac{d}{dt} = \frac{\partial}{\partial t} + \mathbf{v} \cdot \nabla = \frac{\partial}{\partial t} + \mathbf{v}_\perp \cdot \nabla_\perp + \mathbf{v}_\parallel \cdot \nabla_\parallel$$

Considering the uniform assumption along the magnetic field lines, $\nabla_\perp$ term is always much larger than $\nabla_\parallel$ term. Now we decompose the electron and ion momentum equations in $\perp$ and $\parallel$ components and just consider the $\perp$ component balance equation at this moment. We have

For electron: $m_e n\left(\dfrac{\partial}{\partial t} + \mathbf{v}_{e\perp} \cdot \nabla_\perp\right)\mathbf{v}_{e\perp} = -\nabla_\perp P_e + en\nabla_\perp \varphi - \dfrac{e}{c}(\mathbf{v}_{e\perp} \times B)n$ (3.4)

For ion: $m_i n\left(\dfrac{\partial}{dt} + \mathbf{v}_{i\perp} \cdot \nabla_\perp\right)\mathbf{v}_{i\perp} = -\nabla_\perp P_i - en\nabla_\perp \varphi + \dfrac{e}{c}(\mathbf{v}_{i\perp} \times \mathbf{B})n$ (3.5)

For equation (3.4), left hand side (LHS) can be neglected because electron mass is very small comparing with other terms. Then electron momentum equation becomes

(3.6)

$$\frac{B}{c} n \left(\mathbf{v}_{e\perp} \times \mathbf{e}_{\parallel} \right) - n \nabla_{\perp} \varphi + \frac{T_e}{e} \nabla_{\perp} n = 0$$

Where $P_e = T_e n$. T_e is assumed to be a constant.

Take $\mathbf{e}_{\parallel}$ cross product to equation (3.6) and reorganize the form to be

$$v_{e\perp} = \frac{c}{B} \left(\mathbf{e}_{\parallel} \times \nabla_{\perp} \varphi \right) - \frac{T_e c}{eB} \left(\mathbf{e}_{\parallel} \times \nabla_{\perp} (\ln n) \right) \tag{3.7}$$

For equation (3.5), assume $T_i = P_i = 0$ and speed of ion is very small. The zero order form of ion momentum equation becomes

$$\left(\mathbf{v}_{i0} \times \mathbf{e}_{\parallel} \right) = \frac{c}{B} \nabla_{\perp} \varphi \tag{3.8}$$

Taking $\mathbf{e}_{\parallel}$ cross product to both sides of the equation above, we have

$$\mathbf{v}_{i0\perp} = \frac{c}{B} \left(\mathbf{e}_{\parallel} \times \nabla_{\perp} \varphi \right) \tag{3.9}$$

This is in agreement with electron velocity at zero order because $\mathbf{v}_{e0\perp} = \mathbf{v}_{i0\perp} = c(\mathbf{E} \times \mathbf{B}) / B^2$, which is just the E×B drift velocity. However, we need to find another way to figure out first order form for speed of ion.

Assume $\mathbf{v}_i = \mathbf{v}_{i0} + \mathbf{v}_{i1}$ ($v_{i1} \ll v_{i0}$), then the first order equation of $\mathbf{v}_i$ becomes:

$$\frac{d_{\perp} \mathbf{v}_{i0}}{dt} = \Omega_i \left(\mathbf{v}_{i1} \times \mathbf{e}_{\parallel} \right) \tag{3.10}$$

where $\Omega_i = eB / cm_i$ is the ion cyclotron frequency, and total derivative $d_{\perp} / dt = \left(\partial / \partial t + \mathbf{v}_{i0\perp} \cdot \nabla \right)$. By a couple of steps as the following, we derive the $\mathbf{v}_{i1\perp}$.

$$\mathbf{v}_{i1\perp} = \frac{1}{\Omega_i} \frac{d_{\perp}}{dt} \left(\mathbf{e}_{\parallel} \times \mathbf{v}_{i0} \right) = \frac{1}{\Omega_i} \frac{d_{\perp}}{dt} \left(\mathbf{e}_{\parallel} \times \left(\frac{c}{B} \left(\mathbf{e}_{\parallel} \times \nabla_{\perp} \varphi \right) \right) \right) = -\frac{m_i c^2}{eB^2} \frac{d_{\perp}}{dt} \nabla_{\perp} \varphi \tag{3.11}$$

So we have the full form of ion velocity as

$$\mathbf{v}_i = \frac{c}{B}\left(\mathbf{e}_\parallel \times \nabla\varphi\right) - \frac{m_i c^2}{eB^2}\frac{d_\perp}{dt}\nabla_\perp\varphi \tag{3.12}$$

Taking the current conservation law into account

$$\nabla \cdot \mathbf{j} = 0 \tag{3.13}$$

and decouple it in components of $\mathbf{e}_\perp$ and $\mathbf{e}_\parallel$

$$\nabla_\perp \mathbf{j}_\perp + \nabla_\parallel \mathbf{j}_\parallel = 0 \tag{3.14}$$

Integrate above equation along the field line.

$$\int_0^L \left(\nabla_\perp \cdot \mathbf{j}_\perp + \nabla_\parallel \cdot \mathbf{j}_\parallel\right)d\mathbf{l}_\parallel \cong 0 \tag{3.15}$$

By the sheath condition, we have

$$L_\parallel \nabla_\perp \cdot \mathbf{j}_\perp + 2enC_s\left(1 - \sqrt{\frac{m_i}{m_e}}e^{-\frac{e\varphi}{T_e}}\right)\Bigg|_{sheat} = 0 \tag{3.16}$$

where $\nabla_\perp \cdot \mathbf{j}_\perp$ term can be written as

$$\nabla_\perp \cdot \mathbf{j}_\perp = \nabla_\perp \cdot ne\left(-\frac{m_i c^2}{eB^2}\frac{d_\perp}{dt}\nabla_\perp\varphi + \frac{c}{neB}\left(\mathbf{e}_\parallel \times \nabla_\perp P_e\right)\right)$$

$$= \nabla_\perp \cdot \left(-\frac{m_i c^2 n}{B^2}\frac{d_\perp}{dt}\nabla_\perp\varphi + \frac{c}{B}\left(\mathbf{e}_\parallel \times \nabla_\perp P_e\right)\right)$$

$$= -\frac{m_i c^2}{B^2}\nabla_\perp \cdot \left(n\frac{d_\perp}{dt}\nabla_\perp\varphi\right) + \frac{c}{B^2}\frac{\partial B}{\partial x}\frac{\partial P_e}{\partial y} \tag{3.17}$$

where we assume B = B(x), but it is only considered in the driving force term

Meanwhile, decompose electric potential φ into wall potential φ_w and fluctuant

potential $\delta\varphi$, i.e. $\varphi = \varphi_w + \delta\varphi$. The second term in equation (3.16) reads

$$2enC_s\left(1 - \sqrt{\frac{m_i}{m_e}}e^{-\frac{e\varphi}{T_e}}\right) = 2enC_s\left(1 - \sqrt{\frac{m_i}{m_e}}e^{-\frac{e\varphi_w + e\delta\varphi}{T_e}}\right) \tag{3.18}$$

$$= 2enC_s\left(1 - e^{-\frac{e\delta\varphi}{T_e}}\right) \cong 2e^2nC_s\frac{\delta\varphi}{T_e}$$

where we use the ambipolar plasma flow as in equation (2.12) for φ_w and assume

$|e\delta\varphi/T_e| \ll 1$.

Combining equations (3.16), (3.17), and (3.18) together, we get

$$-\frac{m_ic^2}{B^2}\nabla_\perp\left(n\frac{d_\perp}{dt}\nabla_\perp\varphi\right) + \frac{c}{B^2}\frac{\partial B}{\partial x}\frac{\partial P}{\partial y} + \frac{2e^2nC_s\frac{\delta\varphi}{T_e}}{L_\parallel} = 0 \tag{3.19}$$

where $\partial B/\partial x = -B/R$, and φ_w is independent of time, so

$(\nabla_\perp\varphi) = d_\perp/dt(\nabla_\perp\delta\varphi)$, then drop off δ, we get

$$\frac{m_ic^2}{B^2}\nabla_\perp\cdot\left(n\frac{d_\perp}{dt}\nabla_\perp\varphi\right) + \frac{c}{BR}\frac{\partial P}{\partial y} = \frac{2e^2nC_s\frac{\varphi}{T_e}}{L_\parallel} \tag{3.20}$$

Let $\phi = e\varphi/T_e$, and use $C_s = \sqrt{T_e/m_i}$; $\Omega_i = eB/(m_ic)$; $\rho_s = C_s/\Omega_i$, after some

algebra, we finally derive,

$$\rho_s^2\nabla_\perp\cdot\left(n\frac{d_\perp}{dt}\nabla_\perp\phi\right) + \frac{2\rho_sC_s}{R}\frac{\partial n}{\partial y} = \frac{2C_s}{L_\parallel}n\phi \tag{3.21}$$

Note that the factor 2 in second term comes from taking the directional variation

of unit vector $\mathbf{e}_\parallel$ into account. This is so-called vorticity equation (see for example

Refs. [88, 91, 92] and [35, 36, 93]). It is coupled with mass continuity equation as the following, where S is density source, to build our 2D blob model in the SOL (D in equation (3.22) is the diffusion coefficient).

$$\frac{d_\perp n}{dt} = D\nabla_\perp^2 n + S \tag{3.22}$$

In the absence of ambient plasma the equations (3.21) and (3.22) allow the solution in the form of travelling wave

$$n(x, y, t) = n_b(x\text{-}v_b t)\exp\left\{-\left(\frac{y}{\delta_y}\right)^2 - \frac{2C_s t}{L_\parallel}\right\} \tag{3.23}$$

where v_b is an arbitrary function, δ_y is the effective poloidal width of the blob, and

$$v_b = 2C_s\left(\frac{\rho_s}{\delta_y}\right)^2 \frac{L_\parallel}{R} \tag{3.24}$$

is the velocity of the blob.

Further research shows that the vorticity equation consists of the inertia term, the driving term, and the parallel current term. It can be written in a more general way as follows.

$$\rho_s^2 \nabla \cdot \left(n\frac{d}{dt}\nabla\phi\right) + \frac{2\rho_s C_s}{R}\frac{\partial n}{\partial y} = \hat{\mu}(\phi), \tag{3.25}$$

where the operator $\hat{\mu}(\phi)$ describes different closures for the dissipation effects and gives the relation between electrostatic potential and the parallel current.

So far the major attention is paid to the sheath-limited model. The model deals with the blob sitting on magnetic field lines in the SOL which are going through conductive material surfaces (Figure 3.1) and assumes that the relation between the

electrostatic potential and parallel current is determined by the sheath boundary conditions. It is simply to see that, for this closure, we have

$$\hat{\mu}(\phi) = \hat{\mu}_{SOL}(\phi) \equiv \frac{2C_s}{L_{\parallel}} n\phi \qquad\qquad\qquad (3.26)$$
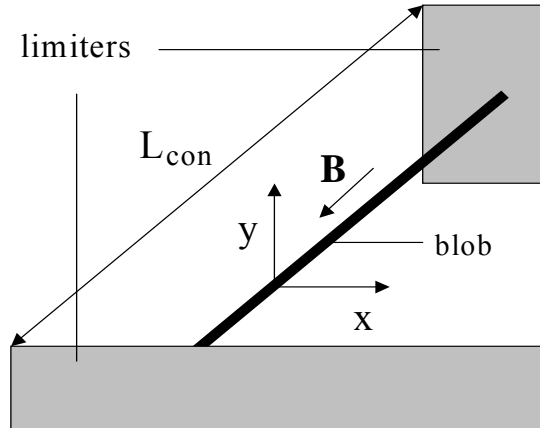
Figure 3.1 Schematic view of 3D blob geometry. Blob sits on the magnetic field lines going through conductive material surfaces.

Other limitations of the closure $\hat{\mu}(\phi)$ are related to simple models corresponding to different magnetic field geometries. For example, closure (3.26) cannot be used to describe blob dynamics in the vicinity of the separatrix where strong magnetic shear squashes the magnetic flux tube at X-point so strongly that perpendicular resistivity of plasma becomes important [94]. Meanwhile, it cannot describe the dynamics of blobs with high plasma beta, which can cause so significant bending of magnetic field lines that blob can penetrate deeply into the SOL region while the magnetic field lines, blob sitting on, still do not intersect the material surfaces, as shown in Figure 3.2. These two issues were addressed in [42] (see also review [95]). It is shown that taking into

account current flow along the field lines toward the X-point and the cross-field resistivity effects in the vicinity of it we have

$$\hat{\mu}(\phi) = \hat{\mu}_X(\phi) \sim \frac{2C_s}{L_b} \frac{\rho_s}{\delta_b} n\phi \qquad (3.27)$$

where L_b is the blob parallel length (the length of the region with increased plasma density/pressure). Somewhat different approach for the closure at the X-point was considered in [96].

For the case of the high beta blob plasma we estimate the perturbation of the magnetic field due to the blob motion, which is similar to that made in the study of the pellet cloud evolution [97, 98]. In this case, plasma polarization current is balanced by parallel current dipole

$$j_{\parallel} \sim enC_s \frac{\rho_s}{\delta_b} \frac{L_b}{R} \qquad (3.28)$$

which gives the following magnitude of radial perturbation of the magnetic field strength, B_r,

$$\frac{B_r}{B} \sim \frac{4\pi}{c} j_{\parallel}\delta_b \sim \beta_b \frac{L_b}{R} \qquad (3.29)$$

where β_b refers to the value of $\beta = 8\pi P/B^2$ at blob position.

As a result, the magnetic field line bends in radial direction. Since bending of magnetic field like propagates along B with the Alfven velocity such quasi-steady state approximation of the magnetic field line structure can be considered if

$$\frac{V_b}{V_A} \gtrsim \frac{B_r}{B} \sim \beta_b \frac{L_b}{R} \qquad (3.30)$$

Then, taking into account the equations (3.24) and (3.27) for blob velocity, we find from inequality (3.30)

$$V_b < C_s \sqrt{\beta_b} \frac{L_b}{R} \qquad (3.31)$$
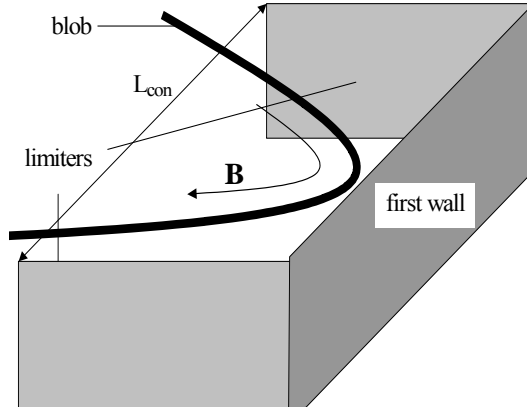
Figure 3.2 Schematic view of 3D blob geometry. Blob sits on highly bending magnetic field lines getting into SOL region without touching the material target.

However, at relatively large β_b bending of the magnetic field lines become so strong that the magnetic field line would "touch" first wall without even going through the material surfaces of divertor targets or limiters (see Figure 3.2). Taking into account expression (3.29), from Figure 3.2 one sees that such situation occurs for

$$\beta_b > \beta_{crit} \sim \frac{R\Delta_w}{L_\parallel^2} \qquad (3.32)$$

where we assume $L_b \approx L_\parallel$, Δ_w is the distance from last closed flux surface to the first wall. In order to describe the evolution of blobs with $\beta_b > \beta_{crit}$ within the framework of simple 2D model we use the approach adopted in the studies of the dynamics of

pellet clouds [97, 98]. Introducing vector potential $A_{\parallel}$ and taking into account that the bending of magnetic field propagates along the field line with Alfven speed from relation $E_{\parallel} = -\nabla_{\parallel}\varphi - (1/c)\partial A_{\parallel}/\partial t = 0$ we find $\varphi = (1/c)V_A A_{\parallel}$ and, correspondingly,

$$j_{\parallel} = -\frac{c^2}{4\pi V_A}\nabla_{\perp}^2\varphi \tag{3.33}$$

Substituting (3.33) into (3.13) we find

$$\hat{\mu}(\phi) = \hat{\mu}_{\beta}(\phi) \equiv -\frac{2V_A}{L_b}n_{amb}\rho_s^2\nabla_{\perp}^2\phi \tag{3.34}$$

where n_{amb} is ambient plasma density away from the blob and V_A is the Alfven speed calculated with the density of ambient plasma.

We notice that equations (3.22), (3.25), and (3.34) can be considered as a nonlinear stage of the ballooning instability, which in a "weakly nonlinear" approximation is discussed in [99]. These equations describe also ionospheric plasma flows with ion-neutral friction as well as fluid flow in porous medium [100]. We also remind that in the case where dissipation in equation (3.25) is due to cross-field plasma viscosity we have

$$\hat{\mu}(\phi) = \hat{\mu}_{\nu}(\phi) \equiv \nu n\rho_s^2\nabla_{\perp}^4\phi \tag{3.35}$$

where ν is the coefficient of molecular viscosity. As one sees, plasma viscosity has the highest order of derivative and, therefore, the closures [(3.26) - (3.34)] should dominate in mesoscale structures while (3.35) is dominant in very small scales.

In the following Chapters, we will present simulation results of blob dynamics for the closure (3.26) (the SOL case) and the closure (3.34) describing high beta blob

dynamics (the HB case). From now on we are going to use the expressions, the SOL blob, the SOL model, or the SOL case; also the HB blob, the HB model, or the HB case. The "SOL" refers to the physical situation governed by the closure (3.26) and the "HB" refers to the physical situation governed by the closure (3.34), in stead of spatially referring to the scrape-off-layer and the high β region.

3.2 Normalization

As stated in previous section, our next work is doing numerical simulation for the closure (3.26) (the SOL case) and closure (3.34) (the HB case). Before that we are going to normalize our equations into simpler form. Different plasma facilities have quite different parameters such as major radius, plasma densities, connection length etc., changing in a wide range. To make our analysis more general, we normalize our models. The final goal of our normalization process is to make all coefficients in (3.25) to be unity. This approach is very important not only because it makes the form of equations simpler and reduces tons of unnecessary work in numerical simulation, but also highlights the characteristic scale length and time scale at the end.

For the closure (3.26), we use

$$\tilde{n} = \frac{n}{n_0} \qquad \tilde{x} = \frac{x}{\delta_*} \qquad \tilde{y} = \frac{y}{\delta_*}$$

$$\tilde{t} = \frac{t}{t_*} \qquad \tilde{\phi} = \frac{\phi}{\phi_*} \qquad v_* = \frac{\delta_*}{t_*}$$

(3.36)

where n_0 is the initial highest density value in our simulation domain and the upper tilde is a symbol of normalized variable. The characteristic scale length δ_* and time scale t_* can be derived in the way to let all coefficients be of unity.

$$\delta_* = \rho_s \left(\frac{L^2}{2R\rho_s}\right)^{1/5} \qquad t_* = \frac{(\delta_*)^3 R}{L\rho_s^2 C_s} \tag{3.37}$$

Also ϕ_* and v_* read

$$\phi_* = \frac{L\rho_s}{R\delta_*} \qquad v_* = \frac{L\rho_s^2 C_s}{R(\delta_*)^2} \tag{3.38}$$

Plugging all [(3.36) - (3.38)] into equation (3.21) and dropping the upper tilde at the end, eventually we get simpler form of the SOL case as

$$\nabla \cdot \left(n \frac{d}{dt} \nabla \phi\right) + \frac{\partial n}{\partial y} - n\phi = 0 \tag{3.39}$$

and continuity equation becomes

$$\frac{dn}{dt} = \frac{DR\delta^*}{L\rho_s^2 C_s} \nabla^2 n \tag{3.40}$$

Note that the dimensionless E×B drift velocity reads

$$v = \left(\frac{\partial \phi}{\partial y}, -\frac{\partial \phi}{\partial x}\right) \tag{3.41}$$

For closure (3.34), the HB case, governing equation reads

$$\rho_s \nabla \cdot \left(n \frac{d}{dt} \nabla \phi\right) + \frac{2C_s}{R} \frac{\partial n}{\partial y} + \frac{2V_A}{L_\parallel} n_{amb}\rho_s \nabla^2 \phi = 0 \tag{3.42}$$

we also use the normalization scheme in (3.36). It turns out that the characteristic scale length δ_* and scale time t_* are:

$$\delta_* = \frac{C_s^2 L_\parallel^2}{2\alpha^2 R V_A^2} \qquad\qquad t_* = \frac{L_\parallel}{2\alpha V_A} \qquad\qquad (3.43)$$

Where $\alpha = n_{amb}/n_0$. Also ϕ_* and v_* read

$$\phi_* = \frac{C_s^3 L_\parallel^3}{2\alpha^3 V_A^3 R^2 \rho_s} \qquad\qquad v_* = \frac{C_s^2 L_\parallel}{\alpha R V_A} \qquad\qquad (3.44)$$

Finally the HB case is simplified as

$$\nabla \cdot \left(n \frac{d}{dt} \nabla \phi \right) + \frac{\partial n}{\partial y} + \nabla^2 \phi = 0 \qquad\qquad (3.45)$$

and associated continuity equation becomes

$$\frac{dn}{dt} = \frac{2D\alpha^3 V_A^3 R^2}{C_s^4 L_b^3} \nabla^2 n \qquad\qquad (3.46)$$

We notice that in continuity equations (3.40) and (3.46), the only thing changed is that the diffusivity D multiplied by a constant. Therefore, using "D" to replace the whole thing in front of $\nabla^2 n$, the form of continuity equation will not be changed and read as same as Eq. (3.22). The new D is the normalized diffusivity. In our work, normalized diffusivity D is set to be a very small number which helps in numerical stabilization but not kills the interesting dynamics in the model. We will also discuss diffusivity effect in Chapter 5.

There are a couple of advantages with this normalized model. Firstly all the facility-related parameters are wrapped up. So it gives us an opportunity to use this simple 2D model to explain more general physical phenomena without considering the effect associated with particular experimental parameters. Secondly the characteristic length scale δ_*, time scale t_*, and characteristic velocity v_* are highlighted. To give

an idea about the magnitude of δ_*, t_*, and v_* we calculate them for several current running toroidal plasma devices as follows

Table 3.1 δ_*, t_*, and v_* for typical fusion plasma devices.

	DIIID	C-Mod	NSTX	ITER
$L_\parallel$(cm)	1750	700	850	6200
R(cm)	175	70	85	620
B(gauss)	22000	50000	3000	53000
T_e(eV)	100	80	50	300
n	2×10^{13}	7×10^{13}	5×10^{12}	1×10^{14}
C_s(cm/s)	7×10^6	6×10^6	5×10^6	1.2×10^7
ρ_s(cm)	0.066	0.026	0.34	0.047
$(\delta_*)_{SOL}$(cm)	0.70	0.27	2.25	0.69
$(t_*)_{SOL}$(s)	1.1×10^{-6}	5×10^{-7}	2×10^{-6}	1.22×10^{-6}
$(v_*)_{SOL}$(cm/s)	6.2×10^5	5.5×10^5	1.1×10^6	5.6×10^5
$(\delta_*)_{HB}$(cm)	0.73	0.16	2.37	6.7
$(t_*)_{HB}$(s)	$1.\times10^{-6}$	3.8×10^{-7}	2.1×10^{-6}	3.8×10^{-6}
$(v_*)_{HB}$(cm/s)	6.3×10^5	4.2×10^5	1.1×10^6	1.8×10^6

One can use these real unit values to correlate our normalized solutions to the real experimental results, and check the corresponding key length and time scales in real devices. It is worthy to note that the scale length, δ_*, for all devices is in order of 1 cm and velocity is in order of 10^5 cm/s. This is in agreement with experimental measurements in SOL in tokamak. Thirdly with these normalized unity coefficient equations, it is much easier to weigh the contribution of each term in the model, and then find leading terms. We will see this in the following qualitative analysis.

Comparing the magnitude of each term in equation (3.39) and (3.45), we can assume the spatial derivative, either $\partial/\partial x$ or $\partial/\partial y$, is in order of δ^{-1}. δ is the scale-length of the characteristic density variation. Neglecting the time derivative in inertial term at the moment, it is simply to derive that the order of inertial term, driving force term and current term in (3.39), the SOL case, are δ^{-6}, δ^{-1}, and δ^{-1} respectively, and δ^{-2}, δ^{-1}, and δ^{-1} for (3.45), the HB case. These magnitude comparisons unveil two important properties of our model. First one is that both SOL and HB cases are sensitive to the structure length scale. For coherent structure larger than unity, $\delta > 1$, the inertia term δ^{-6} in (3.39) and δ^{-2} in (3.45) are very small comparing with the other two term, so the inertia term can be ignored, and the models are dominated by the other two terms left. Large scale model without inertia term has been clearly demonstrated in [101]. Second property is for small spatial scale structure. When $\delta \leq 1$, the inertia effect comes in. One could expect strong KH instability coming in when the inertia term becomes dominant with strong velocity shear. Also we notice that, in the SOL case, the ratio between inertia term and the other two terms is δ^{-5}, but this ratio is δ^{-1} in the HB case. Therefore we can imagine that when δ is getting smaller than unity the inertia effect in the SOL model increases much faster than in HB model. So the motion mode in the SOL case would have a much stronger change than in the HB case as the δ changes from one side of unity to the other side. In addition, using the scaling analysis to evaluation the E×B drift velocity, one can derive that v_{SOL} is proportional

to $1/\delta^2$ and v_{HB} is independent of the scale length δ. All these conclusions from scaling analysis are approved by the simulation results in Chapter 5 and Chapter 6.

3.3 Local Stability Analysis

Next we consider local linear stability analysis of two simple one dimensional structures, which to some extent resemble blobs [equation (4.11)] in the limits $\delta_x \to \infty$ or $\delta_y \to \infty$. We take the perturbations to be proportional to $\exp(-i\omega t + i\mathbf{k} \cdot \mathbf{r})$, where ω and $\mathbf{k}$ are the frequency and the wave number respectively. Then neglecting plasma leakage to the plates and diffusion, linearizing equation (3.39), and taking into account that $|k_x|\delta > 1$, $|k_y|\delta > 1$, we find the following dispersion relations for both limits.

3.3.1 Linear Stability Analysis of the SOL Model

When $\delta_y \to \infty$ in equation (4.11), zero order plasma density, n_0, depends only on x, i.e. $n_0 = \exp\left(-x^2/\delta_x^2\right)$, which can been seen as a poloidal elongated blob. One can calculate that the zero order potential is formulated as $\phi_0 = -\partial \ln n_0 / \partial y = 0$ (constant). We need also the first order first order small perturbed fluctuation as follows:

$$
\begin{aligned}
n_1 &= n_1 \exp(i(\mathbf{k} \cdot \mathbf{r} - \omega t)) \\
\phi_1 &= \phi_1 \exp(i(\mathbf{k} \cdot \mathbf{r} - \omega t))
\end{aligned}
$$

(3.47)

neglect all other higher order fluctuations and plug zero and first order values into vorticity and continuity equations, we have

$$\left(i\omega n_0 k^2 - n_0\right)\phi_1 + ik_y n_1 = 0 \tag{3.48}$$

$$ik_y \frac{dn_0}{dx}\phi_1 + i\omega n_1 = 0 \tag{3.49}$$

Equation (3.48) is from vorticity equation and (3.49) from continuity equation. Note that for this poloidal elongated structure zero order velocity goes to zero, $\mathbf{v}_0 = -\nabla\phi_0 \times \hat{\mathbf{z}} = 0$; and the first order convention term can be written as

$$\mathbf{v}_1 \cdot \nabla n_0 = \frac{\partial\phi_1}{\partial x}\frac{\partial n_0}{\partial y} - \frac{\partial\phi_1}{\partial y}\frac{\partial n_0}{\partial x}$$

Equation (3.48) and equation (3.49) are coupled together. To have non-zero solutions for ϕ_1 and n_1, the determinant of the coefficient matrix must be zero. By this we have the dispersion relation as follows

$$\omega^2 + \frac{i}{k^2}\omega - \frac{k_y^2}{k^2 n_0}\frac{dn_0}{dx} = 0 \tag{3.50}$$

Solutions of this quadratic equation can be easily derived as

$$\omega = -\frac{i}{2k^2} \pm \sqrt{-\frac{1}{4k^4} + \frac{k_y^2}{k^2 n_0}\frac{dn_0}{dx}} \tag{3.51}$$

For radial elongated structure, $\delta_x \to \infty$ in equation (4.11) Zero order density and potential read

$$n_0 = \exp\left(-\frac{y^2}{\delta_y^2}\right) \tag{3.52}$$

$$\phi_0(y) = -\frac{1}{n_0}\frac{dn_0}{dy} \qquad (3.53)$$

Linearize first order variables as in equation (3.47) again, also cancel out the zero order balance and let

$$\varpi = \omega - \mathbf{k}\cdot\mathbf{v}_0 \qquad (3.54)$$

where $\mathbf{v}_0$ is the unperturbed plasma velocity. We derive first order balance equation for vorticity equation

$$(i\varpi n_0 k^2 - n_0)\phi_1 + (ik_y - \phi_0)n_1 = 0 \qquad (3.55)$$

and for continuity equation

$$ik_x \frac{dn_0}{dy}\phi_1 - i\varpi n_1 = 0 \qquad (3.56)$$

Note in this case zero order velocity v_0 is not zero but a constant. To have non-zero solutions for the two-coupled equations, again, the determinant coefficient matrix must be zero, then we have

$$\varpi^2 + \frac{i}{k^2}\varpi + \frac{k_x k_y}{k^2 n_0}\frac{dn_0}{dy} + i\frac{k_x \phi_0}{k^2 n_0}\frac{dn_0}{dy} = 0 \qquad (3.57)$$

$$\varpi = -\frac{i}{2k^2} \pm \sqrt{-\frac{1}{4k^4} - \frac{k_x k_y}{k^2 n_0}\frac{dn_0}{dy} - i\frac{k_x \phi_0}{k^2 n_0}\frac{dn_0}{dy}} \qquad (3.58)$$

As we see from equations (3.51) and (3.58) simple 1D structure can be unstable with respect to RT type of instability with some modification due to the sheath effects (see for example Ref. [88]). In the case $\delta_y \to \infty$, the instability requires $d\ln(n_0)/dx < 0$ and the most unstable perturbations are those with $|k_y| \gg |k_x|$, while for $\delta_x \to \infty$, both negative and positive derivatives of the density, $d\ln(n_0)/dy$, are unstable (instability

requires $k_x k_y dln(n_0)/dy > 0$) and the most unstable perturbations are those with $|k_y| = |k_x|$.

In both cases $\delta_x \to \infty$ and $\delta_y \to \infty$, scale dependence of the growth rates, γ, on the wave number and blob scale has the form

$$\gamma = \frac{k^2}{\delta_b} < \gamma_{max} \sim \frac{1}{\sqrt{\delta_b}} \quad \text{for} \quad k^2 < \sqrt{\delta_b} \qquad (3.59)$$

$$\gamma \approx \gamma_{max} \quad \text{for} \quad k^2 > \sqrt{\delta_b} \qquad (3.60)$$

where δ_b is the spatial scale of 1-D "blob" in the x or y direction. Due to the restriction $k\delta_b > 1$ of our local analysis, from equations (3.59) and (3.60) we can estimate the growth rate of the perturbations with large spatial scales, which are somewhat comparable to δ_b ($k\delta_b \geq 1$):

$$\gamma \approx \frac{1}{\delta_b^3} \sim \frac{v_b}{\delta_b} \quad \text{for} \quad \delta_b > 1 \qquad (3.61)$$

$$\gamma \approx \gamma_{max} \approx v_b \delta_b^{3/2} < \frac{v_b}{\delta_b} \quad \text{for} \quad \delta_b < 1 \qquad (3.62)$$

where normalized blob velocity $v_b = 1/\delta_b^2$. More about nonlocal analysis of blob linear stability can be found in Ref. 27. From (11) we see that for blobs with large spatial scale $\delta_b > 1$, the instability develops in a so short time scale, determined by the growth rate from equation (3.61) $\tau_{inst} = \Lambda/\gamma \approx \Lambda\delta_b/v_b$ (Λ is a numerical factor of the order of a few), that blob barely moves to a distance comparable to its own size. While blob has small spatial scale $\delta_b < 1$, the instability develops at $\tau_{inst} = \Lambda/\gamma_{max}$ and blob moves radially to a large distance $\tau_{inst}v_b = \Lambda v_b/\gamma_{max} \approx \Lambda (\delta_b)^{-3/2} > 1 > \delta_b$. Thus we can

conclude that it is unlikely that blobs with large spatial scale $\delta_b > 1$ can move radially as coherent structures, while blobs with $\delta_b < 1$ seem to be able to move as coherent structures to large distances.

3.3.2 Linear Stability Analysis of the HB Model

In this section, we are going to apply linear stability analysis on the HB blob with the same initial one dimensional perturbations and very similar derivations.

For the poloidally elongated blob, $\delta_y \to \infty$, linearize first order variables as in equation (3.47), plug into governing equations, and cancel out the zero order balance, then we have

$$\left(i\varpi n_0 k^2 - k^2\right)\phi_1 + ik_y n_1 = 0 \tag{3.63}$$

$$ik_y \frac{\partial n_0}{\partial x}\phi_1 + i\varpi n_1 = 0 \tag{3.64}$$

To have non-zero solutions for ϕ_1 and n_1, the determinant of the coefficient matrix must be zero. So we have the dispersion relation as follows

$$\varpi^2 + \frac{i}{n_0}\varpi - \frac{k_y^2}{k^2 n_0}\frac{dn_0}{dx} = 0 \tag{3.65}$$

$$\varpi = -\frac{i}{2n_0} \pm \sqrt{-\frac{1}{4n_0^2} + \frac{k_y^2}{k^2 n_0}\frac{dn_0}{dx}} \tag{3.66}$$

Radial elongated perturbation has zero order density $n_0 = \exp\left(-y^2/\delta_y^2\right)$ and the corresponding $\phi_0 = \phi_0(y)$. The linearized first order equations read

$$(i\varpi n_0 k^2 - k^2)\phi_1 + ik_y n_1 = 0 \qquad (3.67)$$

$$ik_x \frac{dn_0}{dy}\phi_1 - i\varpi n_1 = 0 \qquad (3.68)$$

Non-zero solution gives us

$$\varpi^2 + \frac{i}{n_0}\varpi + \frac{k_x k_y}{k^2 n_0}\frac{dn_0}{dy} = 0 \qquad (3.69)$$

$$\varpi = -\frac{i}{2n_0} \pm \sqrt{-\frac{1}{4n_0^2} - \frac{k_x k_y}{k^2 n_0}\frac{dn_0}{dy}} \qquad (3.70)$$

The local analysis results of HB model are similar to their counterparts in SOL model. In the case $\delta_y \to \infty$, the instability requires $dln(n_0)/dx < 0$ and the most unstable perturbations are those with $|k_y| \gg |k_x|$, while for $\delta_x \to \infty$, both negative and positive derivatives of the density, $dln(n_0)/dy$, are unstable (instability requires $k_x k_y dln(n_0)/dy > 0$) and the most unstable perturbations are those with $|k_y| = |k_x|$. However, in HB model the stabilized term is proportional to $1/n_0$, instead of $1/k^2$ in SOL blob, this indicates that HB blob dynamics is less sensitive to blob scale length than SOL blob dynamics.

In both cases $\delta_x \to \infty$ and $\delta_y \to \infty$, scale dependence of the growth rates, γ, on the blob scale has the form

$$\gamma = \frac{1}{\delta_b} < \gamma_{max} \sim \frac{1}{\sqrt{\delta_b}} \quad \text{for } 1 < \delta_b \qquad (3.71)$$

$$\gamma \approx \gamma_{max} \sim \frac{1}{\sqrt{\delta_b}} \quad \text{for } 1 > \delta_b \qquad (3.72)$$

where δ_b is the spatial scale of 1-D "blob" in the x or y direction. Normalized blob velocity $v_b \sim 1$. From equation (3.71) we see that for blobs with large spatial scale δ_b >1, the instability develops in a so short time scale, determined by the growth rate from (10a) $\tau_{inst} = \Lambda/\gamma \approx \Lambda\delta_b$ (Λ is a numerical factor of the order of a few), that blob barely moves to a distance comparable to its own size. While blob has small spatial scale δ_b < 1, the instability develops at $\tau_{inst} = \Lambda/\gamma_{max}$ and blob moves radially to a large distance $\tau_{inst}v_b = \Lambda/\gamma_{max} \approx \Lambda \ (\delta_b)^{1/2} > \delta_b$. The result is similar to what we have in the SOL blob analysis. We can also conclude that it is unlikely that blobs with large spatial scale δ_b > 1 can move radially as coherent structures, while blobs with δ_b < 1 seem to be able to move as coherent structures to large distances.

3.4 Conclusion

This work has presented the derivation of the 2D SOL blob model. Different closures are discussed to make models with different closure describe several different physical situations. Our focus will on the SOL and HB models. A specific normalization scheme is introduced to reduce all coefficients in governing equations to be unity. Characteristic spatial and time scale are obtained from this normalization method. Spatial scale $\delta_* = \rho_s \left(L^2 /(2R\rho_s)\right)^{0.2}$ and time scale $t_* = \left(\delta_*\right)^3 R /(L\rho_s^2 C_s)$ are showed to be critical values in the SOL blob dynamics and $\delta_* = C_s^2 L_\parallel^2 /(2\alpha^2 RV_A^2)$ and $t_* = L_\parallel /(2\alpha V_A)$ in the HB blob dynamics. It is unveiled that both the SOL and HB

cases are sensitive to the structure length scale. For coherent structure larger than δ_*, dissipation term becomes dominant. For structure smaller than δ_*, inertia term becomes dominant. δ_* is equal to one in the normalized model. In addition, blob dynamics in the SOL model could have a much stronger change than in the HB model as the δ changes from one side of δ_* to the other side. Meanwhile, by local linear stability analysis we find out that in both SOL and HB models simple 1D structure can be unstable. In the case $\delta_y \to \infty$, the instability requires $d\ln(n_0)/dx < 0$ and the most unstable perturbations are those with $|k_y| \gg |k_x|$, while for $\delta_X \to \infty$, both negative and positive derivatives of the density, $d\ln(n_0)/dy$, are unstable (instability requires $k_x k_y d\ln(n_0)/dy > 0$) and the most unstable perturbations are those with $|k_y| = |k_x|$. It is indicated that dynamics in HB model is less sensitive to blob scale length than dynamics in SOL model. We also conclude that it is unlikely that blobs with large spatial scale $\delta_b > 1$ can move radially as coherent structures, while blobs with $\delta_b < 1$ seem to be able to move as coherent structures to large distances. Meanwhile we list characteristic values of δ_*, t_*, and v_* for several popular toroidal plasma devices, such as DIII-D, NSTX, C-MOD, and ITER. It is worthy to note that the scale length, δ_*, for all devices is in order of 1 cm, and velocity is in order of 10^5 cm/s. This is in agreement with experimental measurements in SOL in tokamak.

Chapter 4

Numerical Scheme for Blob Simulation

As we describe in previous Chapters, many key features in the rather complicated transport phenomena are captured by the fairly simple 2D models in (3.39) and (3.45) coupled with continuity equation. However, analytically solving the problems without any extra assumption is very hard. Therefore, we use time-dependent numerical method to simulate blob dynamics in the middle age of its life. Next, we will introduce the structure of our 2D numerical model, such as governing equations, spatial grid system, numerical schemes adopted, boundary condition (B.C.) and initial condition (I.C.). Numerical resolution and data accuracy are also discussed in this Chapter.

4.1 Governing Equations

Even for the reduced 2D models (3.39) and (3.45), numerical solution is not easy to get because of the non-linear inertia term. To simplify our work, we neglect the density variation in inertia term and take the "n" out of the divergence in our models. Then we have

$$\frac{\partial}{\partial t}\nabla^2\phi + (\mathbf{v}\cdot\nabla)\nabla^2\phi + \frac{\partial \ln n}{\partial y} - \phi = 0 \tag{4.1}$$

$$n\frac{\partial}{\partial t}\nabla^2\phi + n(\mathbf{v}\cdot\nabla)\nabla^2\phi + \frac{\partial n}{\partial y} + \nabla^2\phi = 0 \tag{4.2}$$

This is so-called the Boussinesq approximation [102, 103, 104, 105, 106]. The essence of the Boussinesq approximation is the density difference in inertia term is neglected, but it is considered in driving term. Equation (4.1) and (4.2) (we expand the inertial term in there to clarify all the terms we need to deal with in our computational solver.) become RI-SOL and RI-HB equations and equation (3.39) and (3.45) are FI-SOL and FI-HB equations with RI referring to reduced inertial term and FI referring to full inertial term. RI equation is much easier to numerically solve than FI equation. However, we also try to solve the FI-SOL equation by applying relaxation scheme as discussed in section 4.3. This approach is also used in [107].

Meanwhile one should note that equation (4.1) and (4.2) are not closed. Each of them should couple with density continuity equation (4.3), which is in normalized form and neglects density source term, to form a closed system.

$$\frac{\partial n}{\partial t} + (\mathbf{v}\cdot\nabla)n = D\nabla_\perp^2 n \tag{4.3}$$

4.2 Grid System

A quasi-slab domain in edge plasma is chosen to be our simulation domain with boundary length L_x by L_y. It is evenly separated into an nx×ny rectangular grid system as shown in Figure 4.1, where nx and ny are integer numbers of nodes on each axis.

The width and height of each cell are denoted by Δx and Δy, and $\Delta x = Lx/(nx-1)$, $\Delta y = Ly/(ny-1)$. Neither nx and ny nor Δx and Δy should be identical to each other.
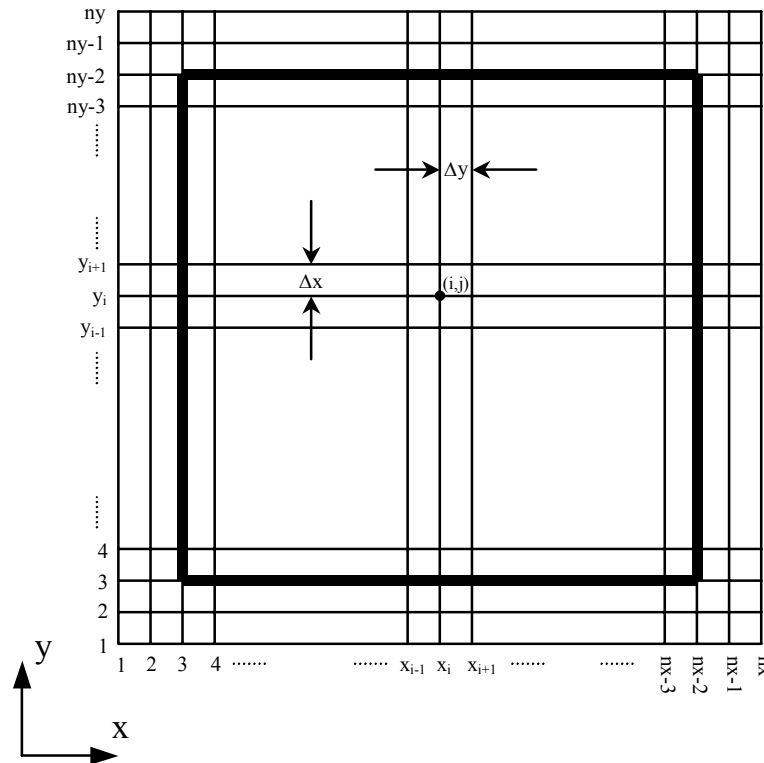
Figure 4.1 Grid system of simulation domain.

On the boundaries around the domain, we artificially pre-setup node value at $x_i = $ 1, 2, nx-1, and nx, and $y_i = $ 1, 2 ny-1, ny to satisfy our boundary condition discussed in section 4.4.1. So our effective calculation domain is from x = 3 to nx-2, and y =3 to ny-2, the area inside of the closed thicker bar in Figure 4.1. Therefore, our calculation amount is (nx-4)×(ny-4). However, for the reason of setting up boundary conditions, our real calculation domain is from x=3 to x=nx-2, and from y=3 to y=ny-2, the area

inside of the closed thicker bar in Figure 4.1. We are going to discuss this in section 4.4 in detail.

Depending upon the spatial discretization, the first and second spatial derivatives are chosen as follows.

$$\left(\frac{\partial f}{\partial x}\right)_{i,j} = \frac{f_{i-2,j} - 8f_{i-1,j} + 8f_{i+1,j} - f_{i+2,j}}{12\Delta x}$$

$$\left(\frac{\partial f}{\partial y}\right)_{i,j} = \frac{f_{i,j-2} - 8f_{i,j-1} + 8f_{i,j+1} - f_{i,j+2}}{12\Delta y}$$

(4.4)

$$\left(\frac{\partial^2 f}{\partial x^2}\right)_{i,j} = \frac{f_{i+1,j} - 2f_{i,j} + f_{i-1,j}}{\Delta x^2}$$

$$\left(\frac{\partial^2 f}{\partial y^2}\right)_{i,j} = \frac{f_{i,j+1} - 2f_{i,j} + f_{i,j-1}}{\Delta y^2}$$

(4.5)

Where f could be any variable. We use fourth-order central difference formula for the first derivative and second-order central difference formula for the second derivative.

4.3 Numerical Schemes Adopted

4.3.1 The Fourth-Order Runge-Kutta Method

In our numerical approach, we use the fourth-order Runge-Kutta (RK4) method in time advance. We choose RK4 scheme not only because it the most popular one in the Runge-Kutta family, but also because it has relatively larger domain of stability

comparing with other time advance methods [108]. Blob dynamics maybe unstable as we see from the preceding linear stability analysis. We will also see the instability evolution in numerical results later on. Therefore, we would like to have a more stable numerical scheme to make our model stabilized in numerical level. It turns out that RK4 is good in this mission. The following is a formula description of RK4 for symbol problem $dy/dt = f(y,t)$, where y could be seen as a vector containing all variables except time.

$$k_1 = f(y_n, t_n)$$
$$k_2 = f(y_n + \frac{h}{2}k_1, t_{n+1/2})$$
$$k_3 = f(y_n + \frac{h}{2}k_2, t_{n+1/2})$$
$$k_4 = f(y_n + hk_3, t_{n+1})$$
$$y_{n+1} = y_n + \frac{h}{6}k_1 + \frac{h}{3}(k_2 + k_3) + \frac{h}{6}k_4$$

(4.6)

4.3.2 The Fast Fourier Transform

In our simulation, we need to solve the Poisson's equation like $\Omega = \nabla^2 \phi$. We use the Fast Fourier Transform [109] (denoted by fft in Matlab) to solve it. In fact, we have two versions of solver for our model. One is programmed by Matlab for easy slover, the other by Fortran for faster calculation speed. In the Matlab code, we directly solve Possion's equation by taking the fft solver from Matlab. However, in the Fortran code, we use indirect iteration method, the relaxation method discuss in the next section, to get ϕ at each time step. By comparing the results from different codes, we surely know that both schemes are working fine.

4.3.3 The Relaxation Method

The equations (4.1) and (4.2) are in the Boussinesq approximation. Comparing with full version equations in (3.39)and (3.45), the first (inertial) term in each equaiton is replaced by computationally less demanding version. This method is extensively used in recent years to study blob dynamics. However, strictly speaking the Boussinesq approximation is not justified for the SOL region where the background plasma density is smaller than the blob plasma density. Therefore simplified equations should be verified with exact version of the first term.

Here we only give the solution for the SOL equation. To make (3.39) solvable, one can change the equation's form (Appendix A) as follows [110]

$$\frac{d}{dt}\Omega = -\frac{\partial E}{\partial x}\frac{\partial n}{\partial y} + \frac{\partial E}{\partial y}\frac{\partial n}{\partial x} + n\phi - \frac{\partial n}{\partial y} \tag{4.7}$$

$$\Omega = \nabla \cdot (n\nabla\phi) \tag{4.8}$$

$$E = \frac{1}{2}\left(v_x^2 + v_y^2\right) \tag{4.9}$$

Equation (4.7) can be solved by our normal schemes. However, equation (4.8) is much more difficult than the Poisson's equation. It cannot be directly solved by the FFT. To achieve our goal, we introduce relaxation method to solve equation (4.8). It is basically an iteration method with the formula as follows

$$\phi_{i,j}^{n+1} = (1 - \omega n_{i,j})\phi_{i,j} + \frac{\omega}{16}[(n_{i+1,j} - n_{i-1,j})(\phi_{i+1,j} - \phi_{i-1,j}) + (n_{i,j+1} - n_{i,j-1})(\phi_{i,j+1} - \phi_{i,j-1})$$

$$+ 4n_{i,j}(\phi_{i+1,j} + \phi_{i-1,j} + \phi_{i,j+1} + \phi_{i,j-1}) - 4\Omega_{i,j}\Delta x^2] \tag{4.10}$$

At each time step, $n_{i,j}$ and $\Omega_{i,j}$ are known and $\phi_{i,j}$ are unknown. This formula is special for spatial discretization $\Delta x = \Delta y$. The variable ω, sometimes called relaxation factor, is normally chosen as 1.2 in our simulation. This technique can be easily transplanted to the Poisson's equation with quite similar formula. Actually, we do use this method to solve the Poisson's equation in our Fortran code.

4.4 Initial and Boundary Conditions

4.4.1 Initial Conditions

In our numerical study we normally seed the Gaussian density blob as an initial condition, as in equation (4.11), with (x_0, y_0) the starting center of blob at t=0.

$$n_b(x, y, t=0) = \exp\left[-\left(\frac{x-x_0}{\delta_x}\right)^2 - \left(\frac{y-y_0}{\delta_y}\right)^2\right] + n_{bg} \qquad (4.11)$$

where δ_x and δ_y are the initial spatial scales of blob in the radial and poloidal directions, and n_{bg} is the background density (all in normalized units). In what follows, we mostly take n_{bg}=0.01, but in section 5.2.4 about high background research we use different values larger that 0.01 for n_{bg}. Figure 5.1 shows a circular density contour plot of a seeded blob, $\delta_x = \delta_y$. It is applied as initial condition most of the time in our simulation. However, one should note that it's not necessary to set δ_x and δ_y identical to each other. Oval blob with $\delta_x \neq \delta_y$ is also worthy to study and we will report our solutions in the next Chapter. Furthermore, our model is compatible to

more complicated density distribution such as biasing potential, zonal flow, pedestal region etc.

In most cases, initial potential is derived by the balance between the driving force and the current terms. The effect of initial potential will be discussed later on.

4.4.2 Boundary Conditions

Boundary conditions are set up as the following. In y direction, we use periodic boundary conditions. Referring to Figure 4.1, it is $f(\forall x, ny) = f(\forall x, 4)$, $f(\forall x, ny-1) = f(\forall x, 3)$, $f(\forall x, 2) = f(\forall x, ny-2)$, and $f(\forall x, 1) = f(\forall x, ny-3)$, where f is any function or its derivatives and "$\forall$" means any point on the axis. In x direction, we simply use fixed value or fixed slope conditions. That means $f(3, \forall y) =$ constant and $f(nx-2, \forall y) =$ constant, or $df/dx(3, \forall y) =$ constant and $df/dx(nx-2, \forall y) =$ constant corresponding to Figure 4.1. We manage the grid point values at x=1, 2, nx-1, and nx to make the fixed boundary condition. So our real calculation domain is from x=3 to x=nx-2, and from y=3 to y=ny-2, the area inside of the closed thicker bar in Figure 4.1.

Normally, we set blob's spatial characteristic scale length δ_x and δ_y ten times smaller than the size of simulation domain, L_x and L_y, therefore, boundary condition won't effect blob dynamics very much as long as the blob is not near the wall.

4.5 Accuracy and Resolution

Blob dynamics is very strong. One could expect instability, turbulent flow, and even chaotic situation in blob's evolution. However, we wouldn't like to see the chaotic situation happen too early. We are going to study the evolution process from regular coherent structure to turbulent regime. Besides using more stable numerical scheme such as RK4 to stabilize our model, we apply the following rules on data accuracy and numerical resolution, to some extent, to let our more stable, or in another word to lower down disturbance in our system.

4.5.1 Data Accuracy

As we know, in numerical simulation computer store data not with infinite precision but rather in some approximation that can be packed into a fixed number of bits (binary digits) or bytes (group of 8 bits). The system accuracy, sometimes called roundoff error, depends on the data type programmers choose for their code. Both Matlab and Fortran allow us a choice among different data types such as integer, single-precision, double-precision, etc. We choose double-precision (64 bits floating-point value), the higher level data accuracy, for all the data values in our simulation.

4.5.2 Numerical Resolution

There is another kind of error that is a characteristic of the program or algorithm used. It comes from the "discrete" approximations to the desired "continuous" quantity. This type of inaccurate representation would persist even on a hypothetical "perfect" computer that had an infinitely accuracy and no roundoff error. We know

that any kind of numerical inaccuracy could bring artificial disturbance to our system. To lower down this discretization-related inaccuracy, sometimes called truncation error, we try to use high enough resolution in our simulation. In practice, we run a code with nx×ny in resolution and then run another code with all the same parameters but two times higher resolution, 2nx×2ny than the preceding one. If the two runs are consistent with each other in terms of instability or graphical pattern, we will use the nx×ny resolution results as the final solutions. If apparent discrepancy occurs, we will try higher resolution code until we get consistent solutions from two different level of resolution. We believe higher resolution code gives us more reliable results in a strong dynamic system.

Chapter 5

SOL Blob Dynamics

5.1 Introduction

The main focus of this Chapter is on the numerical simulation of the dynamics of individual coherent structure, blob or dip, which is a concave in density background, in the SOL region in tokamak. The mechanisms of how blobs are peeled off from bulk plasma and penetrate into the SOL or how dips are formed are beyond the scope of this thesis work. Here we just seed such structures in uniform density SOL plasma and then follow their evolutions and capture geometrical features for different type of structures. We simulate different size circular blobs with and without Boussinesq approximation. Blobs with different scale length in radial and poloidal directions (oval blobs) are studied for distinguishing the influence of different spatial scale length on blob dynamics. In the third section, we introduce the concept of dip in the SOL and compare dynamics of blob and dip. We also discuss the diffusivity and inertia effect on blob dynamics in this Chapter.

5.2 Blob Simulation

Blobs, as we described previously, are extended structure along the field lines but with much smaller scales across the field line. They look like filaments and normally have cross-field size of the order of 1 cm. Through high speed camera in real experiment, we see blobs move radially or poloidally and end up with many different shapes. Some of them can coherently move in a very long distance. Some just fade away without clear trajactory. In this section, we explore blob dynamics by numerical simulation. The evolutions of different geometrical blob structures are discussed. The difference in motion due to poloidal scale length and radial scale length is presented. The effect of high background density to the blob motion and the full inertial term simulation are also discussed.

5.2.1 Circular Blob

Circular blob with poloidal scale length equal to radial scale length, i.e. $\delta_x = \delta_y = \delta$ [as defined in equation (4.11)], is the most simple coherent structure we can start from and this kind of shape is close to that observed in experiment, in which most coherent structures present comparable spatial scale in both poloidal and radial directions. Indeed, we are going to see this simple symmetric structure with single key parameter δ shows many essential properties of blob dynamics in the SOL. In the following, the dynamics of blobs with different scale lengths are discussed.

In this section, all circular blobs are initially set up in the same way described in equation (4.11). Figure 5.1 shows a general density contour plot of an initial blob (t=0) in the slab domain without scale. It could be seen as an initial plot of any circular blob

simulation at t=0. For example, if the domain length $L_x=L_y=L=10$, then it could be seen as the density contour plot for $\delta=1$ blob at t=0; if L=50, it is for $\delta=5$ blob at t=0. Therefore we won't show initial plot for circular blob at t=0 anymore. Here δ is the dimensionless scale length. The initial blob center is at $x_0=0.3L$ and $y_0=0.5L$, which is far enough away from boundaries to avoid any boundary effect. Density amplitude n_0 is 1 and background density n_{bg} is 0.01.
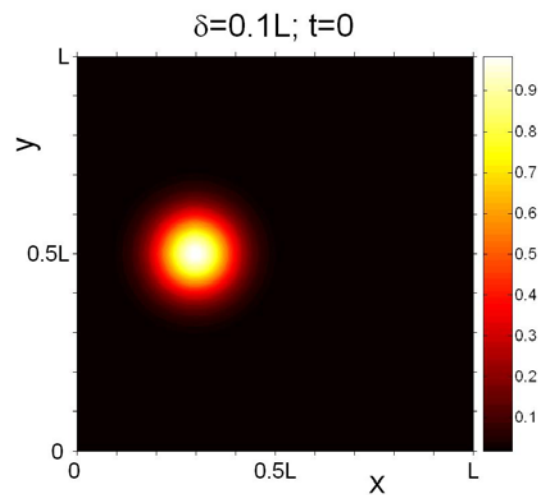

Figure 5.1 (Color) A general density contour plot of an initial blob at t=0 in the slab domain without scale.

Four group pictures of blob evolution are shown in Figure 5.2 to Figure 5.5, corresponding to $\delta=0.2$, 1, 2, and 5 respectively. Dimensionless diffusivities are given under the figures. We purposely choose the scale series with lengths smaller, equal and larger than unity because we want to see if the blob dynamics is going to change when the inertia effect goes from strong to weak as we have discussed in Chapter 3.

For δ=0.2 blob, the initial circular structure evolves into mushroom shape very quickly. Depending upon the qualitative analysis in Chapter 3, the inertia term is about 5^5 times larger than the other two terms. Although nonlinear effect could lower the degree of difference, the inertia effect is still strong. It shows up very quickly and becomes dominant. As a matter of fact, inertia term balances driving force term in the small-scale dynamics. Because this is a situation with fast changing dynamics, initial condition could somewhat affect the pattern of final results, such as the curvature of mushroom hat or the slope of leading/back edges. For example, Figure 5.6 shows the simulation result obtained with zero potential at t=0. From it we see that mushroom has smaller curvature and smoother back edge than the one in Figure 5.2 (b). The time range to get this stage is also longer because of different velocity levels associated with different scales of potential. However, these are just minor differences related to initial conditions. The mushroom shape, the major feature, always shows up in all our small-scale simulations.

For the δ=1 blob, as shown in Figure 5.4, the inertia effect is getting smaller. Basically the δ=1 blob propagates as a coherent circular structure to the right hand side with a long distance, which is much longer than the scale of itself. Again, we see slight mushroom pattern because the inertia term is still comparable to the other two terms when δ=1.

When we increase the blob size to δ=2 in Figure 5.5, the mushroom effect will never show up. This is because the inertia term becomes much smaller than the other two terms in this case. δ=2 blob coherently moves to the right in a very long distance.

Further simulation study shows that $\delta=2$ blob is not absolutely stable. It will involve in fingering effect after a long run. We also notice that, after long time evolution, a significant steepening of density profile starts to develop at the nose, as shown in Figure 5.6. This is due to the reduced E×B convection velocity in the x direction at the nose. As a matter of fact, for $\delta>1$ blob, the x component of the plasma convection, v_x, velocity can be estimated from $v_x \propto \partial\phi/\partial y \propto \partial^2 \ln n/\partial y^2$, which decrease when we move further from the center of the blob. This can explain the asymmetric profile (steep increase of the signal with further long relaxation tail) on the ion saturation current from the probe measurements (see, e.g., Refs. 19, 22 and 60). Similar effects were also reported in Refs. 37 and 39.

Continually increase the spatial scale of blob, we get to the $\delta=5$ blob in Figure 5.7. This regime is dominated by current dissipation because the inertia term is about 5^{-5} times smaller than the other two terms and can be surely neglected. What we see in the simulation is that this current dissipation controlled dynamics is not stable either. Instead of mushroom effect, the RT instability brought by the driving force, which is also the effective gravitational force, becomes dominant and the corresponding fingering effect appears later to break up the original coherent structure. The pattern of finger effect can change much. We have three-finger patter for the $\delta=5$ circular blob. We may also see two-finger, four-finger, or even more fingers pattern as shown later on. The key property in determining fingering effect modes is the blob scale, or more precisely, the poloidal scale of blob. We also notice that although the large scale blob

is subject to fingering effect, the scale of the gingers is comparable to the unity, or δ_*

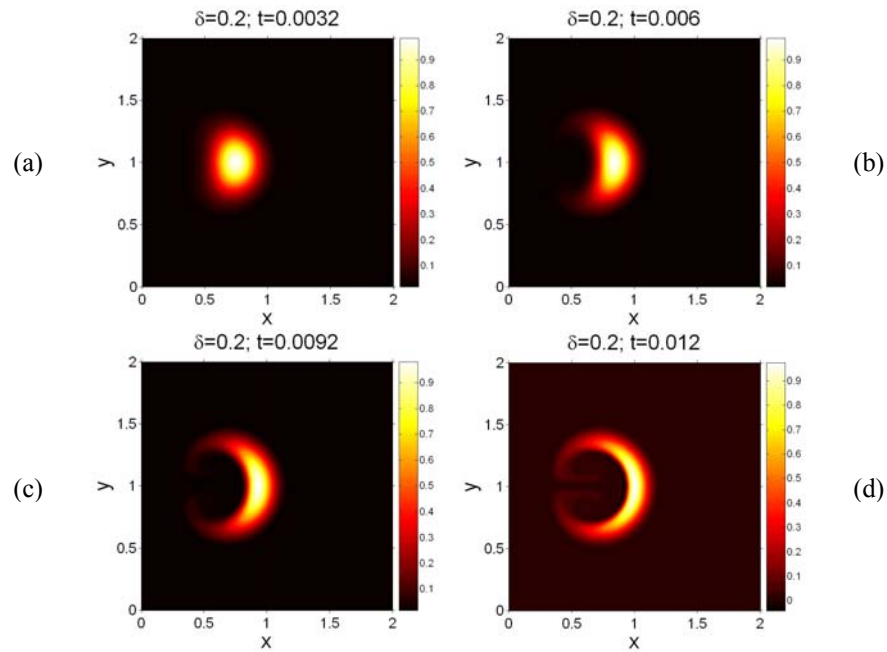in real units, and they keep propagating coherently to the right in large distance.

(a) (b)

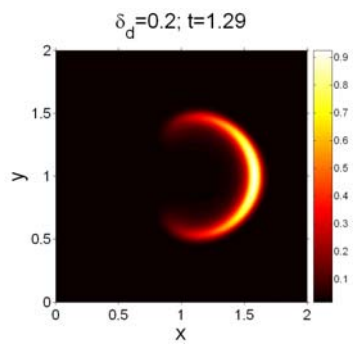(c) (d)

Figure 5.2 (Color) SOL blob evolution with δ=0.2 and D=0.002.

Figure 5.3 (Color) SOL blob zero-initial evolution with δ=0.2 and D=0.002.

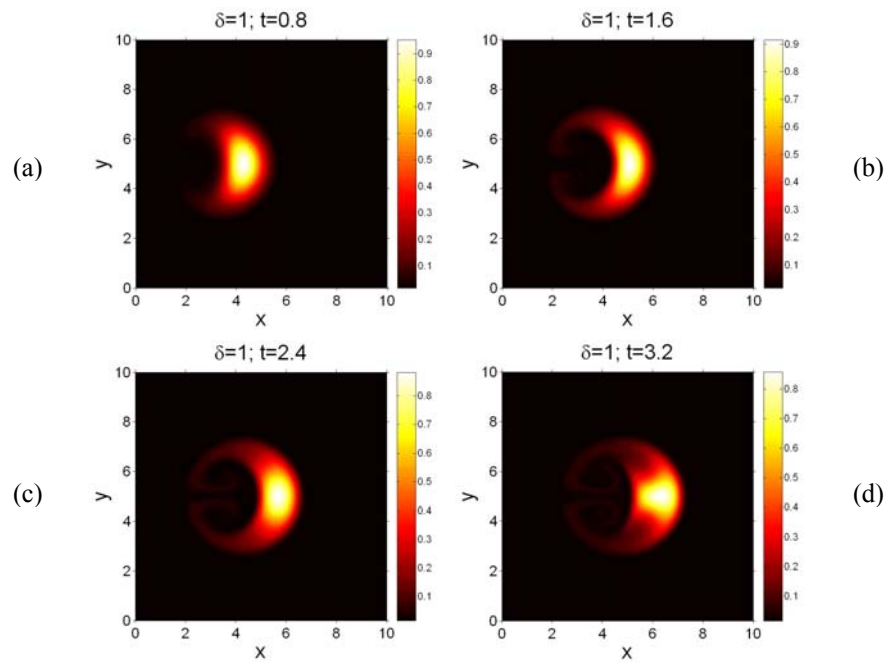Figure 5.4 (Color) SOL blob evolution with δ=1 and D=0.005.
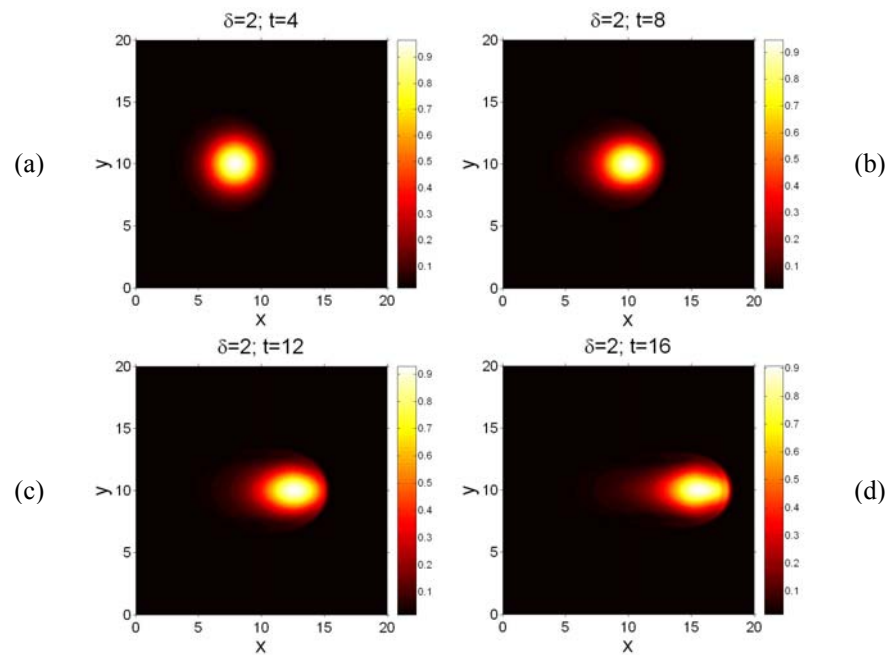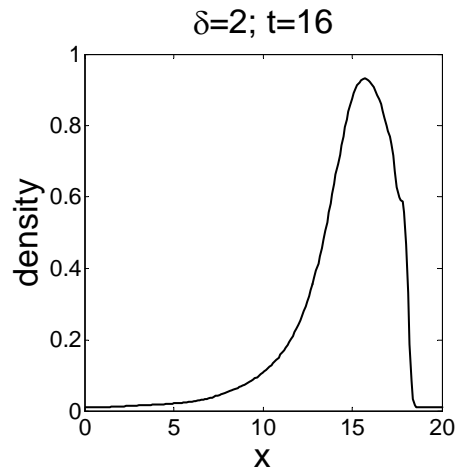

Figure 5.5 (Color) SOL blob evolution with δ=2 and D=0.005.
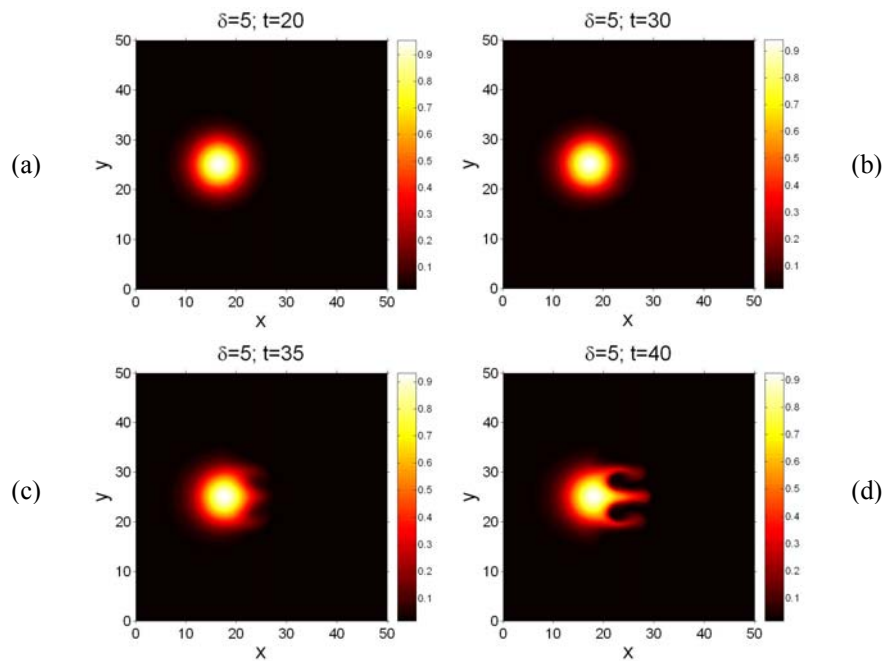
Figure 5.6 δ=2 blob's central profile with relaxation tail.

Figure 5.7 (Color) SOL blob evolution with δ=5 and D=0.01.

5.2.2 FI-SOL Blob Simulation

In most current edge plasma numerical simulations, reduced inertia (RI) technique is used in modifying governing equation as we did in our studies [40]. This simplified model has shown many essentials of blob dynamics. However, we still want to know how big difference between the full model and the reduced one. We use the technique described in Chapter 4 to solve the FI-SOL model numerically.

Figure 5.13 to Figure 5.16 show four different scale length blobs in FI-SOL model. We clearly see that, in FI model, smaller blobs are more structurally stable and coherently propagate in a longer distance than in RI model. However, larger blob like $\delta=2$ is less stable than its counterpart. Comparing with RI-SOL results at same time stage, $\delta=0.2$ and $\delta=1$ FI blob motions have mushroom shapes suppressed. We don't clearly see mushroom shape in 1 blob motion. Also we see the difference of velocity for $\delta=0.2$ and $\delta=1$ blob in Figure 5.13 and Figure 5.14 Small FI blob keeps the constant velocity better than small RI blob because RI blob's speed is slowed down by stronger mushroom effect. This is coincident with the mushroom suppression when we take the density variation in inertia term into account. $\delta=2$ blob is the most stable one in RI simulation but it goes to fingering effect here, which probably due to mushroom suppression. Meanwhile, without surprise, the $\delta=5$ blob motion doesn't change much between FI and RI results. It is because the inertia term is negligibly small in this large size case. Neglecting part of inertia term won't change the whole story very much.

Over all, FI-SOL model in general is coincident with RI-SOL model. However, some details differ. In particular the most stable scale length shifts from 2 to 1.

The iterative relaxation method used in FI-SOL model is very restricted with parameters like diffusivity and iteration times to have the simulation converged. It also cost much more CPU-time and system memory in calculation than RI-SOL model. Depending upon the results we have by far, we think the RI-SOL model is a reasonable approximation and good enough in studying vorticity equation.

5.2.3 Oval Blob

In previous section, we study circular blobs with different size. In this section, we demonstrate results of simulation of oval blobs ($\delta_x \neq \delta_y$). The effect of δ_x and δ_y on blob dynamics are not the same. Based upon our analytical analysis of instability criterion, equation (3.51), and the expression for the drift velocity, equation (2.13), one should expect that the scales of δ_x and δ_y are not equivalent in terms of the blob dynamics. Poloidal scale length δ_y should be the key factor in determining the radial velocity of blob and intriguing the fingering instabilities. Radial scale δ_x is less important for radial motion.

Figure 5.13 shows a radially elongated blob with $\delta_x=5$ and $\delta_y=2$. Comparing with the circular blob simulation results in the preceding section, one can see this oval blob motion is more likely to be comparable to the $\delta=2$ blob motion. It moves outward about 10 dimensionless unit long and then evolves into fingering effect and ends up being two fingers.

Figure 5.14 shows a poloidally elongated blob with $\delta_x=2$ and $\delta_y=5$. Although the initial configuration of blob is almost the same as the upper one with just 90 degrees turning around, the blob dynamics is very different. The poloidally elongated blob moves more like the dynamics of $\delta=5$ blob because it doesn't move forward much and tends to fingering effect after a while. The breaking up point comes earlier in this oval structure comparing with the circular counterpart and it breaks into parts (four fingers) at the end.

Here we are going to discuss the relation between the blob speed and its scale. As we showed in Chapter 2, for blob with poloidal scale close to or larger than one, blob speed should be determined by the poloidal scale and the relation is $v_b \propto \delta_y^2$. In Figure 5.15, we define the blob position by its highest density point and plot blob position vs. running time. The slope will show blob speed. It is clear that coherent structures with same poloidal scales have same speed. From another point of view, Figure 5.16 shows that $v_b \cdot \delta_y^2$ tends to be a constant. We also read that this speed-scale relation will be weakened by non-linear vorticity term as blob getting smaller.
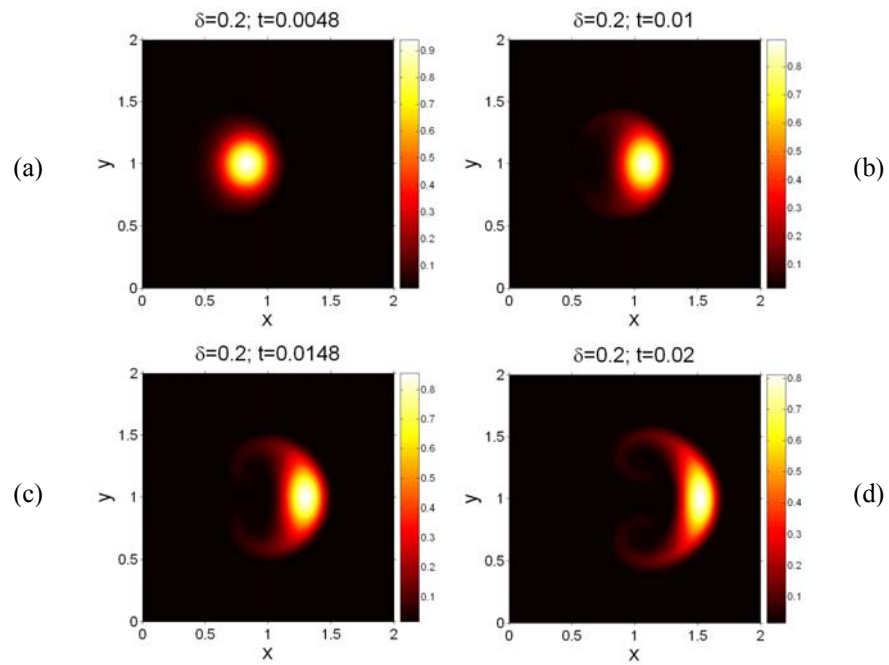
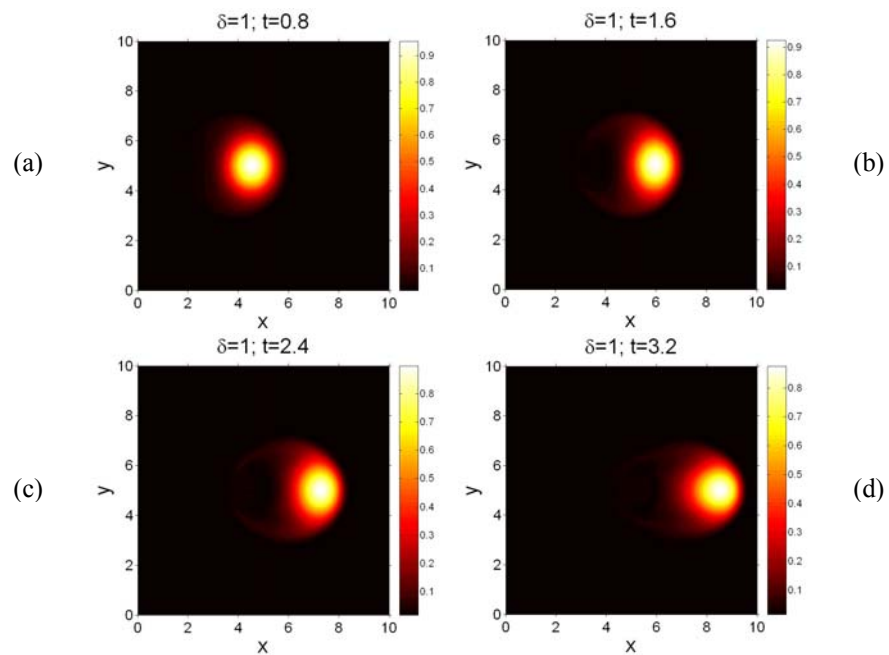Figure 5.8 (Color) FI-SOL blob evolution with δ=0.2 and D=0.01.

Figure 5.9 (Color) FI-SOL blob evolution with δ=1 and D=0.01.

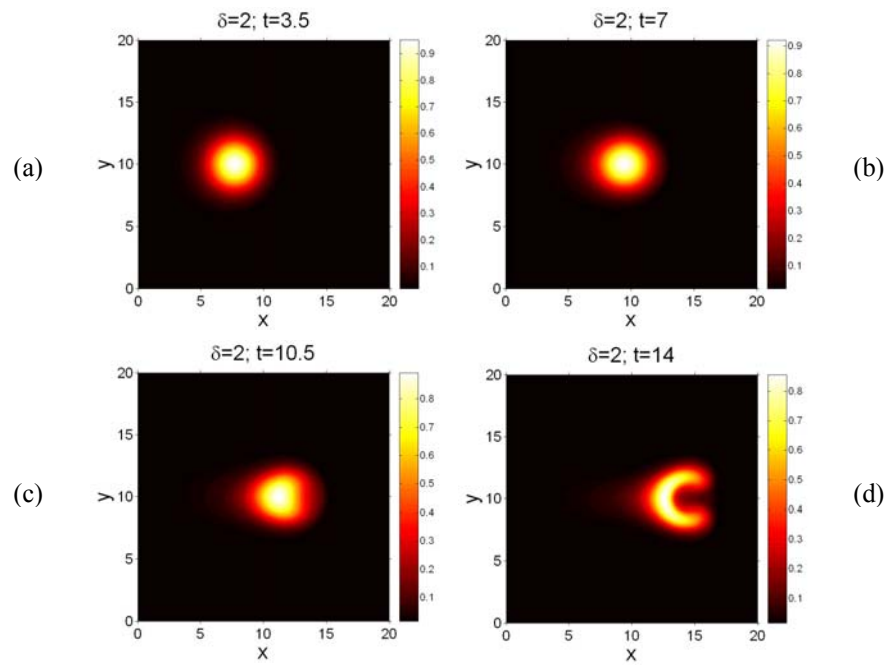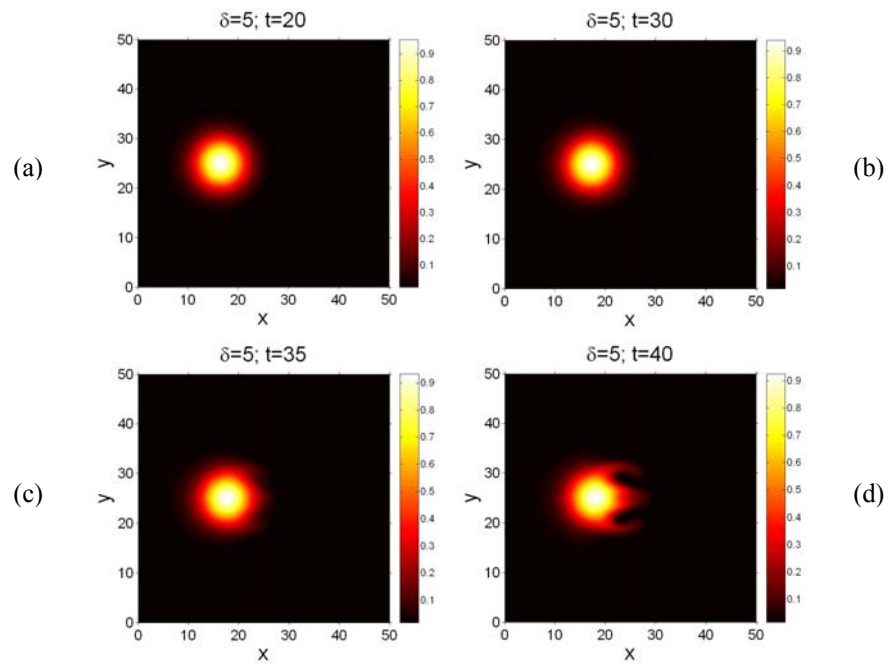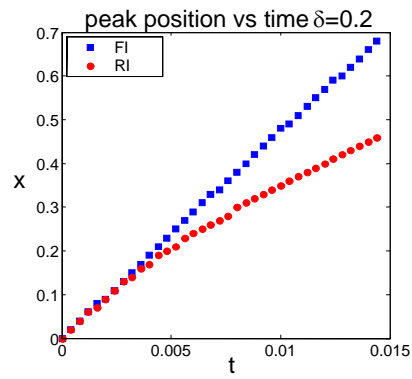Figure 5.10 (Color) FI-SOL blob evolution with δ=2 and D=0.01.

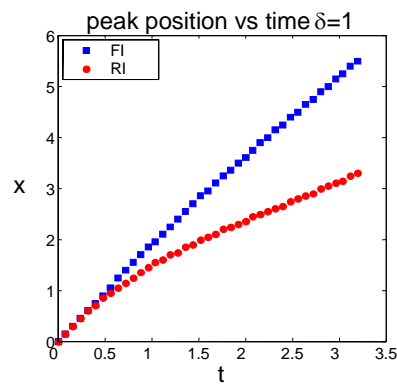Figure 5.11 (Color) FI-SOL blob evolution with δ=5 and D=0.01.

(a)

(b)

Figure 5.12 (Color) Blob's peak position vs. time in FI-SOL model with square dot line and RI-SOL model with circle dot line. Small FI-blob keeps the constant velocity better than small RI blob because RI blob's speed is slowed down by strong velocity shear, i.e. mushroom effect. This is coincident with the mushroom suppression in FI results.
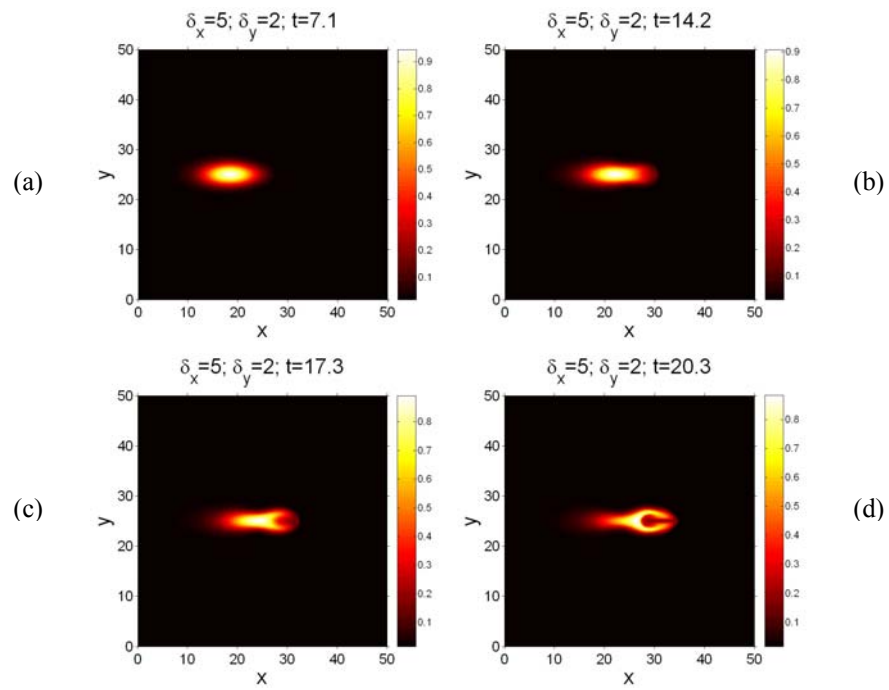
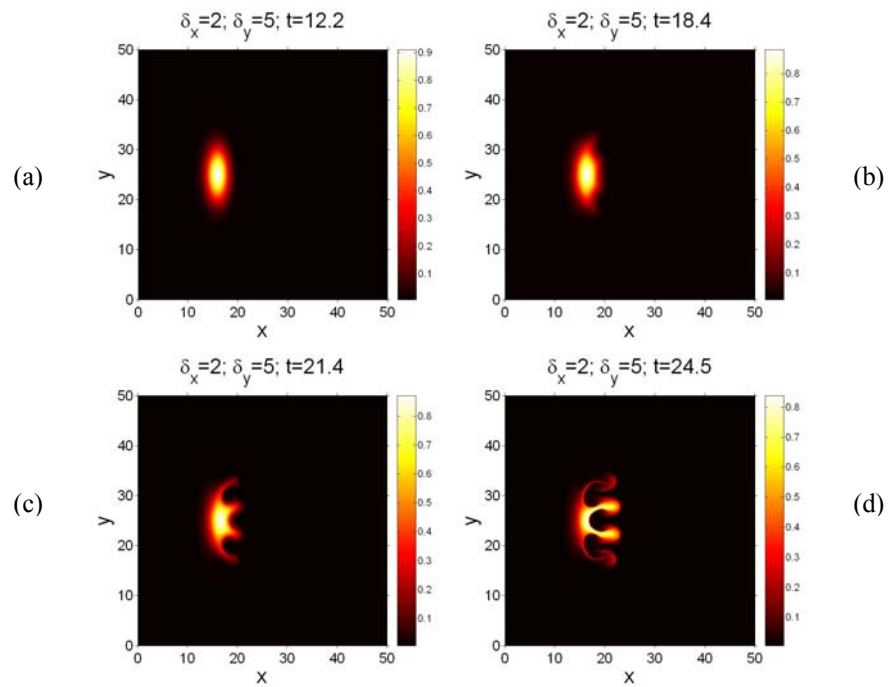Figure 5.13 (Color) Oval blob evolution with $\delta_x=5$, $\delta_y=2$ and D=0.01.

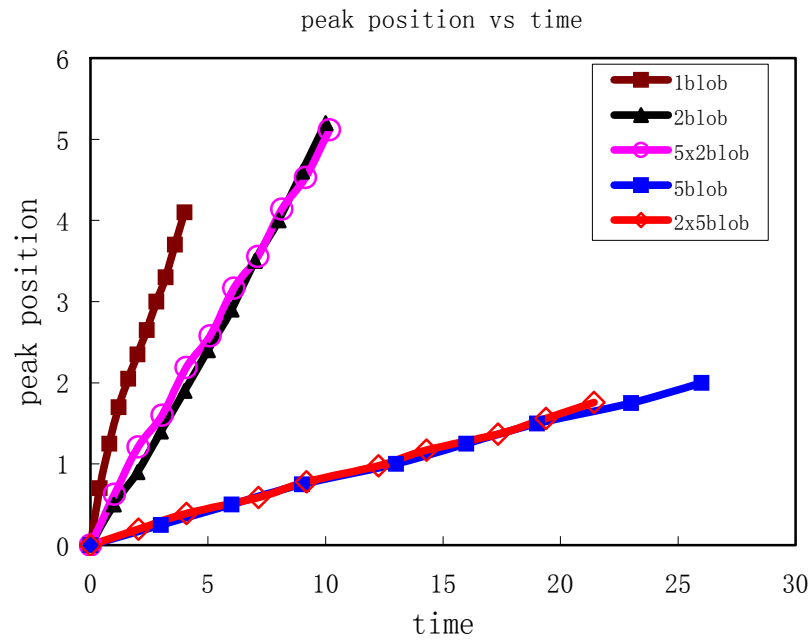Figure 5.14 Oval blob evolution with $\delta_x=2$, $\delta_y=5$ and D=0.01.

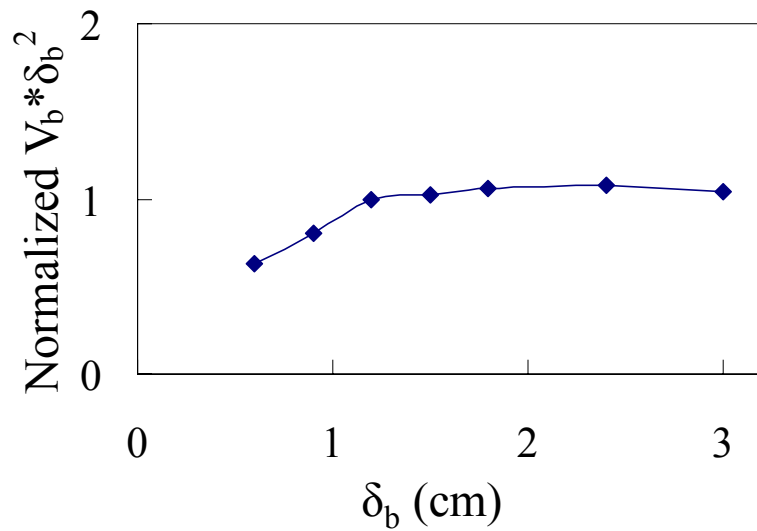Figure 5.15 (Color) Blob peak position vs. evolution time.

Figure 5.16 Relation between blob speed and blob scale.

5.2.4 Impact of Background Density

So far we assume the density magnitude within blob, n_0, is a hundred times larger than background density n_{bg}. Different ratio of n_0/n_{bg} can change the dynamical pattern of blob motion.

The impact of the ratio n_0/n_{bg} on the spatio-temporal evolution of the blobs is demonstrated in this section by Figure 5.17 and Figure 5.18. Both have smaller ratio n_0/n_{bg} as 5 and 2 respectively. δ is equal to 5 in both cases. In the high background situation, the $v_x(y)$ profile, which can be estimated from $v_x \propto \partial_y^2 \ln(n)$, significantly changes in comparison to the results for $n_0/n_{bg} = 100$ in Figure 5.7. As a result, high background effectively narrows down poloidal section of the blob. This effectively decreases the magnitude of δ_y. So in Figure 5.7 we see the $\delta=5$ blob breaks into three fingers, but in Figure 5.17 there are only two major fingers. In Figure 5.18, there is only one major finger. This means the effective scale decrease to value less than 5. It can be seen as the major density in center blob coherently moves forward and transport material to a large distance. We also notice that smaller density difference between center blob and background slows down the dynamics. Finger effect delays because driven force associated with density gradient is weaker in high background case.
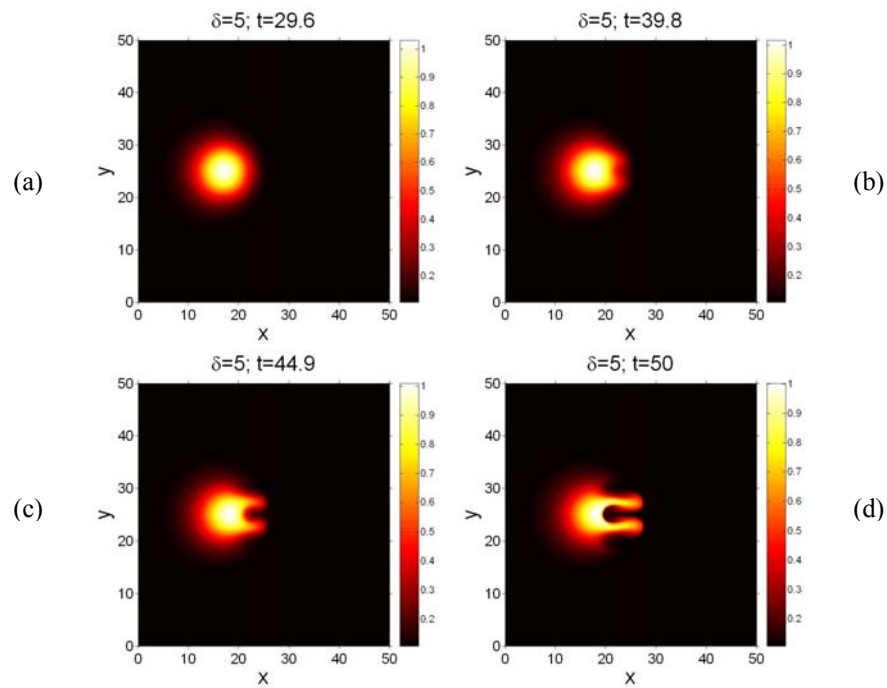
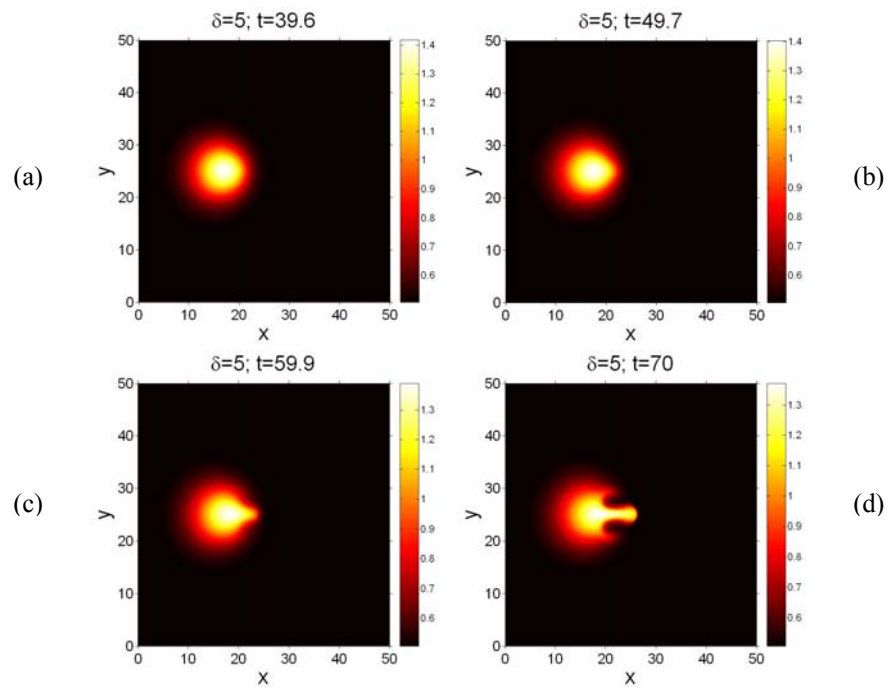Figure 5.17 (Color) High background blob evolution with δ=5, n_0/n_{bg}=5, and D=0.01.

Figure 5.18 (Color) High background blob evolution with δ=5, n_0/n_{bg}=2, and D=0.01.

5.3 Dips

Blobs rapidly transfer plasma outward, increasing sputtering of wall material. Also, return convective flows may rapidly carry impurities across the SOL and into the core plasma. Next we study the evolution of the dips of plasma density in the SOL plasmas. While the ∇B+curvature polarization of blobs causes their ballistic motion to the outer side of torus, the polarization of dips will cause dip to move toward the core. uch features of dip motion are observed in our 2D modeling [111] and have been seen experimentally near the separatrix [19, 112], where dip diagnostic is easier. Ballistic motion of dips can explain the penetration of impurity from the wall to the core often seen in experiments. Indeed, neutral impurity atoms/molecules, being sputtered from the wall, fly to the plasma and, finally, are ionized at some distance from the wall. Neutral impurities that are ionized within the blobs will be immediately carried away to the wall by the blob motion and will not contribute to core plasma contamination. But impurities that are ionized within the dips can be convectively carried towards the core.

Evolution of density contours for dips with $n_d/n_{bg} = 0.5$ and and $\delta = 1$ are shown in Figure 5.17 and Figure 5.18. The initial dip density distribution $n_d(t=0)$ as the following is slightly different from blob density n_b in equaiton (4.11).

$$n_d(x, y, t = 0) = n_{bg} - \exp\left[-\left(\frac{x - x_0}{\delta_x}\right)^2 - \left(\frac{y - y_0}{\delta_y}\right)^2\right]$$

(5.1)

Similarly n_{bg} is the normalized background density and δ_x and δ_y stand for characteristic scale length of dip in x and y directions. Unlike the blob, the dip is occupied by plasma with lower density than ambient plasma.

An apparent observation is that dip motion is contrary to blob motion in direction. The dynamics of an individual dip can significantly differ from that of a blob. The reason is the difference in the magnitudes between the blob and dip plasma density excursions from the background. The magnitude of the blob density, n_b, is not restricted and can be much larger than background plasma density n_{bg}. The magnitude of the dip density, n_d, is restricted. Then, recalling expression (2b), we conclude that the impact of the velocity shear and, therefore, vorticity effects, on dip dynamics may be rather strong. We see this from Figure 5.19 and Figure 5.20 that indeed vorticity effects play a very important role in dip dynamics. Vorticity slows down the inward dip propagation and even breaks the dips into pieces. We also found fast-moving mushroom structures, which is similar to those found in the case of small-scale blob evolution, propagate radially from wall side (RHS) to core side (LHS).

Figure 5.19 (Color) Dip motion with $\delta_d=1$, $n_d/n_{bg}=0.5$, and D=0.01.

Figure 5.20 (Color) Dip motion with $\delta_d=1.3$, $n_d/n_{bg}=0.5$, and D=0.01.
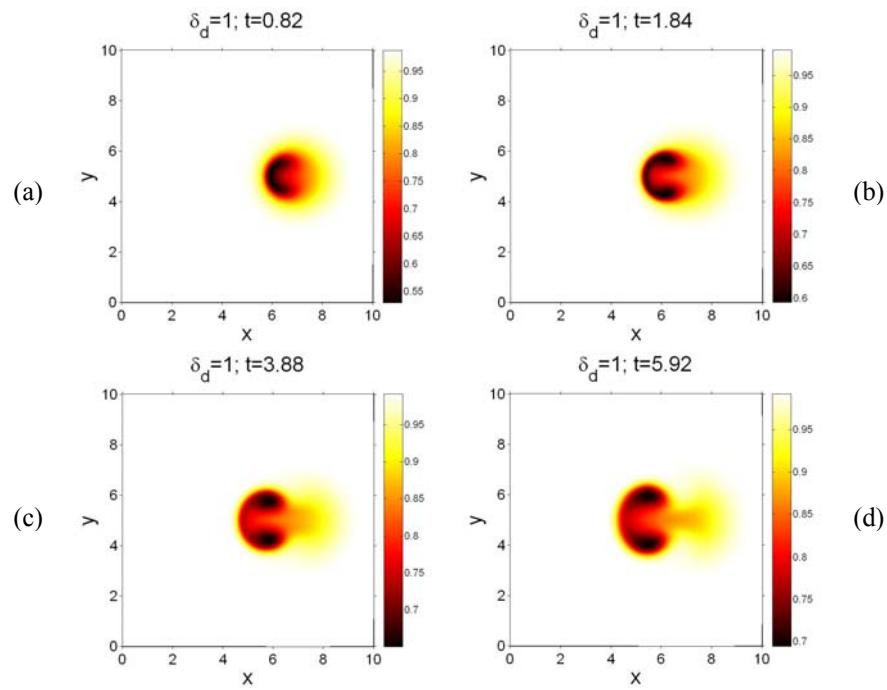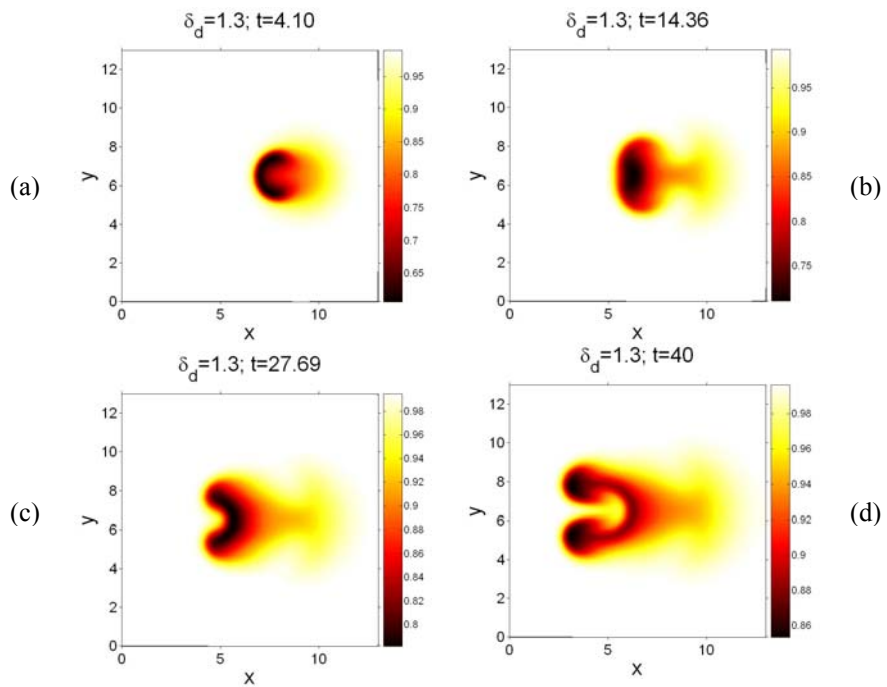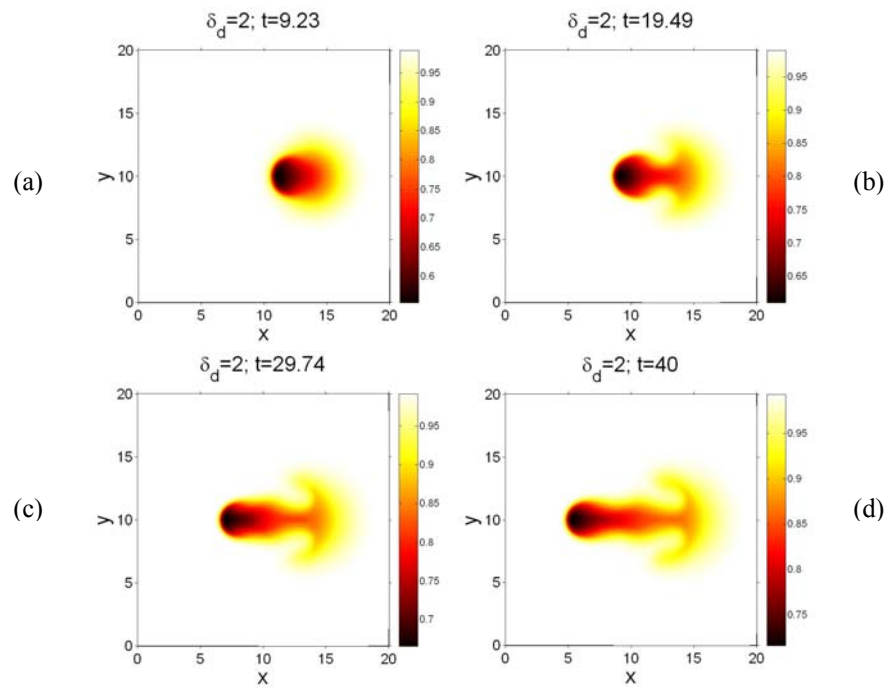
Figure 5.21 (Color) Dip motion with $\delta_d=2$, $n_d/n_{bg}=0.5$, and D=0.01.
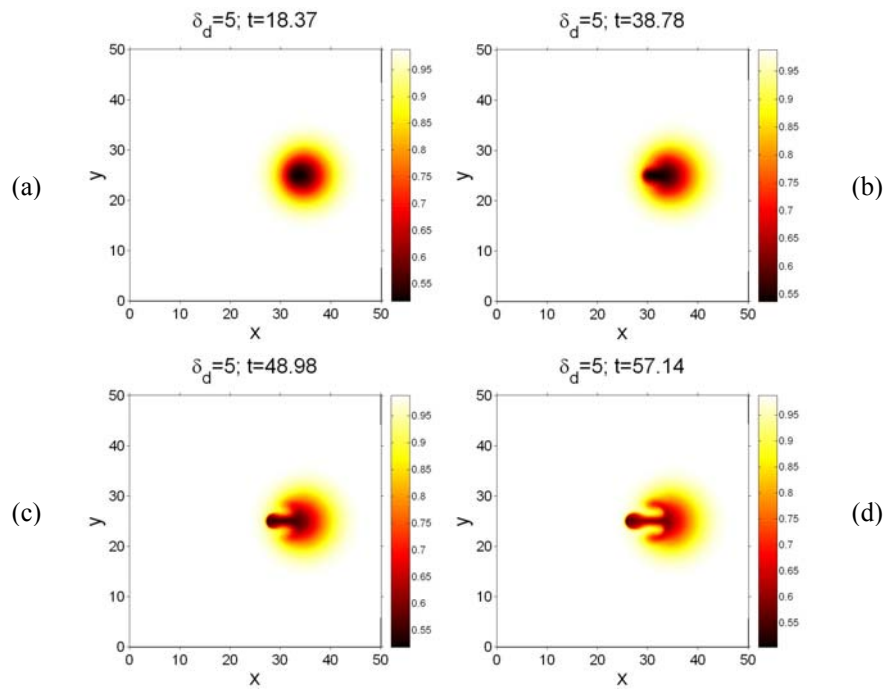
Figure 5.22 (Color) Dip motion with $\delta_d=5$, $n_d/n_{bg}=0.5$, and D=0.01.

5.4 Discussion of Inertia Term

As we discussed previously, D'Ippolito and Myra independently study blob dynamics using their numerical model without inertia term. In their numerical results reported, we can see the RT instability almost everywhere. However, in their results there is no mushroom effect appeared. It turns out that the mushroom effect and vortex dipole are associated with the inertia term.

Figure 5.23 shows blob evolution with inertia term and driving force dominated, i.e. the current term in vorticity equation is neglected in this group of simulation. Comparing with results in section 5.2.1, we see that $\delta = 0.2$ blob has little change, but $\delta = 2$ and 5 blobs change a lot. As we know, for small blob like $\delta = 0.2$, by linear stability analysis, the inertia term is much larger than current term. Therefore, neglecting current term in vorticity equation has almost no influence on blob evolution. For $\delta = 2$ and 5, inertia term is parallel or much smaller than current term. Neglecting current term of course strongly change the dynamic system. As a result, we don't have coherent moving structure and finger shape in Figure 5.23. Instead we have all size of blobs end up with mushroom patterns with a vortex dipole behind. It is clear that inertia term drives the structure to mushroom shape and builds up vortex inside the structure. Related study can be found in Ref. [38].
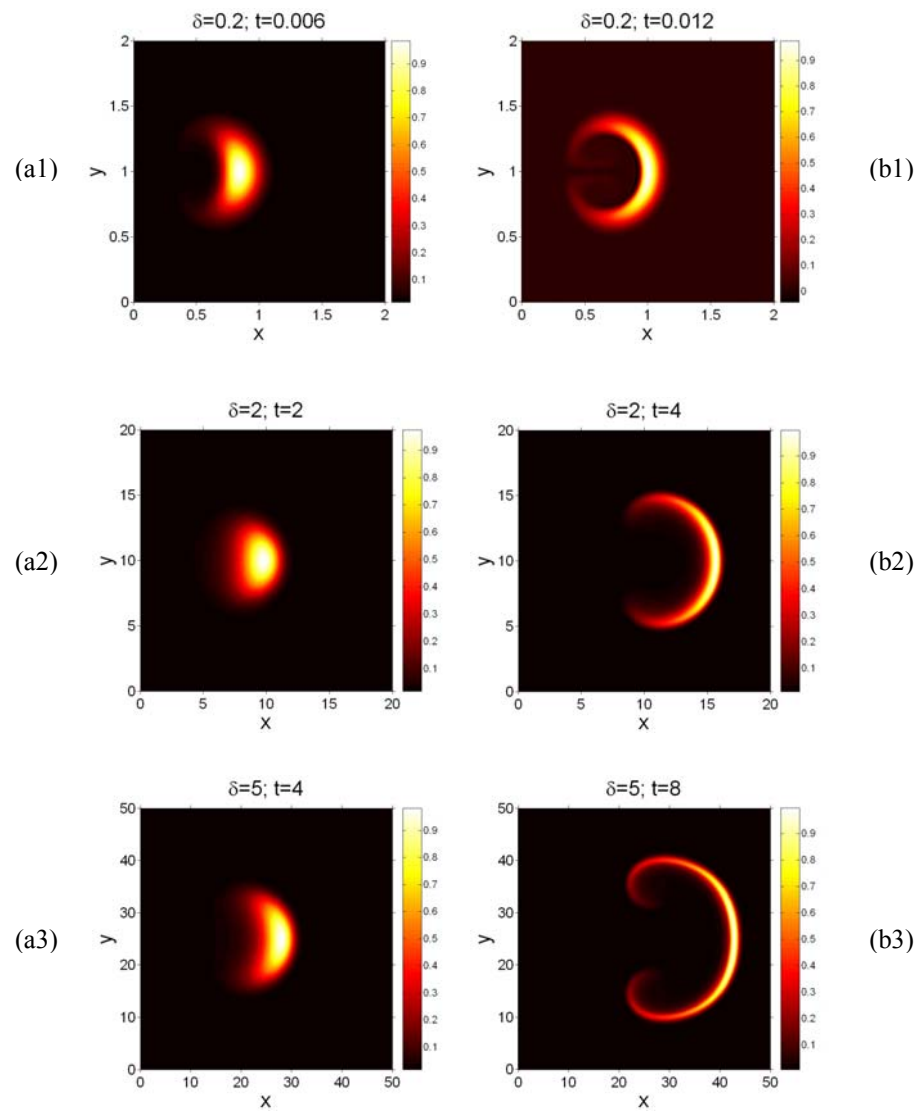
Figure 5.23 (Color) Blob evolution with inertia term and driving force dominated.

5.5 Conclusion

In this Chapter we have carried out simulations of the SOL blob dynamics on circular blobs, oval blobs, and dips. We also study the effect of density background, diffusivity, and inertia term on blob dynamics.

We have found that all blob moves outward by E×B drift. The most structurally stable blob has dimensionless scale length around one, which is corresponding to the characteristic scale length δ_* derived in Chapter 3, and propagate coherently to large distances. Steep nose profile can explain experimental asymmetric profile. Blobs smaller than one evolve into rather slowly moving mushroom-like structures due to strong velocity shear. Blobs larger than one are subject to the fingering instability, which very quickly chops large blobs into a number of relatively narrow fingers reducing their effective cross-field scales. Blobs with spatial scales close to one can coherently move to long distances. The SOL Blob velocity is numerically proved to be proportional to $1/\delta^2$, which is in agreement with our previous scaling analysis.

Also we have found that scale lengths δ_x and δ_y are not equivalent. δ_y determines motion mode and velocity. High background plasma density effectively narrows down blob size.

In the model without the Boussinesq approximation (the FI-SOL model), dynamics is somewhat suppressed. Big blob motion, such as $\delta=5$ blob, doesn't change much comparing with results from the RI-SOL model. For $\delta=0.2$ blob, mushroom

effect is greatly suppressed. In δ=1 blob simulation, inertia effect is not perceptible. Meanwhile, relaxation tail gets longer in the FI case. Over all, FI-SOL model in general is coincident with RI-SOL model. However, some details differ. In particular the most stable scale length shifts from 2 to 1.

Density dips move inward to the core plasma, opposite to the blob movement. Impurity can be carried into the core by dip motion. Vorticity effects in dip is strong, slows down propagation speed and breaks one dip into pieces.

The inertia term in vorticity equation drives the structure to mushroom shape and builds up vortex dipole within the structure. Blob goes to mushroom shape when neglecting parallel current term regardless of the scale length. Blob goes to fingering effect without inertia term regardless of the scale length.

The text of Chapter 5 is, in part, a reprint of the material as it appears in "Two dimensional modelling of blob dynamics in tokamak edge plasmas," G. Q. Yu, S. I. Krasheninnikov, and P. N. Guzdar published in Physics of Plasmas 13, 042508-1 (2006). The dissertation author was the primary author in this paper.

Chapter 6

High β Blob Dynamics

6.1 Introduction

In this Chapter, we present our numerical solutions on HB blob. The normalized governing equations, equation (3.45) and (3.46), have been discussed in Chapter 3. Features of this type of blob has been given in the discussion associated with closure (3.34) in Chapter 3. Spatial geometry is also given in Figure 3.2. To simplify our job, we take Boussinesq approximation in our HB model. So the exact vorticity equation we are solving numerically is the equation (4.2).

6.2 HB Blob Simulation

Numerical simulation results are shown in Figure 6.1 to Figure 6.4. It is clear that HB blobs also move forward to low B side by the E×B drift. However, we notice that the motion modes or the patterns of these HB blobs are somewhat different from the SOL blobs we have studied so far. Looking at Figure 6.2 to 6.4, where blobs have same scale lengths as in Figure 5.2, 5.4, and 5.7, we don't see mushroom shape or fingering shape in the blob evolution. The blob dynamics doesn't obviously change

when the blob scale increases from $\delta=0.2$ to $\delta=5$ right crossing the interesting scale length of unity, which is unlike the previous Chapter results. This is in agreement with what we analyse in Chapter 3. In HB case, the inertia effect would change slightly because the ratio between inertia term and the other two terms is only δ^{-1}. So we won't see great difference in the motion mode when δ is just 5 times smaller/larger than one. However, for some extremely small blob, such as the 0.01 blob shown in Figure 6.1, the inertia term becomes dominant because the ratio $\delta^{-1}=100$ in this case. The mushroom effect and the vortex dipole show up. Note that these results are very similar to pellet cloud study [97, 98]. We also observe fingering effect in HB model for large blob with sufficiently steep leading edge. One can find out rather similar results in [100].

Another interesting feature of the HB blob is the long relaxation tail following behind the leading density peak. We see this steeply increasing density front with long lasting tail for all blobs close to unity in Figure 6.2 to 6.4. One of the density midline in Figure 6.4 (d) is extracted out and shown in Figure 6.5. This type of bursting signal followed by a smoother decaying tail has been extracted from measurement of ion saturation current in SOL region [19, 60]. So experimental coherent structure in SOL with long relaxation tail could also be formed close to or inside of LCFS and be dragged out to SOL region by the blob dynamics shown here. It has been shown that SOL blob can also form a relaxation tail in the previous Chapter. We notice that SOL blob's tail, comparing with blob itself, is much shorter than the HB blob's tail shown inhere.

As we knew, velocity of SOL blob is proportional to δ^{-2}, however, HB blob velocity is independent of blob scale, which is just follows our scaling analysis in Chapter 3. Numerical resutls are shown in Figure 6.6. We plot the x positions of density peaks of blobs vs. time, which demonstrates blob velocity by the slope. To make it more comparable and readable, we use δ for each blob to rescale its own x and time axes. Note that this rescaling is only for resizing the figure and containing all four blobs' position-time figure suitably in one frame just like a zoom-in/out process. It does not change the slope of the curves at all. In Fig. 8, initially, all blobs move to RHS. The moving distance is much longer than the blob size itself and the velocity is a constant. Then the 5 blob and 1 blob will keep moving with constant velocities, which implies, in tokamak close to LCFS region, larger blob around dimensionless one or bigger could move coherently in a longer distance with constant velocity. They may transfer into SOL region and form blob structures with long lasting tails in there. Smaller blobs like 0.2 and 0.01 blob will slow down. The smaller the blob structure, the faster the velocity decreasing. This velocity decreasing process is associated with the inertia term effect.
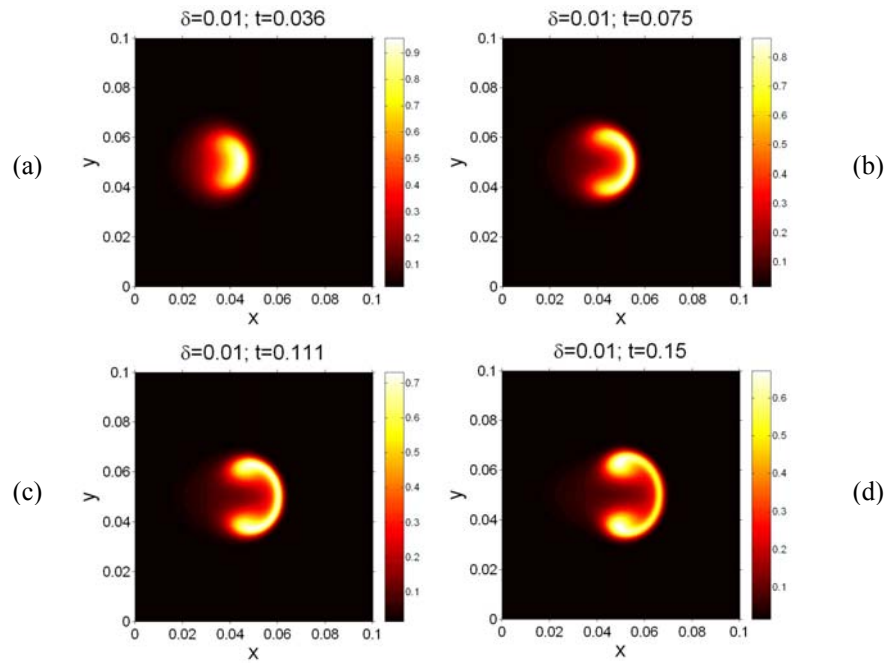
Figure 6.1 (Color) High β blob evolution with δ=0.01 and D=0.00002.
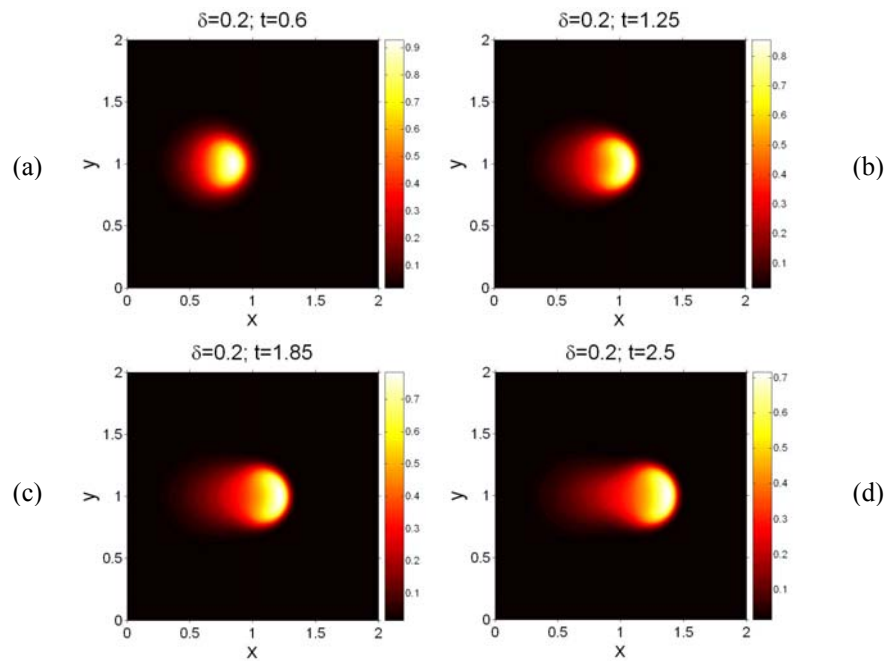
Figure 6.2 (Color) High β blob evolution with δ=0.2 and D=0.001.
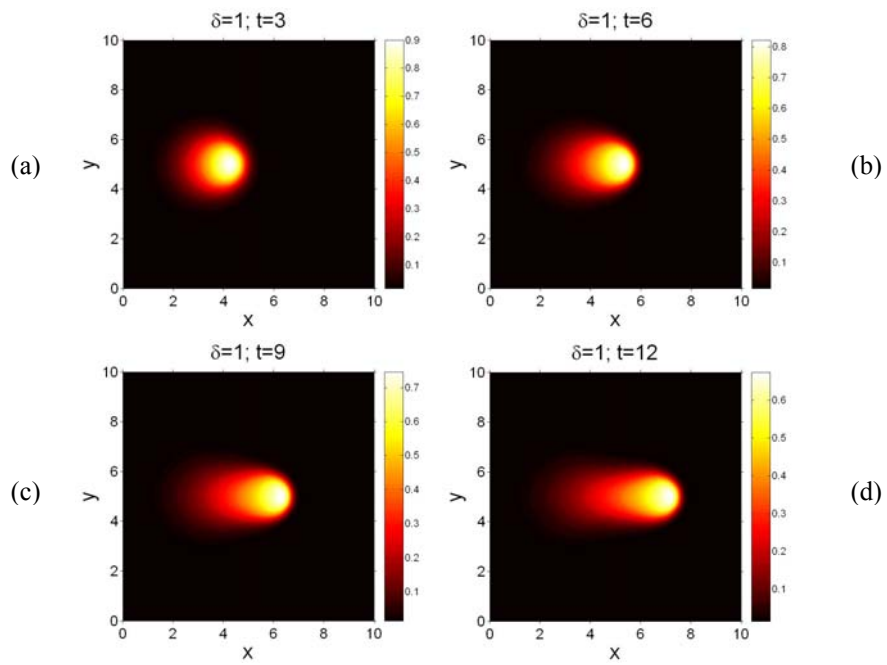
Figure 6.3 (Color) High β blob evolution with δ=1 and D=0.008.
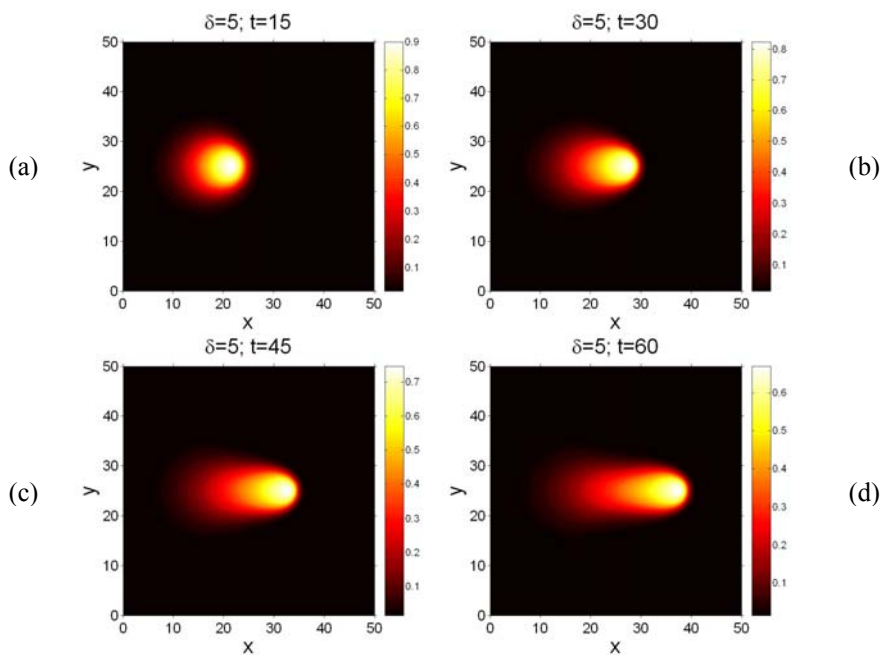
Figure 6.4 (Color) High β blob evolution with δ=5 and D=0.04.
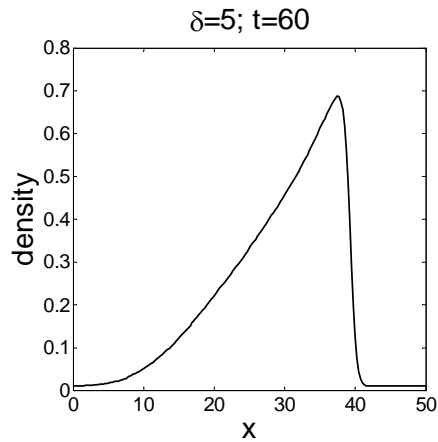
Figure 6.5 δ=5 High β blob's midline profile with relaxation tail.
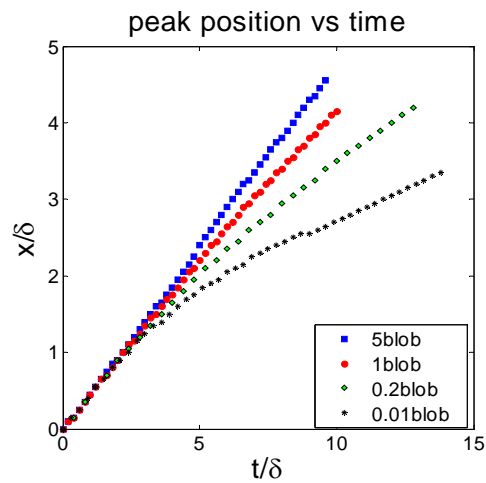
Figure 6.6 (Color) Peak position vs. time of HB blob in different sizes. We use δ for each blob to rescale its own x and time axes. This rescaling is only for resizing the figure and containing all four blobs' position-time figure suitably in one figure. It does not change the curve's slope, which stands for the velocity of the blob.

6.3 Impact of Plasma Diffusion

As we showed in section 5.2.1, radial blob behaviour is like shock-wave solutions of the Burgers' equation, where steep leading edge due to nonlinear convection is balanced by diffusion. Therefore, in addition to the spatial scale of the blob, relative dissipation level in the system is expected to play an important role in blob dynamics as well.

As we understand, the diffusive dissipation with large enough value can always kill the dynamics or instability. In practice, we set diffusivity D as a very small dimensionless number which can help in numerical stabilization but not kill the interesting dynamical features. Numerically $D < 0.1 \times \delta^2 / t_{max}$, where t_{max} is the longest simulation time. For example, in a $t_{max}=10$ simulation for $\delta=1$ blob, we set $D < 0.01$. This would more or less guarantee that blob won't deform too much just by diffusion (see Ref. [39] for details). In Figure 6.7, we show two group of simulation results for blob's evolution with different diffusivities, (a) for the $\delta=2$ SOL blob, (b) for the $\delta=1$ HB blob. The diffusivity doesn't change the blob motion modes much in both (a) and (b) cases. As one can expect, the peak density is diffused lower in higher diffusivity case. In (b), the "shock front" is more apparently smoothened by higher diffusion and the blob speed slows down a little bit more. Note that, in real units, D = 0.01 is corresponding to 0.67m²/s for real diffusivity in the SOL case, and 1.45 m²/s in the HB case. Our applied diffusivities are mostly in the range of 0.1~1m²/s. These

plots also show that, when close to unity, the HB blob extends a longer tail than the

SOL blob does.

(a)

(b)
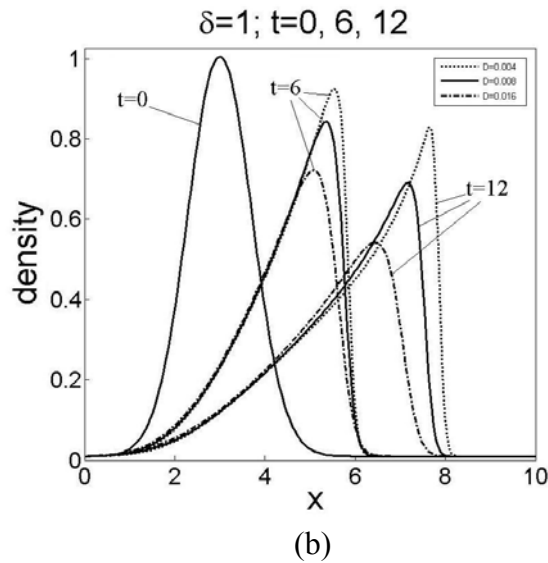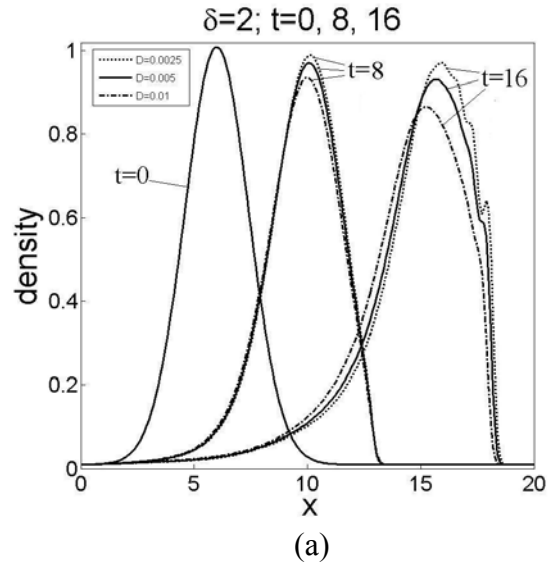
Figure 6.7 Density profile at center line of blob with different diffusivities. In (a), δ=2 SOL model, dot line is for dimensionless D=0.0025, solid line is for D=0.005, dot-dash line is for D=0.01. In (b), δ=1 HB model, dot line is for D=0.004, solid line is for D=0.008, dot-dash line is for D=0.016. Diffusivity doesn't change the blob motion modes much in both cases.
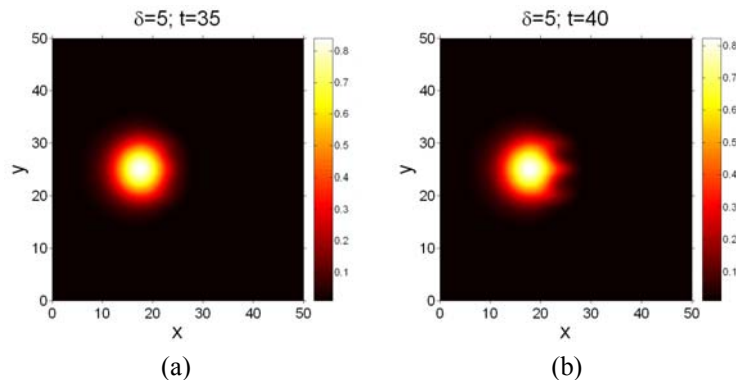
Figure 6.8 (Color) SOL blob evolution with δ=5 and D=0.03.
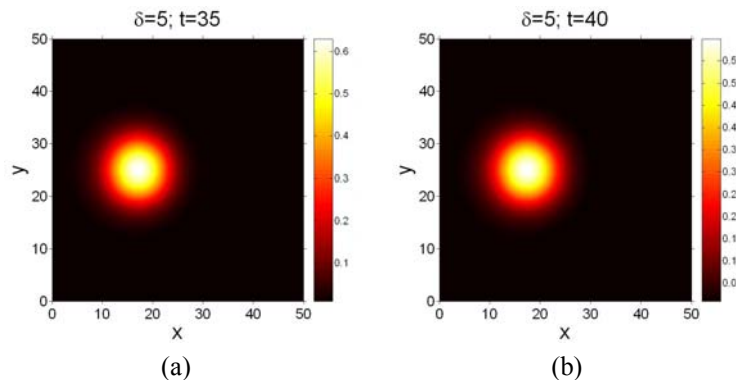
Figure 6.9 (Color) SOL blob evolution with δ=5 and D=0.1.

Meanwhile, we can also see the stabilization effect by stronger diffusion from density contour plots in Figure 6.8 and Figure 6.9, where δ = 5 simulation is made for D = 0.03 and 0.1. Comparing with solutions in Figure 5.7 (c) and (d), one can easily see that the RT instability is stabilized by stronger diffusion. As D = 0.01, the fingering effect is fully developed at t = 40. However, as D = 0.03, although we still see fingering effect at t = 40, it is much weaker than the D=0.01 case. As D up to 0.1, the fingering effect is fully suppressed at t=40 by the relatively large diffusivity.

6.4 Conclusion

In this Chapter we have carried out simulations of the HB blob dynamics. We apply our code on blobs with normalized scale length of 0.01, 0.2, 1, and 5. We have found that HB blobs coherently move forward. They have larger stable range in terms of scale length. They also have longer relaxation tale. We observe mushroom effect for extremely small blob, and fingering effect for big blobs with steeper boundary. HB blob moves with a constant velocity about one half in normalized unit. Unlike the SOL blob the drift velocity does not depend on blob size δ. Blob's velocity slows down more quickly as the scale length getting smaller.

The plasma diffusion doesn't change the blob motion modes much. But it has stabilization effect on blob dynamics. It is shown that RT instability is suppressed by large diffusivity.

The text of Chapter 6 is, in full, a reprint of the material as it appears in "Two dimensional modelling of blob dynamics in tokamak edge plasmas," G. Q. Yu, S. I. Krasheninnikov, and P. N. Guzdar published in Physics of Plasmas 13, 042508-1 (2006). The dissertation author was the primary author in this paper.

Chapter 7

SOL Blob Passing Through Biasing Potential

7.1 Introduction

The applicable divertor biasing schemes uses an electrode inserted into the plasma edge, often beyond the separatrix to establish a radial electric field [113, 114, 115]. It offers a more acceptable alternative for modifying the particle and energy transport in the SOL. Divertor biasing has been reported to be a promising applications for improving divertor performance in the areas of impurity retention, particle exhaust, and heat handling capacities. It is possible to control the radial transport of both plasma and impurities by the value and the polarity of the biasing electric field [116, 117, 118, 119, 120]. In this Chapter we will use our SOL blob model to study blob passing through a biasing potential. A theoretical critical potential value is evaluated. The influence of biasing potential width and amplitude on blob dynamics are reported.

7.2 Model Equation

As it was demonstrated numerically in [121], an impact of divertor target biasing can alter blob shape and, therefore, dynamics of the blob in the after-biased region. Here we present some qualitative conclusions on the impact of divertor target biasing on blob propagation. We assume a bell shape of biasing potential barrier

$$\phi_{bias}(x) = \Phi_{bias} \exp\left(-\left((x - x_{bias})/\delta_{bias}\right)^2\right) \tag{7.1}$$

where Φ_{bias} and δ_{bias} are the magnitude and the width of biasing potential, and x_{bias} determines its spatial location.

We notice that if we omit of the first term in LHS of equation (3.39) then there will be no impact of the biasing on the blob propagation. Indeed, in this case, with simple change of the variable y to $y' = y - v_{bias}(x)t$, where $v_{bias}(x) = d\phi_{bias}(x)/dx$, and introduction of $\tilde{\phi} = \phi - \phi_{bias}$, we eliminate the function $\phi_{bias}(x)$ from equation (3.39). Therefore, in the variables (x, y') neither blob shape nor its propagation along x-coordinate is affected by the biasing, even though in a laboratory frame (x, y) a blob shape will be sheared along y-direction when blob moves through biased region (with this regard see also Ref. [122]). Thus, the first term in LHS of equation (3.39) is the only term, which can alter propagation along x-coordinate. Then comparing the first term in equation (3.39) with others we get the estimate for an impact of biasing on blob propagation. Estimating the first term as $\Phi_{bias}(v_b/\delta_{bias}^3)$, we find that significant effect of biasing can be expected for

$$\Phi_{bias} \gtrsim \Phi_{bias}^{crit} \approx \left(\frac{\delta_{bias}}{2}\right)^3 \delta_b \tag{7.2}$$

where the dimensionless critical biasing potential Φ_{bias}^{crit} is normalized by $\phi_* = L\rho_s/(R\delta_*)$ and spatial length is normalized by $\delta_* = \rho_s\left(L^2/(2R\rho_s)\right)^{0.2}$ as in equations (3.38) and (3.37). It is worthy to note that the non-dimensionalized form of Φ_{bias}^{crit} is $\Phi_{bias}^{crit} \approx \left(\delta_{bias}/(2\rho_s)\right)^3\delta_b/L_{\parallel}$.

To verify the expression (15) we perform a series of numerical runs for blob propagation through biasing potential. We consider the blobs with $\delta_b = 2$ and biasing potential with $\delta_{bias} \approx \delta_b$, $\delta_{bias} \approx 2\times\delta_b$, and $\delta_{bias} \approx 0.5\times\delta_b$. We scan the magnitude of the potential Φ_{bias} and analyze the impact of biasing on blob shape after the potential barrier. We observe that critical amplitude of the potential, when biasing significantly alter a blob shape in the after-barrier region, scales as $\Phi_{bias}^{crit} \propto (\delta_{bias})^p$ with p being between 2 and 3, which is in a reasonable agreement with equation (7.2).

7.3 Blob Passing Through Biased Region

To prove our evaluation, we use the most stable blob, $\delta_b = 2$, as a test vehicle to hit the biasing potential wall in simulation. In Figure 7.1 to Figure 7.4, we show the test blob after passing through the barriers with $\delta_{bias} = 2$ (which in figures in this section is shown as δ_{ϕ}, standing for scale length of biasing potential, to save some space in figures) to equal to the test blob's scale length, $x_{bias} = 10$ at the center in x direction in simulation domain, and varied Φ_{bias}. From equation (7.2) we find that in

this case $\Phi_{bias}^{crit} \sim 2$. In the plotted results, we observe that major blob bodies coherently pass through biased region in the cases when Φ_{bias} is 0.25 or 0.5, although the trajectory of blobs is strongly deviated by the biasing potential at the center. As $\Phi_{bias}=1$ in Figure 7.3, the blob body is apparently deformed. A large part of the blob body is trapped in the biasing zone however still a major piece from blob body gets across the zone and keeps moving outward. In the case of $\Phi_{bias}=2$, i.e. $\Phi_{bias} \gtrsim \Phi_{bias}^{crit}$, in Figure 7.4, as we expect in the early part in this section, a strong deformation and even disintegration of blob body occurs while blob gets into the barrier (see Figure 7.4). Then most fragments from original blob are trapped in the barrier. One should notice that the blobby cross-field transport is somewhat prevented or at least delayed in case of $\Phi_{bias}=$ 1 or 2. The critical biasing potential amplitude to deform blob coherent structure and prevent blob motion is in agreement with the analytical evaluation.

Next we study how the width of biasing barrier effects on blob motion. We still use the most stable blob, $\delta_b = 2$ as the hitting blob, setting $\Phi_{bias}=1$ and 2 to compare with results in Figure 7.3 and 7.4, and varying biasing potential width, δ_{bias} (or δ_ϕ in figures), in 1 and 4, two times smaller and larger that the hitting blob scale. Biasing is located at $x_{bias} = 10$ at the center in x direction in simulation domain. Figure 7.5 and 7.6 show that narrower barrier prevents the blob outgoing movement quite similar to the barrier with $\delta_{bias}=2$ does. Figure 7.7 and 7.8 show that, however, wider barrier prevents blob movement much less than $\delta_{bias}=2$ barrier does. A major part of blob body gets through the biasing zone either in $\Phi_{bias}=1$ or $\Phi_{bias}=2$ case when $\delta_{bias}=4$.

These are in agreement with equation (7.2). It can also be explained as small structure wouldn't be affected by large wave because the local variation in wave is small, just like an ant can hardly sense the curvature on a basketball. Above all, we conclude that potential barrier with scale length close to or narrower than the most coherent blob structure has better impact on prevent blob's outward movements.

7.4 Conclusion

In this Chapter we have modified blob model to study the blob passing by biasing divertor target. Theoretical analysis shows that for a large magnitude of the potential barrier $\Phi_{\text{bias}} \gtrsim \Phi_{\text{bias}}^{\text{crit}} \approx (\delta_{\text{bias}}/2)^3 \delta_b$, which is normalized by $\phi_* = L\rho_s/(R\delta_*)$ and $\delta_* = \rho_s (L^2/(2R\rho_s))^{0.2}$ as in equations (3.38) and (3.37). A strong deformation and even disintegration of the blob as coherent structure will be observed while blob pass through a biasing potential barrier higher than the critical value. Numerical simulations confirm the theoretical prediction. Simulation results visualize that blob can coherently move across lower barrier less than critical value. A strong deformation occurs while blob passes through the critical barrier. We observe that major blob bodies coherently pass through biased region in the cases when Φ_{bias} is small. In the case of $\Phi_{\text{bias}} \gtrsim \Phi_{\text{bias}}^{\text{crit}}$, a strong deformation and even disintegration of the blob as a coherent structure occurs while blob gets into the barrier. We also find that blobby cross-field transport is somewhat prevented or at least decelerated by the biasing potential. Also following equation (7.2), we study how the width of biasing barrier

effects on blob motion. Numerical results shows that the narrower barrier prevents the blob outgoing movement better than wider barrier. It can be explained as small structure wouldn't be affected by large wave because the local variation in wave is small. Therefore potential barrier with scale length close to or narrower than the most coherent blob structure has better impact on prevent blob's outward movements.

The text of Chapter 7 contains material of the paper "Dynamics of blobs in scrape-off-layer/shadow regions of tokamaks and linear devices," G. Q. Yu and S. I. Krasheninnikov, published in Physics of Plasmas 10, 4413 (2003). The dissertation author was the primary author in this paper.

Figure 7.1 (Color) δ_b=2 blob passing biasing potential barrier with δ_{bias}=2 (δ_ϕ in the figure), Φ_{bias}=0.25, and x_{bias}=10.

Figure 7.2 (Color) δ_b=2 blob passing biasing potential barrier with δ_{bias}=2 (δ_ϕ in the figure), Φ_{bias}=0.5, and x_{bias}=10.

Figure 7.3 (Color) δ_b=2 blob passing biasing potential barrier with δ_{bias}=2 (δ_ϕ in the figure), Φ_{bias}=1, and x_{bias}=10.

Figure 7.4 (Color) δ_b=2 blob passing biasing potential barrier with δ_{bias}=2 (δ_ϕ in the figure), Φ_{bias}=2, and x_{bias}=10.

Figure 7.5 (Color) δ_b=2 blob passing biasing potential barrier with δ_{bias}=1 (δ_ϕ in the figure), Φ_{bias}=1, and x_{bias}=10.

Figure 7.6 (Color) δ_b=2 blob passing biasing potential barrier with δ_{bias}=1 (δ_ϕ in the figure), Φ_{bias}=2, and x_{bias}=10.

Figure 7.7 (Color) $\delta_b=2$ blob passing biasing potential barrier with $\delta_{bias}=4$ (δ_ϕ in the figure), $\Phi_{bias}=1$, and $x_{bias}=10$.
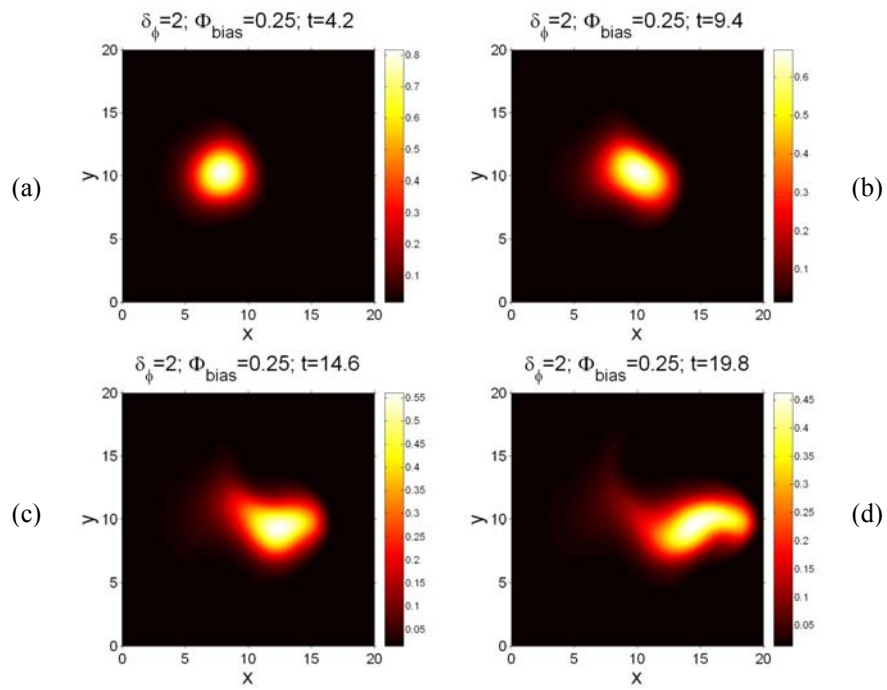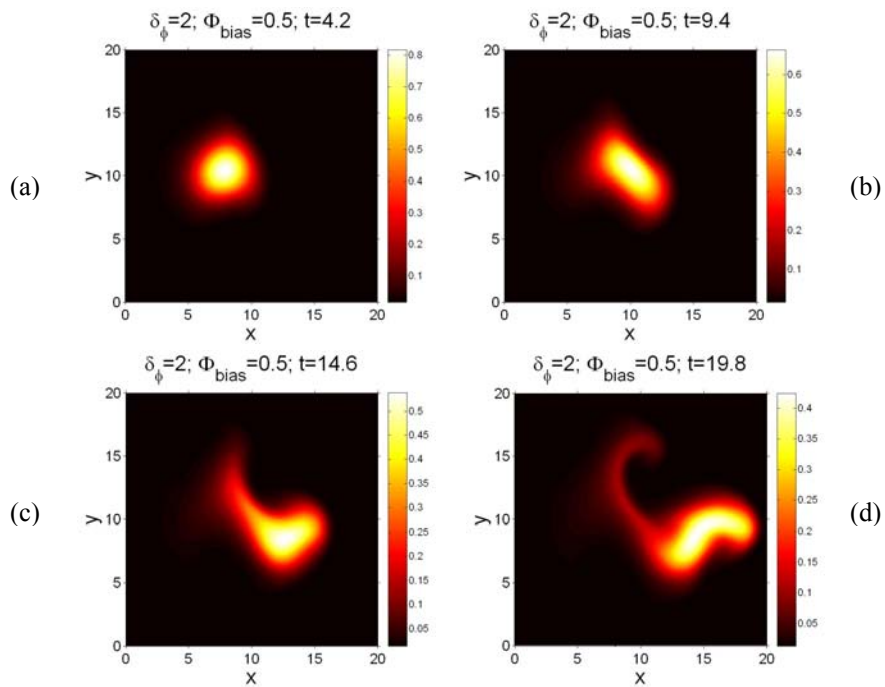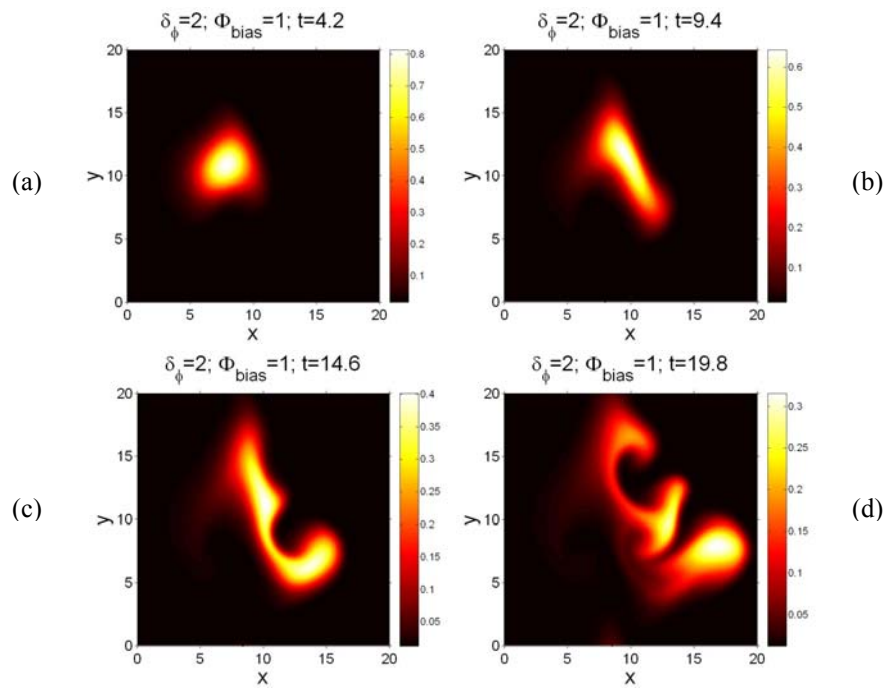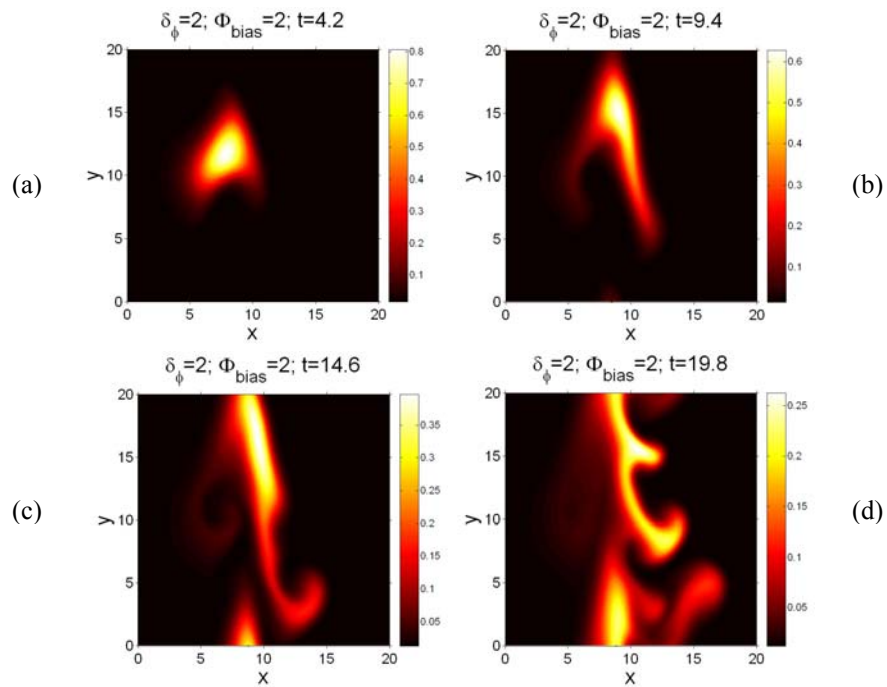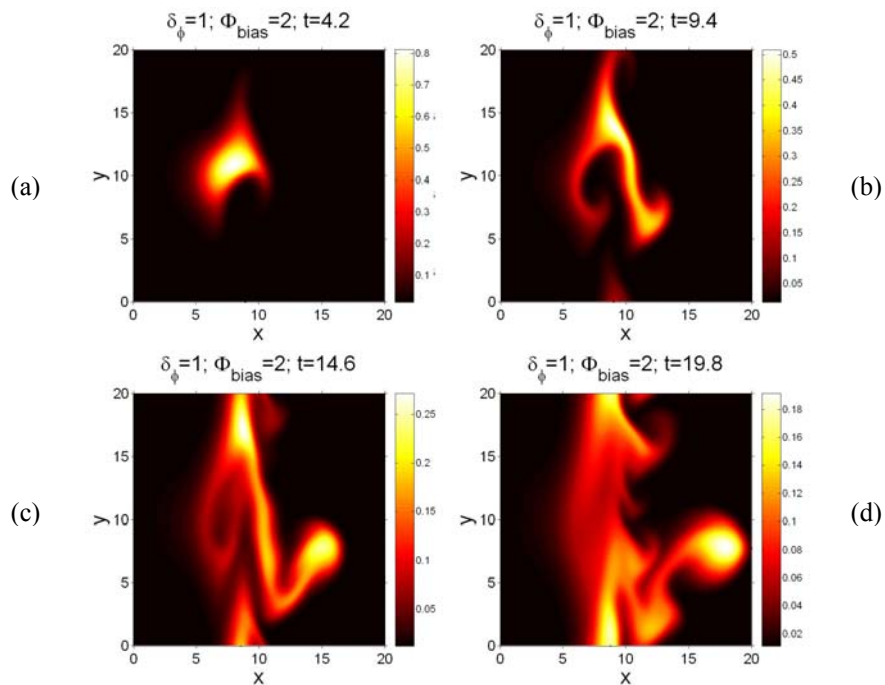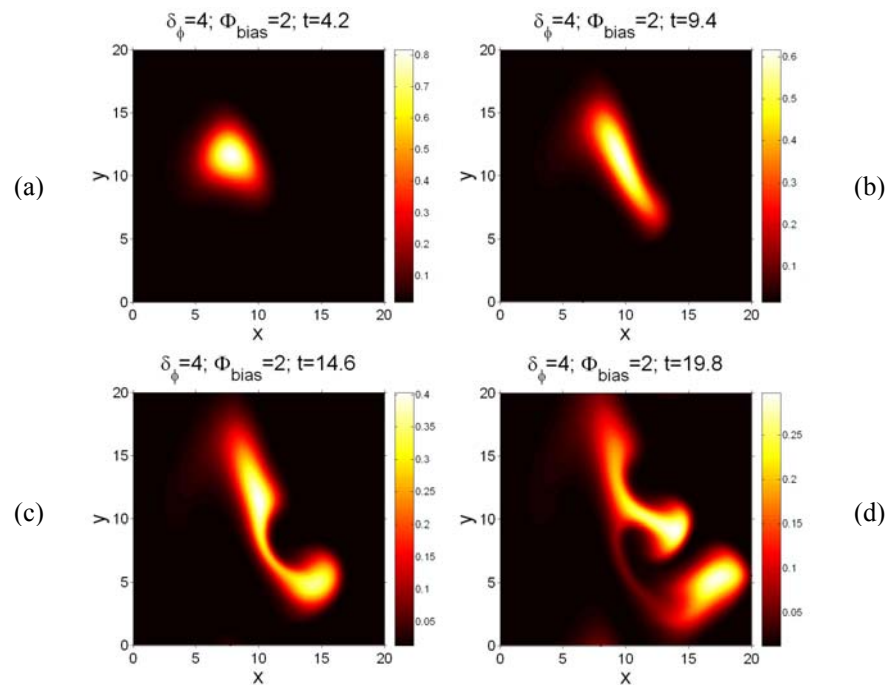

Figure 7.8 (Color) $\delta_b=2$ blob passing biasing potential barrier with $\delta_{bias}=4$ (δ_ϕ in the figure), $\Phi_{bias}=2$, and $x_{bias}=10$.

Chapter 8

Rotational Blob Dynamics

8.1 Introduction

In this Chapter, we present our study of dynamics and stability of blobs which have both density and temperature higher than the surrounding plasma. One dynamic feature of this type of "non-thermalized" blob is rotation, or spin, which is due to monopole temperature potential in blob and plasma motion associated with it. Blob dynamics and instabilities are altered greatly by the rotational behaivor. Most of our studies of rotational blob are reported in Ref. [123] and [124].

In previous Chapters, we demonstrate that an effective gravity force produces a charge dipole due to charge separation in a blob and results in radial transport of the blob as a coherent object. We note that the monopole density concentration in blob is always accompanied by a charge dipole. The magnitude of the electric field in dipole is determined by the balancing of the particle drift source with two counter effects: the loss of charge by current flow $\mathbf{j}_{\parallel}$ along the field lines to the divertor sheaths, and the mixing of the positive and negative charges by blob spin around its axis, which act to reduce the internal charge polarization. Thus, the plasma spin in blob is an important

dynamical variable. The instability is enhanced by the blob spin but its radial transport is hindered by the spin by partially defeating the internal charge polarization.

Blobs develop spin when two conditions are satisfied: (i) the parallel transport of charge and energy to the sheaths is sufficiently rapid to suppress parallel variation of the electrostatic potential and temperature along B ($k_\parallel$=0), and (ii) the blob has an internal temperature profile T_e(r), where r is the blob radial coordinate. The case of interest here is a cylindrically symmetric blob with a hot dense core, so that both n(r) and T_e(r) are monotonically decaying profiles. The first condition ensures that the blob is electrically connected to the sheath and thus has a large Bohm sheath potential. The second condition ensures that this potential produces a radial electric field in the blob and azimuthal spin around its axis. Previous Chapters on blob study are concerned with the far SOL where the blobs are in thermal equilibrium with the background plasma due to the rapid parallel heat transport. In this limit, T_e=const and the blobs did not spin. This Chapter has the goal of understanding blob properties near the separatrix, where the blobs have not yet had time to lose their hot interiors by parallel heat transport. This work is relevant to understanding the blob-like objects thrown off by ELMs which have central densities and temperatures characteristic of the top of the pedestal, much denser and hotter than the surrounding SOL plasma.

In addition to the physics mentioned above, blob spin can also drive internal rotational instabilities that can tear the blob apart. This is a subject of our study. The theory of rotational instabilities of fusion plasmas has a long history [125, 126, 127, 128]. We use our numerical results to show the rotational instabilities of a hot blob,

driven by its own internal spin, play a role in determining its dynamics and the associated SOL particle and energy transport. Another task for this study is to determine the qualitative property of the dominant rotational mode so that it can be used as a "signature" of blob spin (and thus of sheath connection) in understanding experimental visual 2D blob data, such as provided by the gas puff imaging diagnostic [20, 50, 129]. This study is restricted to the $k_\parallel = 0$ limit in which blob spin is expected to be large. The instability is driven by a combination of centrifugal force, Coriolis, Kelvin-Helmholtz, and rotational shear effects.

Next we are going to build up a rotational blob model and use our numerical scheme to study blob's rotational dynamics.

8.2 Model Equation

A minimal set of equations for understanding convective transport of hot blobs consists of the vorticity equation for the electrostatic potential and continuity equations for the plasma density, n, and electron temperature, T_e. For simplicity we work in the cold ion limit. The fundamental equations take the form

$$\rho_s^2 \nabla_\perp \cdot \left(n \frac{d}{dt} \nabla_\perp \phi \right) + \frac{2\rho_s C_s}{R} \frac{\partial n}{\partial y} = \frac{2C_s}{L_\parallel} n(\phi - \phi_B \theta) \tag{8.1}$$

$$\frac{dn}{dt} = D\nabla_\perp^2 n \tag{8.2}$$

$$\frac{d\theta}{dt} = D\nabla_\perp^2 \theta \tag{8.3}$$

where we assume $T_e = T_0 + \delta T_e$ has a small perturbation and only consider the perturbed temperature in the parallel current term, $\theta = \delta T_e/T_0$ is the normalized electron temperature, $C_s = \sqrt{T_0/m_i}$, $\rho_s = C_s/\Omega_i$, $\Omega_i = eB/m_i c$, and in the Bohm sheath potential $\phi_B \theta$ typically $\phi_B = \ln\sqrt{m_i/m_e} \sim 4$. Parallel energy loss is neglected in equation (8.3), under the assumption that $\tau_c < \tau_{E_\parallel}$ where τ_c is a convective time scale of interest, to be defined subsequently. In the opposite limit, $\tau_c > \tau_{E_\parallel}$, the blob will quickly thermalize to the background temperature. Parallel particle loss is also neglected in equation (8.1).

The "thermalized blob equations" result from taking $T_e = $ constant, which trivially solve equation (8.3). Since ϕ_B is then just a constant potential, it may be set to zero, leaving equations (8.1) and (8.2) which are the equations dominating non-rotational blobs in preceding Chapters.

For more convenience, we use the same normalization scheme as in as in equations (3.37) and (3.38) to make all coefficients to be unity. It is worthy to note that potential ϕ is normalized by ϕ_* and temperature θ is normalized by amplitude of temperature variation θ_0. Equation (8.1) then reads

$$\nabla \cdot \left(n \frac{d}{dt} \nabla\phi \right) + \frac{\partial n}{\partial y} = n(\phi - \Phi_{B0}\theta) \tag{8.4}$$

where dimensionless $\Phi_{B0} = \phi_B \theta_0/\phi_*$. We drop the sub-notation $\perp$ for convenience and equations (8.2) and (8.3) don't charge form. To simplify our work, we take Boussinesq approximation in the rotational blob model.

Next we investigate the above equation with addition of spin through Bohm sheath potential $\Phi_{B0}\theta$ with $\theta(t=0) = n(t=0)$, we adjust the value of Φ_{B0} from 0 to 10. Larger Φ_{B0} will give us stronger rotation in blob. Note that equation (8.4) includes the rotational, curvature, and sheath conductivity terms and it is normalized by the δ_* for spatial length and t_* for time as in equation (3.37).

8.3 Blob Rotation

Based upon rotational equation (8.4), results for the scaled x-velocity of blob propagation are shown in Figure 8.1. When both the spin and vorticity convection term are neglected, the blob velocity has the simple scaling $v_x \sim 1/\delta^2$, where δ again is the scale length of blob, and results in a characteristic time for a blob to convect one blob radius of $\tau_c \sim \delta^3$. This scaling leads to straight-line trajectories in Figure 8.1. Comparing the spinning and nonspinning blobs for the same a, spinning blobs move more slowly than their nonspinning counterparts. Finally note that all blobs move at the same speed for $\tau \ll \tau_c$ because there is no time for charge mixing by vorticity convection due to Kelvin–Helmholtz (KH) instability or spin. The blobs typically show motion in both x and y directions. Comparing with non-rotational blob simulation in previous Chapters, we see the suppression of v_x and the generation of v_y due to spin-induced charge mixing. The quantitive analysis for the slowing of v_x and the generation of v_y, and criteria controlling the velocity slowdown by spin can be found in Ref. [124].
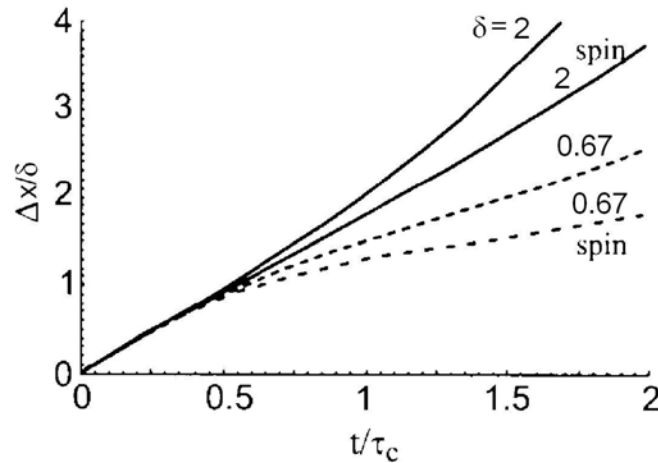
Figure 8.1 Normalized radial displacement Δx of blob vs time normalized to blob convection time τ_c. Numbers indicate the value of δ. The curves labeled "spin" have $\Phi_{B0}=10$, while the curves without the spin label have $\Phi_{B0}=0$. Note that (i) the speed increase as $\delta \to 0$ reflected in the scaling of τ_c is saturated by the vorticity convection term, (ii) for the same δ, spinning blobs move more slowly than their non-spinning counterparts, and (iii) that all blobs move at the same speed for $t \ll \tau_c$ because there is not time for charge mixing by vorticity convection due to KH instability or spin.

The rest of this section will be devoted to studying blob's rotational dynamics in the 2D slab domain. The 2D simulations employed to obtain Figure 8.1 exhibit a rich variety of phenomena. More results in detail are illustrated by snapshots shown in Figure 8.2 through Figure 8.4. At longer times, there are significant ambiguities in the blob trajectories due to blob instabilities which distort the blob's shape, and in extreme cases, destroy its coherence. For $\delta=0.67$ blob with $\Phi_{B0}=1$, this less-than-δ_* blob tends to mushroom effect as in Chapter 5. However, the structure losses symmetry because of rotation process inside. As Φ_{B0} increases to 10, the monopole temperature potential becomes stronger, so does the rotational process. Both x-direction velocity and mushroom effect are suppressed. This is in agreement with the velocity model above.

Furthermore, blob obtains velocity in y direction and evolves into rotational instability. As noted previously, the KH instabilities are present in nonspinning blob simulations. In the spinning case, rotational instabilities are observed (see the simulation results below). These instabilities result in a pinwheel pattern (somewhat resembling a spiral galaxy) that ejects the outer region of the blob. For $\delta=3.33$ blob with $\Phi_{B0}=10$, the larger-than-δ_* blob doesn't tend to fingering effect as its counterpart does in Chapter 5. The mixing process due to spin lowers the effective gravitational force and delays the RT instability. The rotational instability firstly happens in the outer region.

The frames in Figure 8.3 shows that the instability has undergone several e foldings to produce an observable distortion of the blob. The instability peaks near the outside of the blob and throws off an outer shell of material that wraps around to form "arms." The arm is left behind by the blob's rotation and curvature-driven propagation to the right. The instability shown here is clearly rotational in origin and differs qualitatively from the curvature-driven blob instabilities studied in previous Chapters. This figure shows the development of two major "arms" thrown off from blob body, which is corresponding to the mode-2 instability discussed in Ref. [123]. Similar run with different δ has different mode as in Figure 8.4. We remark that the blob dynamics (e.g., temporal variation of v_x and v_y) at later times is very interesting in the simulation as other rotational effects come into play. For example, the radial velocity of the blob is observed to increase after throwing off its outer "arms" and it develops a poloidal velocity.
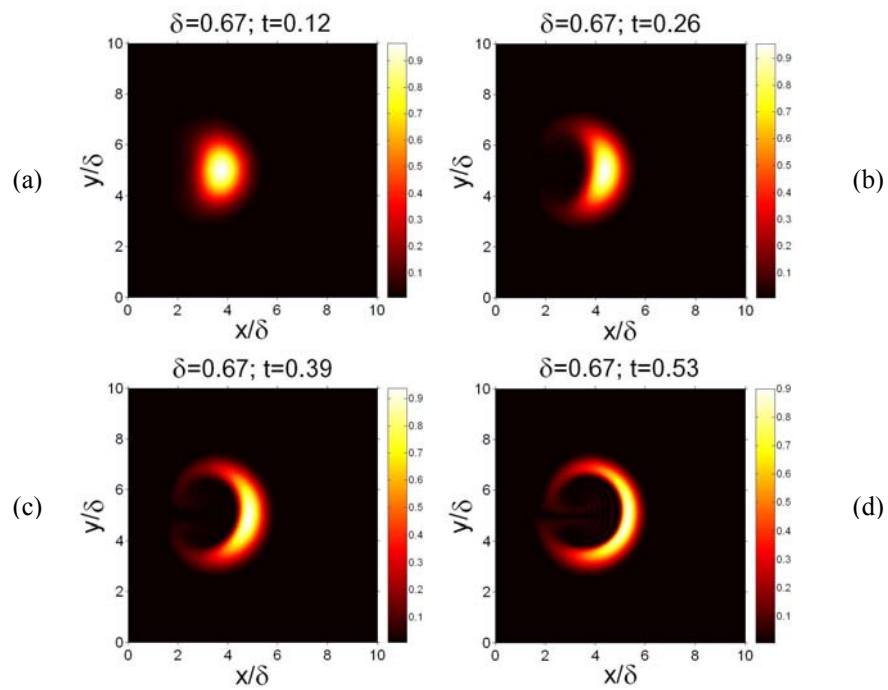
Figure 8.2 (Color) Rotational blob with δ=0.67 and Φ_{B0}=1.
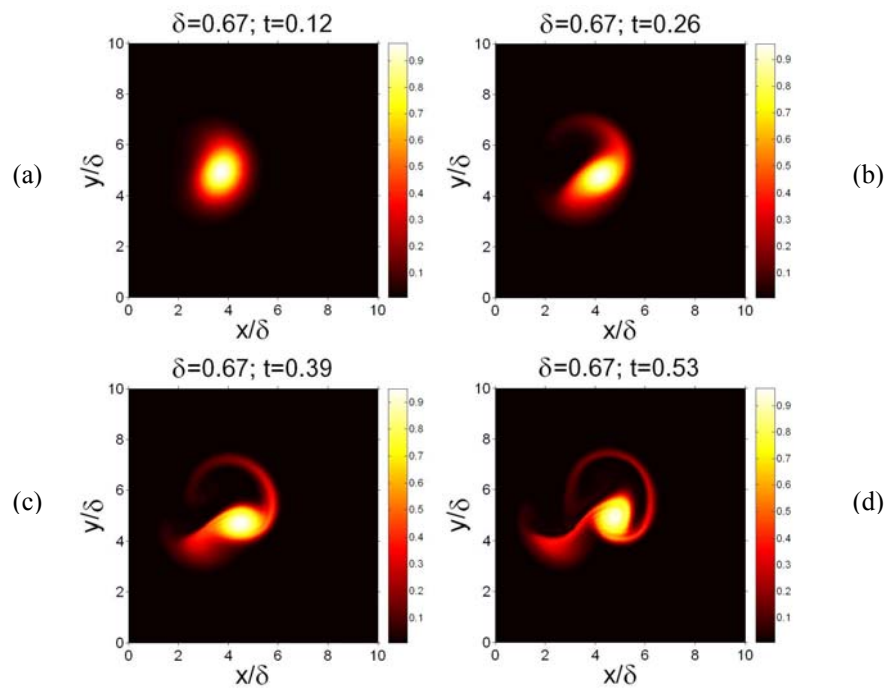
Figure 8.3 (Color) Rotational blob with δ=0.67 and Φ_{B0}=10.
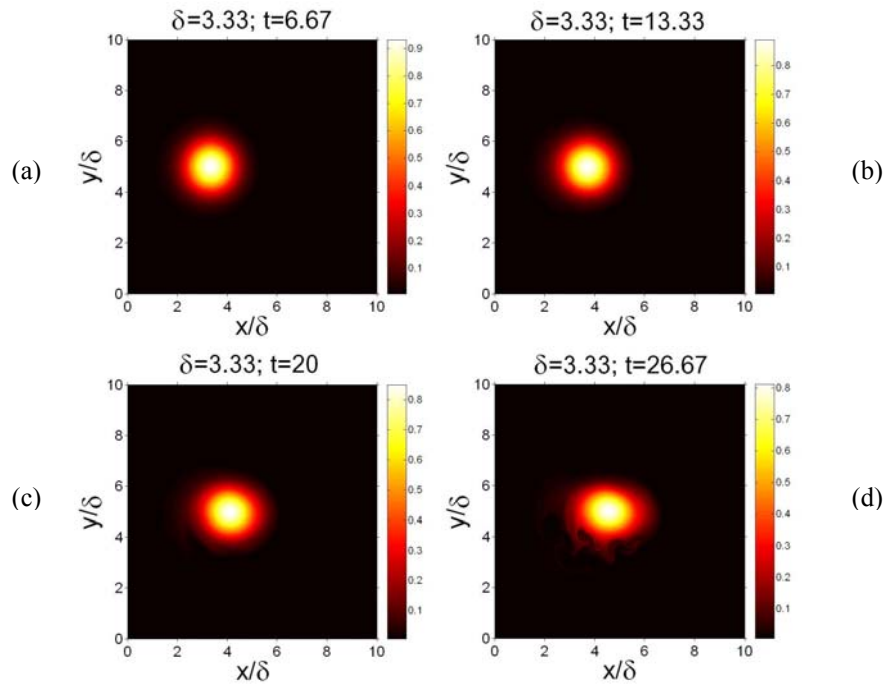
Figure 8.4 (Color) Rotational blob with δ=3.33 and Φ_{B0}=10.

8.4 Conclusion

In this Chapter we study the non-thermalized blob with plasma rotation. A 2D rotational blob model is built up. Blob dynamics in 2D domain is analysed and interesting 2D evolutions are shown. We have we observed the suppression of radial velocity and the generation of poloidal velocity. Deformation by KH and RT instabilities are suppressed due to the spin-induced mixing of the curvature-generated charge separation. Fingering and mushroom effects are inhibited by the rotation. However, blobs are linearly unstable with evolution of rotational instability in

different modes. At later times rotational instability can distort the blob's shape by throwing off the out "arms", and in extreme cases, destroy its coherence.

The text of Chapter 8 contains material of the paper "Rotational stability of plasma blobs," D. A. D'Ippolito, J. R. Myra, D. A. Russell, and G. Q. Yu, published in Physics of Plasmas 11, 4603 (2004) and material of the paper "Convective transport in the scrape-off-layer by nonthermalized spinning blobs," J. R. Myra, D. A. D'Ippolito, S. I. Krasheninnikov and G. Q. Yu, published in Physics of. Plasmas 11, 4267 (2004). The dissertation author was a co-author in these papers

Chapter 9

Conclusion

This thesis has been a theoretical and numerical study of mesoscale plasma structures transport in the SOL region in fusion devices. It turns out that a rather simple 2D model of blob propagation, based on the effective plasma gravity caused by ∇B and magnetic curvature or any other effective gravitational force effect, describes many essentials of nonlinear evolution and radial advection of such mesoscale structures as so-called blobs.

This work has presented the derivation of the 2D blob model. Different closures are introduced to describe several different physical situations. Our focus is on blob along the open field lines and blob with high plasma pressure without reaching the target plates, i.e. the SOL and HB models in this work. A specific normalization scheme is introduced to reduce all coefficients in governing equations to be unity. Characteristic spatial and time scale are obtained from this normalization method. Spatial scale $\delta_* = \rho_s \left(L^2 /(2R\rho_s) \right)^{0.2}$ and time scale $t_* = \left(\delta_* \right)^3 R /(L\rho_s^2 C_s)$ are showed to be critical values in the SOL blob dynamics and $\delta_* = C_s^2 L_{\parallel}^2 /(2\alpha^2 R V_A^2)$ and $t_* = L_{\parallel} /(2\alpha V_A)$ in the HB blob dynamics. It is unveiled that both the SOL and HB

cases are sensitive to the structure length scale. For coherent structure larger than δ_*, dissipation term becomes dominant. For structure smaller than δ_*, inertia term becomes dominant. δ_* is equal to one in the normalized model. In addition, blob dynamics in the SOL model could have a much stronger change than in the HB model as the δ changes from one side of δ_* to the other side. Meanwhile, by local linear stability analysis we find out that in both SOL and HB models simple 1D structure can be unstable. In the case $\delta_y \rightarrow \infty$, the instability requires $d\ln(n_0)/dx < 0$ and the most unstable perturbations are those with $|k_y| >> |k_x|$, while for $\delta_X \rightarrow \infty$, both negative and positive derivatives of the density, $d\ln(n_0)/dy$, are unstable (instability requires $k_x k_y d\ln(n_0)/dy > 0$) and the most unstable perturbations are those with $|k_y| = |k_x|$. It is indicated that dynamics in HB model is less sensitive to blob scale length than dynamics in SOL model. We also conclude that it is unlikely that blobs with large spatial scale $\delta_b > 1$ can move radially as coherent structures, while blobs with $\delta_b < 1$ seem to be able to move as coherent structures to large distances. Meanwhile, we list characteristic values of δ_*, t_*, and v_* for several popular toroidal plasma devices, such as DIIID, NSTX, C-MOD, and ITER. It is worthy to note that the scale length, δ_*, for all devices is in order of 1 cm, and velocity is in order of 10^5 cm/s. This is in agreement with experimental measurements in SOL in tokamak.

Using our numerical schemes, we have carried out simulations of the SOL blob dynamics on circular blobs, oval blobs, and dips. We also study the effect of density background, diffusivity, and inertia term on blob dynamics.

We have found the most structurally stable blob has dimensionless scale length around one, which is corresponding to the characteristic scale length δ_* derived in Chapter 3, and propagate coherently to large distances. Steep nose profile can explain experimentally detected asymmetric profile. Blobs smaller than one evolve into rather slowly moving mushroom-like structures due to strong velocity shear. Blobs larger than one are subject to the fingering instability, which very quickly chops large blobs into a number of relatively narrow fingers reducing their effective cross-field scales. Blobs with spatial scales close to one can coherently move to long distances. Blob velocity is proportional to $1/\delta^2$., which is in agreement with our scaling analysis.

Also we have found that scale lengths δ_x and δ_y are not equivalent. δ_y determines motion mode and velocity. High background plasma density effectively narrows down blob size.

In the model without the Boussinesq approximation (the FI-SOL model), dynamics is somewhat suppressed. Big blob motion, such as $\delta=5$ blob, doesn't change much comparing with results from the RI-SOL model. For $\delta=0.2$ blob, mushroom effect is greatly suppressed. In $\delta=1$ blob simulation, inertia effect is not perceptible. Meanwhile, relaxation tail gets longer in the FI case. Over all, FI-SOL model in general is coincident with RI-SOL model. However, some details differ. In particular the most stable scale length shifts from 2 to 1.

Density dips move inward to the core plasma, opposite to the blob movement. Impurity can be carried into the core by dip motion. Vorticity effects in dip is strong, slows down propagation speed and breaks one dip into pieces.

The inertia term in vorticity equation drives the structure to mushroom shape and builds up vortex dipole within the structure. Blob goes to mushroom shape when neglecting parallel current term regardless of the scale length. Blob goes to fingering effect without inertia term regardless of the scale length.

In the HB blob simulation we apply our code on blobs with normalized scale length of 0.01, 0.2, 1, and 5. We have found that HB blobs also coherently move outward (RHS). They have wider stable range in terms of scale length. They also have longer relaxation tail. We observe mushroom effect for extremely small blob, and fingering effect for big blobs with steeper boundary. HB blob moves with a constant velocity about one half in normalized unit. Unlike the SOL blob the drift velocity does not depend on blob size δ. Blob's velocity slows down more quickly as the scale length getting smaller.

The plasma diffusion doesn't change the blob motion modes much. But it has stabilization effect on blob dynamics. It is shown that RT instability is suppressed by large diffusivity.

Furthermore we have modified blob model to study the SOL blob passing by biasing divertor target. Theoretical analysis shows that for a large magnitude of the potential barrier $\Phi_{bias} \gtrsim \Phi_{bias}^{crit} \approx \left(\delta_{bias}/2\right)^3 \delta_b$, which is normalized by $\phi_* = L\rho_s/(R\delta_*)$ and $\delta_* = \rho_s\left(L^2/(2R\rho_s)\right)^{0.2}$. A strong deformation and even disintegration of the blob as coherent structure will be observed while blob pass through a biasing potential barrier higher than the critical value. Numerical simulations confirm the theoretical prediction. Simulation results visualize that blob can coherently move across lower barrier less

than critical value. A strong deformation occurs while blob passes through the critical barrier. We observe that major blob bodies coherently pass through biased region in the cases when Φ_{bias} is small. In the case of $\Phi_{\text{bias}} \gtrsim \Phi_{\text{bias}}^{\text{crit}}$, a strong deformation and even disintegration of the blob as a coherent structure occurs while blob gets into the barrier. We also find that blobby cross-field transport is somewhat prevented or at least decelerated by the biasing potential. From another point of view to the critical value of potential barrier, we study how the width of biasing barrier effects on blob motion. As one can predicts, the narrower barrier prevents the blob outgoing movement better than wider barrier. One of the reasons is that small structure wouldn't be affected by large wave because the local variation in wave is small. Therefore potential barrier with scale length close to or narrower than the most coherent blob structure has better impact on prevent blob's outward movements.

Finally we study the non-thermalized blob with plasma rotation. A 2D rotational blob model is built up. Blob dynamics in 2D domain is analysed and interesting 2D evolutions are shown. We have we observed the suppression of radial velocity and the generation of poloidal velocity. Deformation by KH and RT instabilities are suppressed due to the spin-induced mixing of the curvature-generated charge separation. Fingering and mushroom effects are inhibited by the rotation. However, blobs are linearly unstable with evolution of rotational instability in different modes. At later times rotational instability can distort the blob's shape by throwing off the out "arms", and in extreme cases, destroy its coherence.

We conclude that modelling work of blob shows many features of mesoscale structure transport in the SOL so far. It is in agreement with experimental measurements. Also it helps further our understanding of the anomalous cross field transport in fusion plasma devices.

Appendix

A. Change the Form of Inertia Term in Relaxation Method

$$\nabla \cdot \left(n \frac{d}{dt} \nabla \phi \right) = \nabla \cdot \left(n \left(\frac{\partial}{\partial t} - \nabla \phi \times \hat{z} \cdot \nabla \right) \nabla \phi \right)$$

$$= \nabla \cdot \left(\frac{\partial}{\partial t} (n \nabla \phi) - \frac{\partial n}{\partial t} \nabla \phi - (\nabla \phi \times \hat{z} \cdot \nabla)(n \nabla \phi) + \nabla \phi (\nabla \phi \times \hat{z} \cdot \nabla n) \right)$$

$= 0$ for incompressibility

$$= \nabla \cdot \left(\frac{\partial}{\partial t} (n \nabla \phi) - (\nabla \phi \times \hat{z} \cdot \nabla)(n \nabla \phi) - \left(\frac{\partial n}{\partial t} - (\nabla \phi \times \hat{z} \cdot \nabla n) \right) \nabla \phi \right)$$

$$= \frac{\partial}{\partial t} \nabla \cdot (n \nabla \phi) + \nabla \cdot (- \nabla \phi \times \hat{z} \cdot \nabla)(n \nabla \phi) \quad \text{(The second term derivation is below)}$$

$$= \frac{\partial}{\partial t} \nabla \cdot (n \nabla \phi) + (- \nabla \phi \times \hat{z} \cdot \nabla)(\nabla \cdot (n \nabla \phi)) + E_x n_y - E_y n_x$$

$$= \frac{d}{dt} \nabla \cdot (n \nabla \phi) + E_x n_y - E_y n_x \qquad E = \frac{1}{2} (v_x^2 + v_y^2)$$

$$= \frac{d}{dt} \Omega + E_x n_y - E_y n_x \qquad \Omega = \nabla \cdot (n \nabla \phi)$$

$$\nabla \cdot \left(-\nabla \phi \times \hat{z} \cdot \nabla \right) \left(n \nabla \phi \right) = \nabla \cdot \left(v \cdot \nabla \right) \left(n \nabla \phi \right)$$

$$= \frac{\partial}{\partial x_i} \left(v_j \frac{\partial}{\partial x_j} \left(n \frac{\partial \phi}{\partial x_i} \right) \right)$$

$$= \frac{\partial v_j}{\partial x_i} \frac{\partial}{\partial x_j} \left(n \frac{\partial \phi}{\partial x_i} \right) + v_j \frac{\partial}{\partial x_j} \left(\frac{\partial}{\partial x_i} \left(n \frac{\partial \phi}{\partial x_i} \right) \right)$$

$$= \frac{\partial v_j}{\partial x_i} \frac{\partial n}{\partial x_j} \frac{\partial \phi}{\partial x_i} + \frac{\partial v_j}{\partial x_i} \frac{\partial^2 \phi}{\partial x_i x_j} n + \left(v \cdot \nabla \right) \nabla \cdot \left(n \nabla \phi \right)$$

$$= \frac{\partial v_x}{\partial x} \frac{\partial n}{\partial x} \frac{\partial \phi}{\partial x} + \frac{\partial v_y}{\partial x} \frac{\partial n}{\partial y} \frac{\partial \phi}{\partial x} + \frac{\partial v_x}{\partial y} \frac{\partial n}{\partial x} \frac{\partial \phi}{\partial y} + \frac{\partial v_y}{\partial y} \frac{\partial n}{\partial y} \frac{\partial \phi}{\partial y}$$

$$+ \frac{\partial v_x}{\partial x} \frac{\partial^2 \phi}{\partial x^2} n + \frac{\partial v_y}{\partial x} \frac{\partial^2 \phi}{\partial x \partial y} n + \frac{\partial v_x}{\partial y} \frac{\partial^2 \phi}{\partial x \partial y} n + \frac{\partial v_y}{\partial y} \frac{\partial^2 \phi}{\partial y^2} n + \left(v \cdot \nabla \right) \nabla \cdot \left(n \nabla \phi \right)$$

$$= -\frac{\partial v_y}{\partial y} \frac{\partial n}{\partial x} v_y + \frac{\partial v_y}{\partial x} \frac{\partial n}{\partial y} v_y - \frac{\partial v_x}{\partial y} \frac{\partial n}{\partial x} v_x + \frac{\partial v_x}{\partial x} \frac{\partial n}{\partial y} v_x$$

$$+ \frac{\partial v_x}{\partial x} \frac{\partial v_y}{\partial x} n - \frac{\partial v_y}{\partial x} \frac{\partial v_x}{\partial x} n + \frac{\partial v_x}{\partial y} \frac{\partial v_y}{\partial y} n - \frac{\partial v_y}{\partial y} \frac{\partial v_x}{\partial y} n + \left(v \cdot \nabla \right) \nabla \cdot \left(n \nabla \phi \right)$$

$$= -\frac{1}{2} \left(\frac{\partial v_y^2}{\partial y} + \frac{\partial v_x^2}{\partial y} \right) \frac{\partial n}{\partial x} + \frac{1}{2} \left(\frac{\partial v_y^2}{\partial x} + \frac{\partial v_y^2}{\partial x} \right) \frac{\partial n}{\partial y} + \left(v \cdot \nabla \right) \nabla \cdot \left(n \nabla \phi \right)$$

$$= -E_y n_x + E_x n_y + \left(v \cdot \nabla \right) \nabla \cdot \left(n \nabla \phi \right) \qquad E = \frac{1}{2} \left(v_x^2 + v_y^2 \right)$$

Bibliography

1 http://www.iter.org/.

2 F. L. Hinton and R. D. Hazeltine, Rev. Mod. Phys. 48, 239 (1976).

3 P. C. Liewer, Nucl. Fusion 25, 543 (1985).

4 P. Helander and D. J. Sigmar, Collisional Transport in Magnetized Plasmas (Cambridege University, Cambridge, England, 2002).

5 Allen H. Boozer, Rev. Mod. Phys. 76, 1071 (2004)

6 L. M. Kovrizhnikh, Sov. Phys. JEPT 29, 475(1969).

7 A. H. Boozer and G. Kuo-Petravic, Phys. Fluids 24, 851(1981).

8 Z. Lin, W. M. Tang, and W. W. Lee, Phys. Plasmas 2, 2975 (1995).

9 D. C. Robinson, in "Turbulence and Anomalous Transport in Magnetized Plasmas", Cargese Workshop 1986, edited by D. Gresillon and M. Dubois, 21 (Ecole Polytechnique, Palaiseau, France, 1986)

10 C. M. Surko, in "Turbulence and Anomalous Transport in Magnetized Plasmas", Cargese Workshop 1986, edited by D. Gresillon and M. Dubois, 93 (Ecole Polytechnique, Palaiseau, France, 1986)

11 A. J. Wootton, B. A. Carreras, H. Matsumoto, K. McGuire, W. A. Peebles, Ch. P. Ritz, P. W. Terry, and S. J. Zweben, Phys. Fluids B2 (12), 2879 (1990).

12 S. J. Zweben Phys. Fluids 28, 974 (1985).

13 R. Jha, P. K. Kaw, S. K. Mattoo, C. V. S. Rao, Y. C. Saxena, and ADITYA Team, Phys. Rev. Lett. 69, 1375 (1992).

14 M. Endler, H. Niedermayer, L. Giannone, E. Holzhauer, A. Rudyj, G. Theimer, N. Tsois and the ASDEX Team, Nucl. Fusion 35, 1307 (1995).

15 F. J. Øynes, O-M Olsen, H. L. Pécseli, Å. Fredriksen, and K. Rypdal, Phys. Rev. E 57, 2242 (1998).

16 M. V. A. P. Heller, Z. A. Brasilio, I. L. Caldas, J. Stöckel, and J. Petrzilka, Phys. Plasmas 6, 846 (1999).

17 E. Sánchez, C. Hidalgo, D. López-Bruna, I. García-Cortés, R. Balbín, M. A. Pedrosa, B. van Milligen, C. Riccardi, G. Chiodini, J. Bleuel, M. Endler, B. A. Carreras, and D. E. Newman, Phys. Plasmas 7, 1408 (2000).

18 B. A. Carreras, V. E. Lynch, and B. LaBombard, Phys. Plasma 8, 3702 (2001).

19 J. A. Boedo, D. Rudakov, R. Moyer, S. Krasheninnikov, D. Whyte, G. McKee, G. Tynan, M. Schaffer, P. Stangeby, P. West, S. Allen, T. Evans, R. Fonck, E. Hollmann, A. Leonard, A. Mahdavi, G. Porter, M. Tillack, and G. Antar, Phys. Plasmas, 8 4826 (2001).

20 S. J. Zweben, D. P. Stotler, J. L. Terry, B. LaBombard, M. Greenwald, M. Muterspaugh, C. S. Pitcher, K. Hallatschek, R. J. Maqueda, B. Rogers, J. L. Lowrance, V. J. Mastrocola, and G. F. Renda, Phys. Plasmas 9, 1981 (2002).

21 G. Y. Antar, G. Counsell, Y. Yu, B. Labombard, and P. Devynck, Phys. Plasmas 10, 419 (2003).

22 J. L. Terry, R. Maqueda, C. S. Pitcher, S. J. Zweben, B. LaBombard, E. S. Marmar, A. Yu. Pigarov, and G. Wurden, J. Nucl. Mat. 290-293, 757 (2001)

23 A. Kallenbach, R. Dux, J. Gafert, G. Haas, L.D. Horton, M. Jakobi, B. Kurzan, H.W. M uller, R. Neu, J. Neuhauser, R. Pugno, T. P utterich, V. Rohde,W. Sandmann, S.-W. Yoon, and the ASDEX Upgrade team,, Nucl. Fusion 43, 573 (2003).

24 G. S. Kirnev, V. P. Budaev, S. A. Grashin, E. V. Gerasimov, and L. N. Khimchenko, Plasma Phys. Contr. Fusion 46, 621 (2004).

25 A. H. Nielsen, H. L. Pecsell, and J. Rasmussen, Phys. Plasmas 3, 1530 (1996).

26 G. Y. Antar, S. I. Krasheninnikov, P. Devynck, R. P. Doerner, E. M. Hollmann, J. A. Boedo, S. C. Luckhardt, and R. W. Conn, Phys. Rev. Lett. 87, 065001 (2001).

27 T. Carter, Bull. of the Amer. Phys. Soc. 47, 201 (2002).

28 Th. Pierre, A. Escarguel, D. Guyomarc'h, R. Barni, and C. Riccardi, Phys. Rev. Letter 92, 065004-1 (2004).

29 N. Platt, E. A. Spiegel, and C. Tresser, 1993, Phys. Rev. Lett. 70, 279 (2005).

30 D. L. Rudakov, J. A. Boedo, R. A. Moyer, S. Krasheninnikov, A. W. Leonard, M. A. Mahdavi, G. R. McKee, G. D. Porter, P. C. Stangeby, J. G. Watkins, W. P. West, D. G. Whyte, and G. Antar, Plasma Phys. Control. Fusion 44, 717 (2002).

31 A. Kirk, G. F. Counsell, H. R. Wilson, J. W. Ahn, R. Akers, E. R. Arends, J. Dowling, R. Martin, H. Meyer, M. Hole, M. Price, P. B. Snyder, D. Taylor, M. J. Walsh, Y. Yang, and the MAST Team, Plasma Phys. Control. Fusion 46, 551 (2004).

32 A. W. Leonard, T. H. Osborne, M. E. Fenstermacher, R. J. Groebner, M. Groth, C. J. Lasnier, M. A. Mahdavi, T. W. Petrie, P. B. Snyder, J. G. Watkins, and L. Zeng, Phys. Plasmas 10, 1765 (2003).

33 A. V. Chankin, N. Asakura, T. Fukuda, A. Isayama, K. Itami, Y. Kamada, H. Kubo, Y. Miura, T. Nakano, N. Oyama, S. Takeji, and H. Takenaga, J. Nucl. Materials 313–316, 828 (2003).

34 W. Fundamenski, W. Sailer, Plasma Phys. Contr. Fusion 46, 233 (2004).

35 S. I. Krasheninnikov, Phys. Lett. A 283, 368 (2001).

36 D. A. D'Ippolito, J.R. Myra, and S. I. Krasheninnikov, Phys. Plasmas 9, 222 (2002).

37 N. Bian, S. Benkadda, J.-V. Paulsen, and O. E. Garcia, Phys. Plasmas 10, 671 (2003).

38 O. E. Garcia, V. Naulin, A. H. Nielsen, and J. Juul Rasmussen, Phys. Rev. Lett. 92, 165003-1 (2004).

39 A. Y. Aydemir, Phys. Plasmas 12, 62503(2005).

40 G. Q. Yu and S. I. Krasheninnikov, Phys. Plasmas 10, 4413 (2003).

41 O. E. Garciaa, N. H. Bian, V. Naulin, A. H. Nielsen, and J. Juul Rasmussen, Phys. Plasmas 12, 090701 (2005).

42 S. I. Krasheninnikov, D.D. Ryutov, and G. Q. Yu, 13th International Toki Conference on Plasma Physics and Controlled nuclear Fusion, December 9-12, 2003, Toki, Japan; J. Plasma Fusion Res. SERIES 6, 139 (2005).

43 S. I. Krasheninnikov, A. I. Smolyakov, G. Yu, and T. K. Soboleva, Czech. J. Phys. 55, 307 (2005).

44 D. A. Russell, D. A. D'Ippolito, J. R. Myra, W. M. Nevins, and X. Q. Xu, Phys. Rev. Lett. 93, 265001 (2004).

45 S.J. Zweben and R.W. Gould, Nucl. Fusion 25, 171 (1985).

46 J. Bleuel, M. Endler, H. Niedermeyer, M. Schubert, H. Thomsen, and W7-AS Team, New J. Phys. 4, 38 (2002)

47 E.Martines, M. Hron, and J. Stockel, Plasma Phys.Control. Fusion 44, 351 (2002).

48 G. R. McKee, R. J. Fonck, M. Jakubowski, K. H. Burrell, K. Hallatschek, R. A. Moyer, D. L. Rudakov, W. Nevins, G. D. Porter, P. Schoch, and X. Xu, Phys. Plasmas 10, 1712 (2003).

49 R. J. Maqueda, G. A. Wurden, S. Zweben, L. Roquemore, H. Kugel, D. Johnson, S. Kaye, S. Sabbagh, and R. Maingi, Rev. Sci. Instrum. 72, 931 (2001).

50 J. L. Terry, S. J. Zweben, K. Hallatschek, B. LaBombard, R. J. Maqueda, B. Bai, C. J. Boswell, M. Greenwald, D. Kopon, W. M. Nevins, C. S. Pitcher, B. N. Rogers, D. P. Stotler, and X. Q. Xu, Phys. Plasmas 10, 1739 (2003).

51 J.D. Callen, Phys. Fluids B 2, 2869 (1990).

52 A. J. Wootton, B. A. Carreras, H. Matsumoto, K. McGuire, W. A. Peebles, C. P. Ritz, P. W. Terry, S. J. Zweben, Phys. Fluids B 2, 2879 (1990).

53 P.C. Liewer, Nucl. Fusion 25, 1281 (1985).

54 B.A. Carreras, IEEE Trans. Plasma Sci. 25, 1281 (1997).

55 M. Endler, J. Nucl. Mater. 266-269, 84 (1999).

56 B. LaBombard, Phys. Plasmas 9, 1300 (2002).

57 R. J. Fonck, P. A. Duperrex, and S. F. Paul, Rev. Sci. Instrum. 61, 3487 (1990).

58 S. F. Paul and R. J. Fonck, Rev. Sci. Instrum. 61, 3496 (1990).

59 R. D. Durst, R. J. Fonck, G. Cosby, H. Evensen, and S. F. Paul, Rev. Sci. Instrum. 63, 4907 (1992).

60 J. A. Boedo, D. L. Rudakov, R. A. Moyer, G. R. McKee, R. J. Colchin, M. J. Schaffer, P. G. Stangeby, W. P. West, S. L. Allen, T. E. Evans, R. J. Fonck, E. M. Hollmann, S. Krasheninnikov, A. W. Leonard, W. Nevins, M. A. Mahdavi, G. D. Porter, G. R. Tynan, D. G. Whyte, and X. Xu, Phys. Plasmas 10 1670 (2003).

61 F. Wagner, G. Becker, K. Behringer, D. Campbell, A. Eberhagen, W. Engelhardt, G. Fussmann, O. Gehre, J. Gernhardt, G. v. Gierke, G. Haas, M. Huang, F. Karger, M. Keilhacker, O. Klüber, M. Kornherr, K. Lackner, G. Lisitano, G. G. Lister, H. M. Mayer, D. Meisel, E. R. Müller, H. Murmann, H. Niedermeyer, W. Poschenrieder, H. Rapp, H. Röhr, F. Schneider, G. Siller, E. Speth, A. Stäbler, K. H. Steuer, G. Venus, O. Vollmer, and Z. Yü, Phys. Rev. Lett. 49, 1408 (1982).

62 H. Zohm, Plasma Phys. Control. Fusion 38, 105 (1996).

63 R Aymar, P Barabaschi, and Y Shimomura, Plasma Phys. Control. Fusion 44, 519 (2002).

64 ITER Physics Basis Editors, Nucl. Fusion 39, 2137 (1999)

65 A. Loarte, et. al., Extrapolating type-I ELMs physics to ITER Proc. 11th European Fusion Physics Workshop (Heraklion, Crete, 8–10 December 2003)

66 G. Federici and ITER JWS Group, Plasma-wall interaction in ITER Proc. 11th European Fusion Physics Workshop (Heraklion, Crete, 8–10 December 2003)

67 M. Endler, I. García-Cortés, C. Hidalgo, G. F. Matthews, ASDEX Team, and JET Team, Plasma Phys. Contr. Fusion 47, 219 (2005).

68 B. A. Carreras, J. Nucl. Materials 337-339, 315(2005).

69 J. A. Boedo, D. L. Rudakov, R. J. Colchin, R. A. Moyer, S. Krasheninnikov, D. G. Whyte, G. R. McKee, G. Porter, M. J. Schaffer, P. C. Stangeby, W. P. West, S. L. Allen, and A. W. Leonard, J. Nucl. Mater. 313-316, 813(2003).

70 Lord Rayleigh, Scientific Papers, Vol. II (Cambridge Univ. Press, Cambridge, England, 1900), p. 200.

71 G. I. Taylor, Proc. R. Soc. London Ser. A 201, 192 (1950).

72 D. H. Sharp, Physica 12D, 3 (1984).

73 K. O. Mikaelian, Phys. Rev. A 40, 4801 (1989).

74 K. O. Mikaelian, Phys. Rev. A 26, 2140 (1982).

75 H. Aref and G. Tryggvason, Phys. Rev. Lett. 62, 749 (1989).

76 M. B. Schneider, G. Dimonte, and B. Remington, Phys. Rev. Lett. 80, 3507 (1998).

77 M. Chertkov, Phys. Rev. Lett. 91, 115001-1 (2003).

78 P. G. Drazin and W. H. Reid, Hydrodynamic Stability (Cambridge University Press, 1981).

79 D. J. Acheson, Elementary Fluid Dynamics (Oxford University Press, 1990).

80 E. Meshkov, Izv. Akad. Nauk SSSR, Mekh. Zhidk. Gaza 4, 151 (1969).

81 R. D. Richtmyer, Commun. Pure Appl. Math. 8, 297 (1960).

82 Laurel Swift, at http://www.colorado.edu/MCEN/flowvis/galleries/2004/-assignment1.html

83 J. Martin, N. Rakotomalala, D. Salin, and P. Watzky, at http://www.fast.u-psud.fr/~dos/equipe/automates/bgkfr.html

84 http://www-sccm.stanford.edu/Students/witting/kh.html

85 F. F. Chen, Introduction to Plasma Physics and Controlled Fusion (Plenum Press, New York, 1984).

86 M. A. Lieberman and A. J. Lichtenberg, Principles of Plasma Discharges and materials Processing (JONH WILEY & SONS, INC, 1994)

87 D. A. D'Ippolito, J. R. Myra, S. I. Krasheninnikov, G. Q. Yu, and A. Yu. Pigarov, Contrib. Plasma Phys. 44, 205 (2004)

88 A.V. Nedospasov, V.G. Petrov, G.N. Fidel'man, Nucl. Fusion 25, 21 (1985).

89 D. Farina, R. Pozzoli, D.D. Ryutov, Nucl. Fusion 33, 1315 (1993).

90 S. I. Krasheninnikov and A. I. Smolyakov, Phys. Plasmas 10, 3020 (2003).

91 B.B. Kadomtsev: in Proc. Seventh Conference on Phenomena in Ionized Gases, Belgrade, 1965, (Eds. B. Perovic and D. Tocsic), Gradjevinska Knjiga, Belgrade, Yugoslavia, 1966, Vol. II, p. 610.

92 W.B. Kunkel and J.U. Guillory:in Proc. Seventh Conference on Phenomena in Ionized Gases, Belgrade, 1965, (Eds. B. Perovic and D. Tocsic), Gradjevinska Knjiga, Belgrade, Yugoslavia, 1966, Vol. II, p.702.

93 G. Q. Yu, S. I. Krasheninnikov, and P. N. Guzdar, Phys. Plasmas 13, 042508-1 (2006).

94 D. D. Ryutov and R. H. Cohen, Contr. Plasma Phys. 44, 168 (2004).

95 S. I. Krasheninnikov, A. I. Smolyakov, G. Yu, and T. K. Soboleva, Czech. J. Phys. 55, 307 (2005).

96 D. A. Russell, D. A. D'Ippolito, J. R. Myra, W. M. Nevins, and X. Q. Xu, Phys. Rev. Lett. 93, 265001 (2004).

97 V. Rozhansky, I. Veselova, and S. Voskoboynikov, Plasma Phys. Control. Fusion 37, 399 (1995).

98 P. B. Parks, W. D. Sessions, and L. R. Baylor, Phys. Plasmas 7, 1968 (2000).

99 S. C. Cowley, H. Wilson, O. Hurricane, and B. Fong, Plasma Phys. Contr. Fusion 45, A31 (2003).

100 R.N. Sudan, A.V. Gruzinov, W. Horton, and N. Kukharkin, Physics Reports 283, 95 (1997).

101 D. A. D'Ippolito and J.R. Myra, Phys. Plasmas 10, 4029 (2003).

102 R. N. Rudakov, Appl. Math. Mech. 31, 376 (1967).

103 C. M. Vest and V. S. Arpaci, J. Fluid Mech. 36, 1 (1969).

104 R. F. Bergholz, J. Fluid Mech. 84, 743 (1987).

105 Y.–M. Chen and A. J. Pearlstein, J. Fluid Mech. 198, 513 (1989).

106 S. A. Suslov and S. Paolucci, J. Fluid Mech. 398, 61 (1999).

107 P. N. Guzdar, J. F. Drake, D. McCarthy, A. B. Hassam and C. S. Liu, Phys. Fluids B 5, 3712 (1993).

108 T. R. Bewley, Numerical Methods in Science and Engineering, UC San Diego, (2001)

109 W. H. Press, S. A. Teukolsky, W. T. Vetterling, and B. P. Flannery, Numerical Recipes in Fortran 77, (Cambridge University Press, 2003)

110 P. N. Guzdar, N. A. Gondarenko, and P. K. Chaturvedi, Radio Sci. 33, 1901 (1998).

111 S. A. Galkin, S. I. Krasheninnikov, D. A. D'Ippolito, J. R. Myra, and X. Q. Xu, Sherwood conference 2002.

112 J. A. Boedo, et. al., 15th PSI, 2002.

113 A. Boileau, Nucl. Fusion 33, 165 (1993).

114 R. J. Taylor, M. L. Brown, D. B. Fried, H. Grote, J. R. Liberati, G. J. Morales, and P. Pribyl, Phys, Rev. Lett. 63, 2365 (1989).

115 R. R. Weynants, G. Van Oost, and G. Bertschinger, Nucl. Fusion 32, 837 (1992).

116 P. Couture, A. Boileau, R. D&coste, B. Gregory, C. Janicki, J. L. Lachambre, D. Lafrance, D. Michaud, G. G. Ross, B. Stansfield, B. Terreault, G. Abel, C. Boucher, L. Gauthier, V. Glaude, E. Haddad, A. Hubbard, J. Kalnavams, E. Knystautas, G. Le Clair, C. Liu-Hinz, H. H. Mai, F. Martin, R. Neufeld, D. Pinsonneault, N. Richard, A. Sarkissian, M. St.-Onge, D. Whyte, and W. Zuzak, Phys. Lett. A 163, 204 (1992).

117 R Decoste, J.-L. Lachambre, G. Abel, A. Boileau, C. Boucher, A. Cote, T. Fall, J.-L. Gauvreau, B. C. Gregory, E. Haddad, C. Janicki, C. Liu-Hinz, H. H. Mai, F. Martin, D. Michaud, N. Richard, G. Ross, A. Sarkissian, B. L. Stansfield, B. Terreault, and W. Zuzak, Phys. Plasmas, Vol. 1, 1498 (1994).

118 V. Rozhansky and M. Tendler, Phys. Plasmas 1, 2711 (1994).

119 D. Lafrance, R. Huang, B. L. Stansfield, E. Haddad, and J.-L. Lachambre, Phys. Plasmas 4, 3644 (1997).

120 V.Rozhansky, E.Kaveeva, S.Voskoboynikov, D.Coster, X.Bonnin, and R.Schneider, Phys. Plasmas 9, 3385 (2002).

121 H. Biglary, P. H. Diamond, and P. W. Terry, Phys. Fluids B 2, 1 (1990).

122 A. V. Filippas, R. D. Bengtson, G. X. Li, Mark Meier, Ch. P. Ritz, and E. J. PowersPhys. Plasmas 2, 839 (1995).

123 D. A. D'Ippolito, J. R. Myra, D. A. Russell, and G. Q. Yu, Phys. Plasmas 11, 4603 (2004)

124 J. R. Myra, D. A. D'Ippolito, S. I. Krasheninnikov, and G. Q. Yu, Phys. Plasmas 11, 4267 (2004).

125 J. B. Taylor, J. Nucl. Energy, Part C 4, 406 (1962).

126 M. N. Rosenbluth and A. Simon, Phys, Fluids 8, 1300 (1965).

127 L. D. Pearlstein and N. A. Krall, Phys. Fluids 9, 2231 (1966).

128 J. P. Freidberg and L. D. Pearlstein, Phys. Fluids 21, 1207 (1978).

129 S.J. Zweben, R.J. Maqueda, D.P. Stotler, A. Keesee, J. Boedo, C.E. Bush, S.M. Kaye, B. LeBlanc, J.L. Lowrance, V.J. Mastrocola, R. Maingi, N. Nishino, G. Renda, D.W. Swain, J.B.Wilgen, and the NSTX Team, Nucl. Fusion 44, 134 (2004).